Decay spectroscopy of $N \sim Z$ nuclei in the vicinity of ^{100}Sn

by

Joochun (Jason) Park

B.Sc., The University of British Columbia, 2012

A THESIS SUBMITTED IN PARTIAL FULFILLMENT OF
THE REQUIREMENTS FOR THE DEGREE OF

DOCTOR OF PHILOSOPHY

in

THE FACULTY OF GRADUATE AND POSTDOCTORAL STUDIES

(Physics)

THE UNIVERSITY OF BRITISH COLUMBIA

(Vancouver)

March 2017

© Joochun (Jason) Park 2017

Abstract

The nuclear shell model (SM) has been very successful in describing the properties and the structure of near-stable and stable isotopes near the magic nuclei. Today, the advent of powerful facilities capable of producing radioactive isotopes far from stability has enabled the test of the SM on very proton-rich or neutron-rich magic nuclei. $^{100}_{50}\mathrm{Sn}_{50}$ is a proton-rich doubly-magic nucleus, but is nearly unstable against proton emission. Key topics of nuclear structure in this region include the location of the proton dripline, the effect of proton-neutron interactions in $N \sim Z$ nuclei, single-particle energies of orbitals above and below the $N = Z = 50$ shell gaps, and the properties of the superallowed Gamow-Teller decay of ^{100}Sn.

A decay spectroscopy experiment was performed on ^{100}Sn and nuclei in its vicinity at the RIKEN Nishina Center in June 2013. The isotopes of interest were produced from fragmentation reactions of $^{124}_{54}$Xe on a $^{9}_{4}$Be target, and were separated and identified on an event-by-event basis. Decay spectroscopy was performed by implanting the radioactive isotopes in the Si detector array (WAS3ABi) and observing their subsequent decay radiations. β^+ particles and protons were detected by WAS3ABi, and γ rays were detected by a Ge detector array (EURICA).

Of the proton-rich isotopes produced in this experiment, over 20 isotopes as light as ^{88}Zr and as heavy as ^{101}Sn were individually studied. New and improved measurements of isotope/isomer half-lives, β-decay endpoint energies, β-delayed proton emission branching ratios, and γ-ray transitions were analyzed. In general the new results were well reproduced by the SM, highlighting a relatively robust ^{100}Sn core. However, the level scheme of ^{100}Sn's β-decay daughter nucleus ^{100}In was not conclusively determined because of several missing observations which were expected from various SM predictions. Significantly higher β-decay and γ-ray statistics are required on several nuclei, including ^{100}Sn, to evaluate the limit of the current understanding of their structure.

Preface

This dissertation is based on the ^{100}Sn experiment RIBF9 which took place in June 2013 at RIKEN Nishina Center, in the framework of the EURICA collaboration. I was one of the two principal analysts of the experimental data; the other was D. Lubos, a PhD student collaborator at Technische Universität München who performed an independent, parallel analysis on the same dataset with emphasis on the superallowed Gamow-Teller β decay of ^{100}Sn. On the other hand, I was the main investigator of the β-delayed proton and γ-ray data. None of the text in this dissertation is taken directly from previous publications.

In Chapter 3, the calibration methods for EURICA detectors' time, energy, and efficiency information were developed on my own, and parts of them were presented in an article titled "Gamma-spectroscopy around ^{100}Sn" which was published in *RIKEN Accel. Prog. Rep.*, vol. 48, page 29 in 2015. Energy calibration constants for each Si strip of WAS3ABi were provided from D. Lubos. However, I carried out independent calibrations of the timing and the high-energy data of WAS3ABi to improve the accuracy of the implantation position.

In Chapter 4, the discovery of new proton-rich isotopes ^{90}Pd, ^{92}Ag, ^{94}Cd, and ^{96}In was published in an article titled "New Isotopes and Proton Emitters-Crossing the Drip Line in the Vicinity of ^{100}Sn" in *Physical Review Letters*, vol. 116, pages 162501-6 in April 2016. The main author of this article is I. Čeliković. As a co-author and a member of the EURICA collaboration, I provided editorial corrections to the manuscript. A preliminary report on the isotope production was published with the title "Study of the superallowed β-decay of ^{100}Sn" in *RIKEN Accel. Prog. Rep.*, vol. 47, page 7 in 2014. The discussion of isomeric states in ^{95}Ag was discussed in private with two EURICA collaborators: K. Moschner and A. Blazhev from Institut für Kernphysik, Universität zu Köln. They have analyzed a separate dataset and have obtained consistent results of the half-lives. Based on the division of topics and their initiative to perform the experiment on ^{95}Ag, the main authorship of a future article on its isomeric decays belongs to them. On the other hand, the discovery of new isomeric γ-ray transitions in ^{96}Cd was independently verified from a separate experiment RIBF83 by R. Wadsworth and P. J. Davies from the University of York (in the United Kingdom). A joint article on the structure of ^{96}Cd is in preparation, with me being the second author. My contributions to the article include writing a supplementary section for combining the two consistent experimental results.

Table of Contents

List of Tables

List of Figures

Acknowledgements

This academic adventure would not have been possible without my research supervisor Reiner Krücken. His critical assessments and insightful suggestions throughout my research progress sharpened my ability to process the experimental results and discuss them with due rigor and clarity. I was greatly motivated by his profound knowledge and enthusiasm for nuclear structure physics, which has become a significant part of my career plan.

Many thanks go to my analysis partner Daniel Lubos. Given the abundance of experimental data to be analyzed with a variety of challenges, I found regular discussions with him to be invaluable not only for academic advancement, but also for sharing emotional burdens during stagnant times. His fluency in Japanese made my stays at RIKEN much more comfortable. I feel very fortunate to have gained such a versatile friend.

My mentor Mustafa Rajabali deserves a special recognition. Much of my hands-on expertise with detectors for decay spectroscopy and and data acquisition systems was developed under his guidance. He spared his valuable time to observe my research methods closely and offer quick and helpful tips to move forward.

This experiment has truly been an international effort, and here I cite only the key collaborators: Shunji Nishimura, Pieter Doornenbal and Giuseppe Lorusso from RIKEN; Roman Gernhäuser and Thomas Faestermann from Technische Universität München; Bob Wadsworth and Paul Davies from the University of York; and Igor Čeliković from GANIL. Besides numerous other scientists, these individuals advanced key discussions on my experimental methods and results with their professional experience.

The colleagues at TRIUMF have provided me support as well. Theorist Jason Holt taught me how to use the nuclear shell model calculation software NuShellX. PhD candidate friends Steffen Cruz, Nikita Bernier, and Lee Evitts have offered me encouragements and made this journey much more enjoyable by simply participating in the race together.

I thank my family, friends and acquaintances outside the academic environment for their unwavering support through this endeavor. I was able to mature in other aspects of my life because they have reminded me about the intangible but precious values of social life, and the world outside research laboratories.

Most of all, I thank the triune God: the Father, Jesus the Son, and the Holy Spirit for both creating such an interesting universe and giving me the inspiration to study a small but intriguing part of it. Awe belongs to God, and the delight of amazement belongs to me.

Chapter 1

Introduction

Atomic nuclei are mesoscopic quantum many-body systems of protons and neutrons, which are two distinct fermions. Each of the ∼3000 nuclides experimentally known so far is a unique combination of Z protons and N neutrons bound by the strong force, resulting in its distinct properties. Advancements in particle/heavy ion accelerator facilities, detector systems, as well as experimental methods have allowed production and investigation of many unstable nuclei that could only have been made in the most exotic environments of the universe. Consequently, the properties of these exotic nuclei then offer insights in two major disciplines of nuclear physics: nuclear astrophysics and nuclear structure.

In nuclear astrophysics, origins and production process paths of heavy elements beyond nickel and iron are a major focus. Knowing the half-lives and branching probabilities of particle emission following β decays of the unstable isotopes helps to determine the nucleosynthesis processes that reproduce the experimentally observed elemental abundances. The properties of proton-rich nuclei are important input for understanding the rapid-proton-capture process (*rp*-process) [19].

In nuclear structure, the robustness of the state-of-the-art theories are put to the test against experimental results of nuclei far away from stability. In particular, the scope of this thesis is centered around the structure of nuclei in the vicinity of $^{100}_{50}\mathrm{Sn}_{50}$: a nucleus on which many intriguing topics converge. The sections below outline each of them in more detail.

1.1 Shell model of atomic nuclei

The subsections below give brief overviews of the background information on the nuclear shell model (SM), and in this context ^{100}Sn is a pivotal nucleus. Analogous to the concept of electron shells/orbitals in atomic physics, the SM has been very successful in describing the structure of nuclei with nucleon numbers near 2, 8, 20, 28, 50, 82 and 126 (magic numbers), at which large energy gaps are present in the single-particle spectrum.

One of the modern topics of nuclear structure, both experimental and theoretical, is the robustness of the aforementioned established magic numbers far away from stability. Being doubly magic but extremely proton-rich, ^{100}Sn and nuclei in its vicinity serve as good candidate nuclei to test the robustness of the SM involving only a few particles outside the closed shells or holes in the valence orbitals. Basic principles of β and γ decays are described in Section 1.2.1 and Section 1.2.2, which offer insights into the structure of these unstable isotopes.

1.1.1 Nuclear mean-field potential and the formation of $N = Z = 50$ shells

An atomic nucleus is bound by the attractive nuclear force between protons and neutrons. The fundamental principle of the nuclear force is quantum chromodynamics (QCD) of the quarks and gluons comprising each nucleon, but QCD is not invoked further in this thesis as the knowledge of nuclear structure can be sufficiently described in terms of nucleon-nucleon (NN) interactions. The cumulative effect of NN interactions can be represented with a nuclear mean field potential, which corresponds to a net average potential acting on a bound nucleon. The mean field potential consists of several components: a central part, the spin-orbit coupling, the spin-spin and tensor interactions, etc. The number of parameters needed to describe this potential can reach up to 18 (see for example the AV18 potential [20, 21]).

The central part of the nuclear potential has two major characteristics that are verified experimentally: saturation of the attractive force at the core which reflects the Pauli exclusion principle, and weak binding near the surface which reflects the short-range nature of the strong force. A mean field potential reflecting these characteristics is the Woods-Saxon potential [22]:

$$V(r) = -\frac{V_0}{1 + \exp(\frac{r-R}{a})}, \tag{1.1}$$

where V_0 is the potential well depth, $R = r_0 A^{1/3}$ ($r_0 = 1.2$ fm) is the nuclear radius scaled by the mass number A, and a is the surface thickness. More empirical potentials employ tuned V_0 and a, and/or introduce angular asymmetry $r = r(\theta, \phi)$ to account for possible effects of nuclear deformation.

Approximating the solution of the nuclear Hamiltonian with the Woods-Saxon potential is a huge simplification, but it generates distinct orbitals with angular momenta l and large energy gaps at certain nucleon numbers. However, the inclusion of the spin-orbit coupling ($\vec{l} \cdot \vec{s}$) [23, 24] is needed to reproduce the magic numbers by splitting a given l-orbital (only $l > 0$) into two parts: spin aligned ($j = l + s$), and spin anti-aligned ($j = l - s$) where j is the total angular momentum and $s = 1/2$ for protons and neutrons. This coupling is attractive for the spin-aligned component, and its magnitude scales with l. The large spin-orbit splitting of the $g(l = 4)$ orbital causes the spin-aligned $g_{9/2}$ to be substantially lowered to an energy similar to that of the $p_{1/2}$ orbital. In addition to the 38 nucleons that can be placed in the lower orbitals, the $p_{1/2}$ and the $g_{9/2}$ orbitals can accommodate 12 more nucleons - leading to to the magic number 50. Additional nucleons have to fill much higher-energy orbitals, which are $g_{7/2}, d_{5/2}, d_{3/2}, s_{1/2}$, and $h_{11/2}$ before the next magic number 82. Fig. 1.1 illustrates the locations of magic numbers and a general ordering of the orbitals from a Woods-Saxon potential, combined with the spin-orbit interaction. Being distinct fermions, protons and neutrons have similar but separate potentials whose depths differ by a Coulomb repulsion energy. While neutrons are not charged, the isovector interaction between like nucleons is repulsive. Therefore there are no bound states for an assembly of neutrons only, with the exception of neutron stars that are intact due to a massive gravitational attraction.

For more quantitative analysis of the orbital energies, realistic mean-field potentials via Hartree-

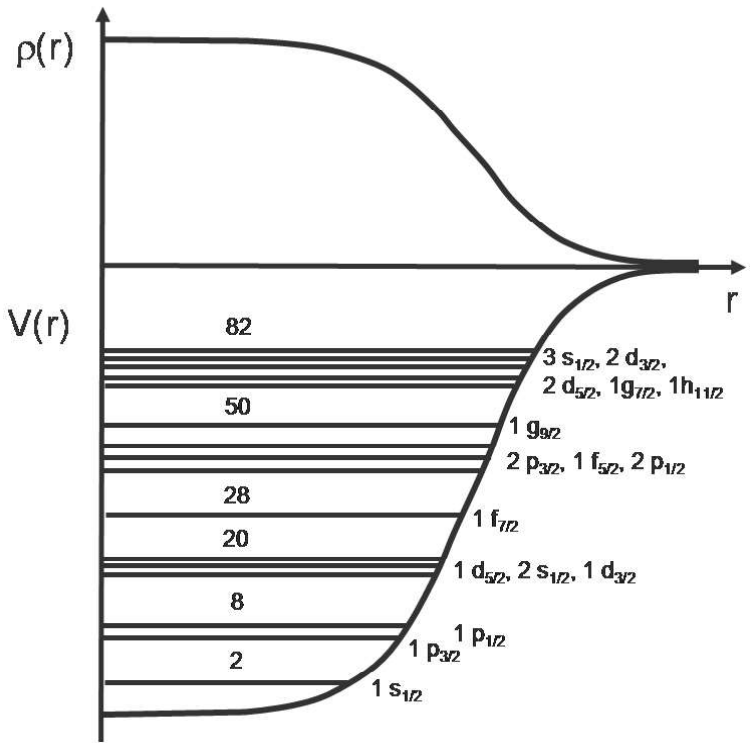

Figure 1.1: Qualitative Woods-Saxon (WS) potential depth as a function of nuclear radii for a generic nucleus from Eq. (1.1). The corresponding nuclear density, which is experimentally determined, is plotted above the x-axis. The orbitals and magic numbers generated from the WS potential and spin-orbit coupling are listed within the potential. The quantum number n of the orbitals here begins at 1, while throughout the thesis n starts at 0. This figure is taken from Ref. [3].

Fock methods [25, 26] can be applied in solving the Hamiltonian. The proton and neutron orbitals are denoted by prefixes π and ν respectively, to distinguish between orbitals with identical total angular momenta.

1.1.2 Interacting shell model

The SM described above can predict the energies and wavefunctions of single-particle states rather accurately. However, as the valence orbital is filled with nucleons, residual interactions of the valence nucleons among themselves and those in lower orbitals must be taken into account. In addition, NN scattering can promote any constituent nucleon into a valence orbital or those above it, leaving vacancies in the inner orbitals. All of these configurations must be calculated for a state with its total spin J. Consequently, the number of required calculations usually exceeds the available computing power - certainly for a nucleus as heavy as ^{100}Sn. Truncation in calculation is required on multiple levels: assumption of an inert core and inclusion of only relevant valence orbitals (vertical truncation), and limitations on the occupation numbers for each orbital (horizontal truncation). Table 1.1 shows the different models suitable for nuclei around ^{100}Sn. Two elements are required: effective single particle energies (SPEs) of the active valence orbitals and two-body matrix elements (TBMEs). For the calculations used in this work, both the SPEs and the TBMEs are empirical values which were extracted from a database of well-known nuclei.

Table 1.1: SM model spaces employed for nuclei around ^{100}Sn, available in the NuShellX software (see Section 1.1.3). The Core/Limit column refers to the inert core nucleus assumed in the model and the heaviest nucleus calculable by the allowed valence space. For a more comprehensive list, see Table 3 in Ref. [1].

Acronym	Model space	Core/Limit	Refs.
pg	$\pi\nu(1p_{1/2}, 0g_{9/2})$	$^{76}_{38}\mathrm{Sr}_{50}/^{100}_{50}\mathrm{Sn}_{50}$	[27, 28]
fpg	$\pi\nu(0f_{5/2}, 1p, 0g_{9/2})$	$^{56}_{28}\mathrm{Ni}_{28}/^{100}_{50}\mathrm{Sn}_{50}$	[29, 30]
$fpgds$	$\pi\nu(0f_{5/2}, 1p, 0g, 1d, 2s)$	$^{56}_{28}\mathrm{Ni}_{28}/^{140}_{70}\mathrm{Yb}_{82}$	[31]
$gdsh$	$\pi\nu(0g_{7/2}, 1d, 2s, 0h_{11/2})$	$^{100}_{50}\mathrm{Sn}_{50}/^{164}_{82}\mathrm{Pb}_{82}$	[32]

1.1.3 NuShellX: shell model calculation software

Out of several computer codes to perform SM calculations, NuShellX has been chosen. Other available codes include ANTOINE [33, 34], NATHAN [33, 34], and MSHELL [35] - each with unique features and Hamiltonian diagonalization schemes. However, the calculation outputs are expected to be consistent with one another given the same input model space, truncations, SPEs and TBMEs. In addition to level schemes, calculated β- and γ-decay half-lives, branching ratios, decay energies, and transition strengths are available outputs to be compared directly with experimental values.

1.2 Decay spectroscopy

Much of the structure of unstable isotopes is deduced from decay processes, a schematic scheme of which is presented in Fig. 1.2. In order to capture as much experimental information as possible, both particle emission spectroscopy (β or p) and γ-ray spectroscopy need to be performed. The following sections describe each process and the underlying physics related to the investigation of nuclear structure in this thesis.

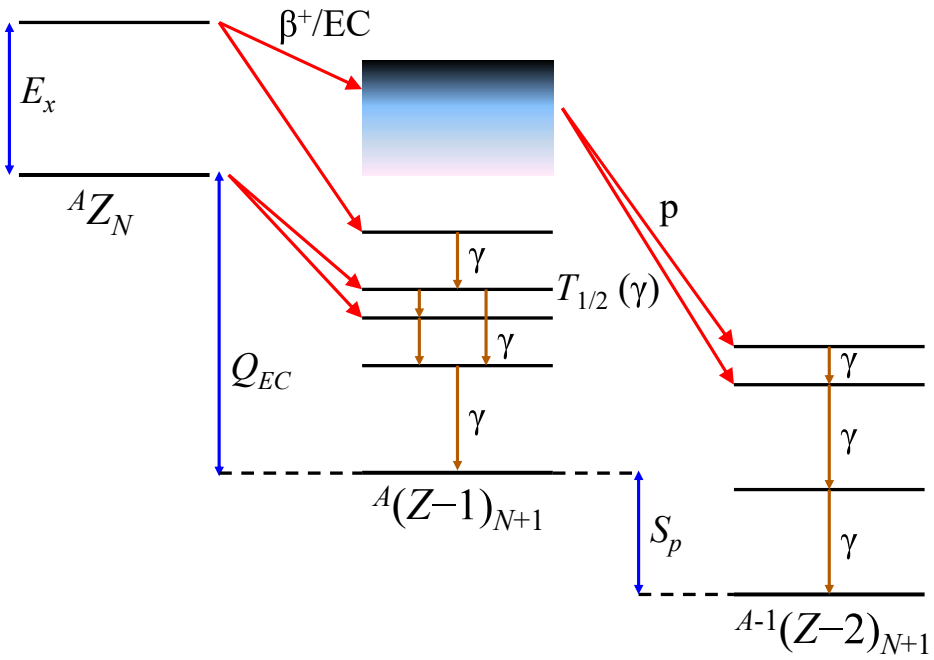

Figure 1.2: Decay processes of a hypothetical proton-rich nucleus with mass number A and proton number Z.

1.2.1 β decay: Fermi and Gamow-Teller

β decay is a weak interaction process where a nucleon in an atomic nucleus changes its type, releasing a β particle and either an electron neutrino ν_e (for β^+ decay) or an electron antineutrino $\bar{\nu}_e$ (for β^- decay). Electron capture (EC) is another decay mechanism available to proton-rich nuclei. β particles and neutrinos are leptons, which are spin 1/2 particles unaffected by the strong interaction. In this thesis, two types of β decays are relevant: positron (β^+) emission and EC. Both processes convert a proton in a proton-rich nucleus into a neutron to increase stability:

$$\beta^+ : p \rightarrow n + e^+ + \nu_e, \tag{1.2}$$

$$\mathrm{EC} : p + e^- \rightarrow n + \nu_e. \tag{1.3}$$

Comparisons of the two equations show that EC has a larger energy window compared to β^+ emission by approximately $2m_e$, or 1.022 MeV (minus the binding energy of the captured electron). However, for a heavy and exotic proton-rich isotope the available decay energy is far larger than this energy window difference and the β^+ decay branch becomes dominant (see Fig. 4.1.3 of Ref. [1]). For most of the nuclei in the ^{100}Sn region, β^+ decay dominates over EC. For the remainder of the thesis, β decays (without the superscript) refer to β^+ decays.

Experimental β decay information in this region of nuclides is not exhaustive. As a result, certain excited states in the daughter nuclei, inaccessible through fusion-evaporation reactions or isomer spectroscopy after fragmentation reactions, may yet to be discovered. A non-comprehensive list of such nuclei (β-decay daughters) includes ^{89}Tc, ^{90}Ru, ^{92}Rh, and ^{98,99}Cd. Additional β-decaying isomeric states are predicted by theory and may be discovered.

For the nuclei of interest, a β decay can be either a pure Fermi (F), a pure Gamow-Teller (GT), or an admixture of both. The properties and differences of the two decay modes are given in Table 1.2.

Table 1.2: Comparisons of the two β-decay modes. Only allowed transition properties are given.

Decay mode	Fermi (F)	Gamow-Teller (GT)
Lepton spins	antiparallel ($\uparrow\downarrow$)	parallel ($\uparrow\uparrow$)
Isospin change ΔT	0	0, ±1
Spin change ΔJ	0	0 (not $0 \rightarrow 0$), ±1
Parity change $\Delta\pi$	0	0

The decay strengths of the two decay modes are related to the product of the phase space integral f, which depends on the β-decay energy and the partial decay half-life t [36, 37]:

$$ft = \frac{K}{G_V^2 B_F + G_A^2 B_{GT}}, K = \frac{2\pi^3 (\ln 2)\hbar^7}{m_e^5 c^4}, \tag{1.4}$$

where G_V and G_A are the vector and axial-vector weak coupling constants. It is common to quote the $\log(ft)$ value of a β decay, which has been shown to reflect the decay selection rules [38]. The transition strengths B_F and B_{GT} correspond to the square of the matrix elements between the initial state $|\psi_i>$ and the final state $|\psi_f>$:

$$B_F = |M_V|^2 = |\langle\psi_f|\hat{\tau}|\psi_i\rangle|^2; \tag{1.5}$$

$$B_{GT} = |M_A|^2 = |\langle\psi_f|\hat{\sigma}\hat{\tau}|\psi_i\rangle|^2, \tag{1.6}$$

where $\hat{\sigma}$ is the Pauli spin matrix operator and $\hat{\tau}$ is the isospin transition operator.

Fermi decay

In Fermi decays the leptons are emitted with antiparallel spins, and $\Delta T = \Delta J = 0$. Therefore, only isobaric analog states (IAS) are populated. The IAS are usually inaccessible in a β decay because the Q_{EC} value is lower than the Coulomb energy difference ΔE_C between the IAS. However, for a proton-rich nucleus near the dripline, $Q_{EC} > \Delta E_C$ and Fermi decay becomes a viable decay mode. For pure Fermi decays, the Fermi strength function B_F is reduced to a isospin ladder operator algebra:

$$B_F = |\langle \psi_f | \hat{\tau} | \psi_i \rangle|^2 = |\langle T, T_z + 1 | \hat{\tau}_+ | T, T_z \rangle|^2 = (T - T_z)(T + T_z + 1) \tag{1.7}$$

for β decays. The isospin T corresponds to half of the number of unpaired nucleons, and $T_z = (N - Z)/2$ of the parent nucleus is its projection. In view of Eq. (1.4), this implies that all pure Fermi decays of the same isospin group must have a constant ft value. This is known as the conserved vector current (CVC) hypothesis, which requires additional corrections (radiative and isospin-symetry-breaking) on the order of 1% to before comparing different nuclei [39]. The ft values with corrections are noted as $\mathcal{F}t$.

Candidate nuclei with significant or pure Fermi-decay components are very exotic $T_z = -1/2$ and odd-odd $T_z = 0$ isotopes. The ground states of $T_z = 0$ nuclei undergo $0^+ \rightarrow 0^+$ superallowed Fermi decays to isobaric analog states, the half-lives and Q_β (β-decay endpoint energy) values of which can be used to test the CVC hypothesis. In particular, $N = Z$ nuclei cease to be stable against proton emission beyond ^{100}Sn, making ^{98}In the heaviest superallowed $0^+ \rightarrow 0^+$ Fermi-decay candidate. With the highest Z and Q_β values, these nuclei are sensitive test cases of the consistency of the corrected $\mathcal{F}t$ value, which may be affected via the Fierz interference term [40]. According to the present literature, precise half-lives with less than 1% relative uncertainties and Q_β or mass measurements with $\delta M/M < 0.1\%$ are required in order to be relevant.

If the CVC hypothesis holds, then the unitarity of the Cabibbo-Kobayashi-Maskawa (CKM) quark-mixing matrix [41] could be tested with the average $\mathcal{F}t$ value $\overline{\mathcal{F}t}$. The unitarity of the CKM matrix implies that all hadronic matter is composed of three generations of quarks (up/down, charm/strange, and top/bottom), and no other types of quarks are present in nature. The mixing between the up and the down quark $|V_{ud}| = G_V/G_F$ of the CKM matrix can be obtained from the following relationship [37]:

$$|V_{ud}|^2 = \frac{K}{2G_F^2(1 + \Delta_R^V)\overline{\mathcal{F}t}} \tag{1.8}$$

$$= \frac{2915.64 \pm 1.08}{\overline{\mathcal{F}t}}, \tag{1.9}$$

where the present literature has $V_{ud} = 0.97417(21)$.

Gamow-Teller decay

In GT decays, allowed transitions may change the isospin and change the spin of the final state by up to one unit. Due to their loose restraints on the selection rules, GT decays are ubiquitous in the chart of nuclides. In general, the B_{GT} value of a GT decay is fragmented across multiple final states and thus cannot be used to learn something about a unique transition. For a pure GT decay with multiple final states, Eq. (1.4) is reduced to

$$B_{GT} = \sum_i \frac{3811.5 \text{ s}}{f_i t_i} \tag{1.10}$$

after having evaluated the constants. f_i and t_i correspond to partial phase space integrals and half-lives, respectively. Experimentally, one must be aware of the pandemonium problem [42] which creates a bias in favor of dominant transitions. Under certain circumstances, however, a dominant population of one final state may be assumed if other states are not easily accessible due to energetics or selection rules. One example for this is ^{100}Sn. In this case one may apply an extreme single particle estimate (ESPE) aided by the SM to predict the theoretical B_{GT} [43]:

$$B_{GT}(ESPE) = \frac{4\ell}{2\ell+1}\left(1 - \frac{N_{\nu g7/2}}{8}\right) N_{\pi g9/2}, \tag{1.11}$$

where $\ell = 4$ for the $g_{9/2}$ orbital, and $N_{\nu g7/2} = 0$ and $N_{\pi g9/2} = 10$ are nucleon occupation numbers for the parent nucleus ^{100}Sn. In this approach, the ESPE B_{GT} is $160/9 \simeq 17.8$, much larger than the experimental value of $9.1^{+2.6}_{-3.0}$ in Table 1.3. Among other causes that result in a lower B_{GT}, it is incorrect to neglect core excitations which would increase $N_{\nu g7/2}$ and decrease $N_{\pi g9/2}$ in the above formula. The phenomenon of the experimental B_{GT} being systematically lower than the ESPE across the nuclear chart is known as GT quenching. A universal quenching factor of 3/4 has been applied to the GT operator to reproduce the experimental B_{GT} values with relative success, which is a testament to the robustness of the SM. However, it would be interesting to increase the knowledge of experimental B_{GT} to validate theoretical interpretations of the GT quenching discussed in Ref. [33].

1.2.2 γ decay and electromagnetic transition strength

A β decay from a parent nucleus may populate the ground state of the daughter nucleus directly, or a set of excited states within the Q_{EC} window. Many excited states in nuclei are then de-excited through γ-ray emission. With high-purity germanium detectors, a precise level scheme of a nucleus may be determined with high-resolution γ-ray spectroscopy and $\gamma\gamma$ coincidence analysis. With sufficient statistics, $\gamma\gamma$ angular correlation analyses may be performed to determine the spins and parities of the excited states.

Similar to EC of the β decay, γ decay may compete with internal conversion (IC) where an atomic electron is emitted in place of the γ ray. In this case, the emitted electron energy is equal

to the transition energy minus the binding energy of the electron orbital. During this process, Auger electrons [44] may also be emitted. An IC branch becomes more viable as the transition energy decreases, and/or the minimum multipolarity of the γ-ray transition increases. This ratio is denoted by the IC coefficient $\alpha = \lambda_e/\lambda_\gamma$, where λ_e and λ_γ are decay branching ratios of IC and γ-ray decays, respectively. For a $0 \rightarrow 0$ transition, only the electric monopole ($E0$) IC is possible.

Isomeric γ-ray transitions

Every state in atomic nuclei possesses its unique spin and parity J^π, and a γ-ray transition from an excited state must obey the selection rule: $|J_f - J_i| \leq \ell \leq J_i + J_f$. γ-ray emission is hindered for large ℓ and small E_γ such that the half-life of an excited state may be orders of magnitude higher than 10^{-12} s (see cases (c) and (d) of Fig. 1.4). With the exception of extreme hindrance for γ rays which result in a dominant β-decay branch, γ-ray transitions with half-lives on the order of ns to μs are measurable with standard detectors. Then the electromagnetic transition strength $B(\sigma\ell)$ of an isomeric γ-ray decay can be determined with the multipolarity $\sigma\ell$, the transition energy E_γ, the half-life $T_{1/2}$, and the branching ratio b. Experimental $B(\sigma\ell)$ then can be used to test the robustness of SM calculations in various types of isomers and their γ-decay properties. A formula for $B(\sigma\ell)$ in terms of the multipolarity constant $K(\sigma\ell)$ and the experimental observables is:

$$B(\sigma\ell) = K(\sigma\ell)E_\gamma^{-(2\ell+1)}\left(\frac{\ln 2}{T_{1/2}}\right)\left(\frac{b}{1+\alpha}\right), K(\sigma\ell) = \frac{(\hbar c)^{2\ell+1}\ell[(2\ell+1)!!]^2\hbar}{8\pi(\ell+1)}. \tag{1.12}$$

Electromagnetic transition strengths are usually represented in Weisskopf units (W.u.), which is a coarse order-of-magnitude estimate of the nuclear collectivity involved in the transition. Two simplifications are made to approximate the transition matrix element: setting the angular integral to be one, and assuming a constant radial wavefunction for the radial integral. For electric transitions from a nucleus with mass A, one W.u. corresponds to

$$B^W(E\ell) = \frac{1}{4\pi}\left(\frac{3}{\ell+3}\right)^2 e^2 R_0^{2\ell}, \tag{1.13}$$

where $R_0 = A^{1/3}r_0 = (1.2)A^{1/3}$ fm is the average nuclear radius. For magnetic transitions,

$$B^W(M\ell) = \frac{10}{\pi}\left(\frac{3}{\ell+2}\right)^2 \mu_N^2 R_0^{2\ell-2}, \tag{1.14}$$

where $\mu_N = e\hbar/(2m_p)$ is the nuclear magneton. More information on the electromagnetic transitions is found in Appendix B.

1.2.3 Proton emission

Binding energy (or mass), one of the macroscopic properties of nuclei, may be investigated experimentally with spontaneous nucleon emission. Many proton-rich nuclei that were produced in this

experiment have proton separation energies S_p less than the β-decay Q-value and thus excited states with excitation energies E_x greater than S_p may be populated in the daughter nucleus as illustrated in Fig. 1.2. Consequently, β-delayed proton (βp) emission is possible. For certain states the Q_p value exceeds the initial and the final state energy difference, enabling direct proton emission.

1.3 Structure of ^{100}Sn and nuclei in its vicinity

^{100}Sn is located far northwest of the stable isotope ^{102}Pd in the Segrè chart of nuclides (see Fig. 1.3) and borders the predicted proton dripline. Suggested from the figure are several undiscovered isotopes (empty squares below, or on the right side of the dripline) that may be stable against spontaneous proton emission. Experimental information on nuclei in the ^{100}Sn region are needed to confirm the dripline prediction and test the robustness of SM predictions in the most proton-rich environment.

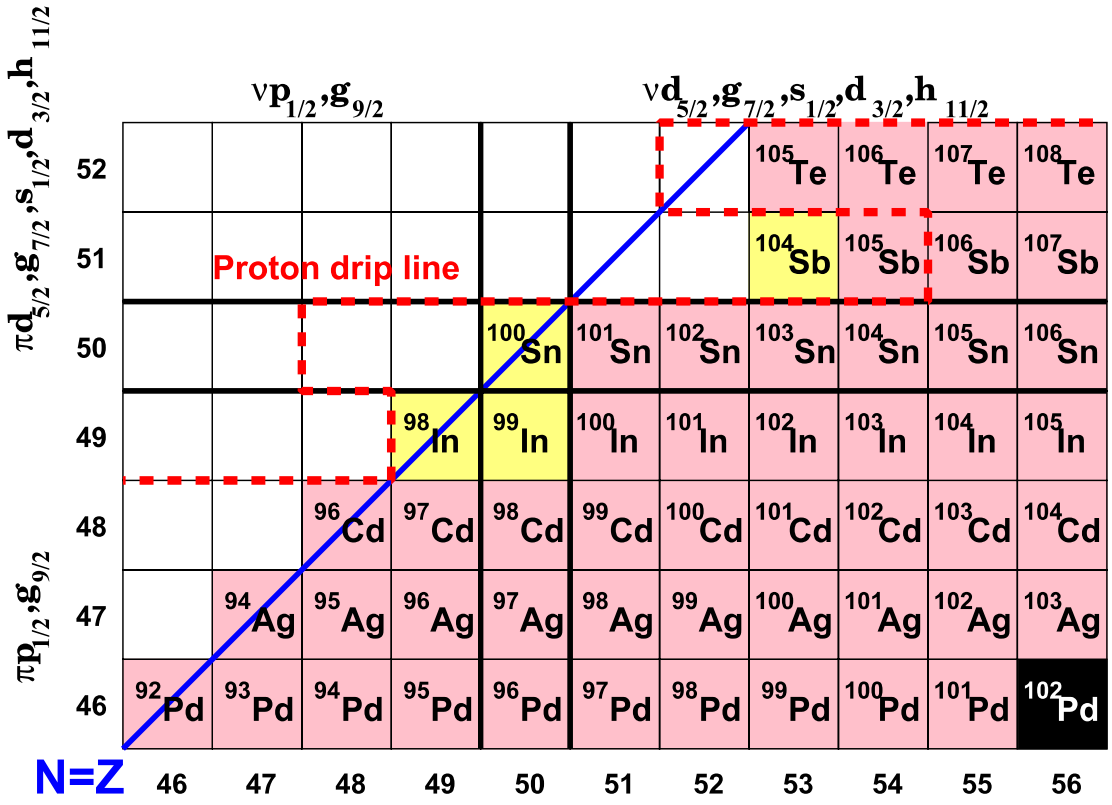

Figure 1.3: Segrè chart of nuclides around ^{100}Sn, displaying radioactive nuclei with known half-lives (yellow), half-lives and excited states (red), and stable ^{102}Pd (black). A theoretical proton dripline is drawn in red dashed lines. This figure is taken from Ref. [1].

1.3.1 Doubly magic nucleus ^{100}Sn

^{100}Sn is the heaviest $N = Z$ doubly magic nucleus, with Section 1.1.1 providing a basis for 50 being a magic number. This nucleus plays a key role in understanding the nuclear structure in the context of the shell model. Experimental and theoretical knowledge of ^{100}Sn and nuclei in its vicinity are discussed in the following sections.

Superallowed Gamow-Teller decay of ^{100}Sn

^{100}Sn is bound against proton emission and undergoes a superallowed GT decay which has the smallest $\log(ft)$ value [14] in any nuclear β decay. In corollary, the GT-decay strength B_{GT} is the largest among thousands of known β decays. The underlying experimental values of the ^{100}Sn are given in Table 1.3. This enables a unique opportunity to compare the experimental B_{GT} value to theoretical predictions without much of the GT-decay strength being lost due to a finite β-decay energy window Q_{EC}.

Table 1.3: Average experimental values of ^{100}Sn's β decay compiled from previous experiments.

Observable	Average value	Refs./notes
$T_{1/2}$	1.09(18) s	[14, 45, 46]
$Q_{EC} - E_x$	$4.35^{+0.19}_{-0.17}$ MeV	[14, 46]
B_{GT}	$9.3^{+2.3}_{-3.0}$	all combined
	$9.1^{+2.6}_{-3.0}$	[14] alone

The most significant experimental uncertainty of the B_{GT} value comes from the uncertainty of the Q_{EC} value, where the phase space integral f mentioned in Eq. (1.10) depends on the 5th power of Q_{EC}. To improve the precision of the Q_{EC} value, mass spectrometry or high-statistics β-decay spectroscopy measurements are required.

Level scheme of ^{100}In

Determining the correct level scheme of ^{100}In, the β-decay daughter nucleus of ^{100}Sn, is essential for ^{100}Sn's experimental $\log(ft)$ and B_{GT} values. Three different level schemes have been proposed by independent models [15, 16, 47], and two of them hold reasonable validity according to the dissertation work by C. B. Hinke [48]. Of those two, the preferred level scheme is presented in [14]. The ambiguity is caused by the non-observation of weak γ-ray transitions in one of the proposed level schemes, and is discussed in Section 4.4.7.

Excited states of ^{100}Sn

No experimental information exists for the excited states of ^{100}Sn, where the energies of the low-spin excited states would be valuable in addressing the discrepancies of theoretical predictions. A seniority (nucleons not paired to spin 0; see the excited states of Fig. 1.4 (d)) isomer has been

predicted for the 6^+ state in ^{100}Sn among various models [49–51] with a half-life ranging from 90 ns to 2.6 μs, which would help preserve the γ-ray transitions for delayed spectroscopy until the ^{100}Sn isotopes in an in-flight facility pass through the separators and identification detectors. The results of the search for an isomer in ^{100}Sn are presented in Section 4.2.2.

1.3.2 Proton-neutron interaction in the $g_{9/2}$ orbitals

^{100}Sn and nuclei in its vicinity have equal or approximately the same numbers of protons and neutrons, and the ability to describe their structure depends heavily on the knowledge of isoscalar ($T = 0$) and isovector ($T = 1$) interactions among the nucleons in this region. An attractive $T = 0$ interaction is available only to proton-neutron (pn) pairs with aligned spins, while $T = 1$ interactions are present in all of pp, pn, and nn pairs with anti-aligned spins.

In the $g_{9/2}$ orbital, the pn interaction is most clearly demonstrated in $N = Z$ nuclei due to the closest overlap of the proton-neutron wavefunctions and the maximum number of pn pairs available for the valence nucleons. This is corroborated experimentally with high-spin isomers: (7^+) and (21^+) in ^{94}Ag [52], and (16^+) in ^{96}Cd [8]. The $(25/2^+)$ isomer in ^{97}Cd [53] can be understood as an unpaired $g_{9/2}$ neutron with a spin projection $K = 7/2$ filling one of the two pn hole pairs generating the (16^+) isomer in ^{96}Cd. The $T = 0$ pn interaction is also responsible for an accurate theoretical description of the experimental level scheme of a $N = Z$ nucleus ^{92}Pd [54], in contrast to the level scheme of a $N = 50$ magic nucleus ^{96}Pd [55] where the dominant component of the low-spin states' wavefunctions is based on the $T = 1$ pp interaction. The current theories of pn interactions near ^{100}Sn can be examined more carefully with more robust experimental data.

1.3.3 Limit of proton binding at $Z \leq 50$

Different mass models predict limits on proton binding of nuclei around ^{100}Sn, but they have not been fully tested with experimental data. An overview of β-delayed proton emitters in the vicinity of ^{100}Sn was presented in Ref. [56] with an impact on a certain scenario for the rp-process. A controversial report on the observation of direct two-proton emission in ^{94}Ag [11] was challenged by Refs. [57, 58] on the basis of experimental apparatus and level scheme of the $2p$ daughter ^{92}Rh, respectively. Another investigation of ^{94}Ag isomers confirmed a $1p$ emission at $Q_p = 790(30)$ keV, but found neither the second 1p branch at $Q_p = 1010$ keV nor the signature of $2p$ emission [59]. It is of interest to confirm ^{94}Ag as the first and only odd-Z $2p$ emitter. The results from this experiment are discussed in Section 4.3.5.

Some of the most exotic nuclei are $T_z = -1/2; N = Z - 1$ species, which for $40 < Z \leq 50$ are on the edge of the proton dripline based on various mass predictions. From the literature on these nuclei [60–62], many odd-Z nuclei appear to be proton unbound based on their sub-microsecond half-lives. For even-Z nuclei, half-lives on the order of 10 ms are expected with $\Delta J = 0$, mixed Fermi/GT β decays to their daughter nuclei. Better half-life measurements would provide clearer borders of the proton dripline; Q_β measurements would be a more sensitive test of the mass calculations.

1.3.4 $N = 50$ shell gap, single particle energies

The spin-orbit coupling which brings down the $g_{9/2}$ orbital close to the $p_{1/2}$ orbital results in both the formation of the shell gap at the magic number 50 and an increasing proximity of the two orbitals. $\Delta J = 4$, a parity difference, and a small energy gap results in a hindrance of γ decays between these orbitals such that low-energy $1/2^-$ states may be β-decaying isomers. These predictions are elaborated in Refs. [13, 63].

Two core-excited isomers in ^{98}Cd [64] and ^{96}Ag [65] reveal the closeness of the neutron $g_{7/2}$ and the $d_{5/2}$ orbitals, which is the cause of hindered $E2$ transitions in parallel with $E4$ transitions bridging the shell gap. In addition to the spin-gap isomers formed by the $T = 0$ pn interaction, other examples of isomers are exhibited in Fig. 1.4.

^{101}Sn has one extra neutron added to the ^{100}Sn nucleus, and is an excellent probe to study the SPEs of the $g_{7/2}$ and the $d_{5/2}$ orbitals above the $N = 50$ shell gap. The ground state spin of ^{101}Sn has been a controversial topic due to the onset of degeneracy between the aforementioned orbitals. A study on the α-decay chain to ^{101}Sn places the $g_{7/2}$ orbital below the $d_{5/2}$ orbital by 172(2) keV [66], in conflict with another experiment which proposed the reverse order [67]. It would be important to determine the order of the two orbitals for ^{101}Sn to test the effects of the two-body tensor force [68] that is evident in many exotic nuclei with unbalanced Z/A ratios.

1.4 Thesis objective

This thesis presents results from a decay spectroscopy experiment aimed at establishing energy, spin and parity assignments of ground and excited states of nuclei around ^{100}Sn, validating or challenging SM predictions. Both β-decay and electromagnetic transition strengths determined from this experiment allow for more stringent tests of transition matrix elements calculated from SM models with different model spaces. Measured half-lives, decay Q-values and βp branching ratios are presented as valuable inputs for rp-process calculations and mass evaluations. The limit of the proton dripline in the $Z \sim 50$ region is investigated with experimental data on the most neutron-deficient isotopes.

For the doubly magic ^{100}Sn and its decay, more specific aims are covered in this thesis. First, improvements in the precision of $T_{1/2}$ and Q_β of ^{100}Sn β decay are presented, which in turn establish a more sensitive test of the SM prediction on ^{100}Sn's B_{GT} value. The literature level schemes of ^{100}In are reviewed with higher-statistics γ-ray data, with emphasis on γ-ray intensities and unobserved transitions that are essential to disambiguate the proposed level schemes. Finally, research on a hypothetical isomer in ^{100}Sn is discussed in relation to the level scheme of the ^{100}Sn itself.

A parallel but independent analysis of this data has been carried out by D. Lubos [69] at Technische Universität München, with varying degrees of emphasis on different topics to validate the consistency of the results.

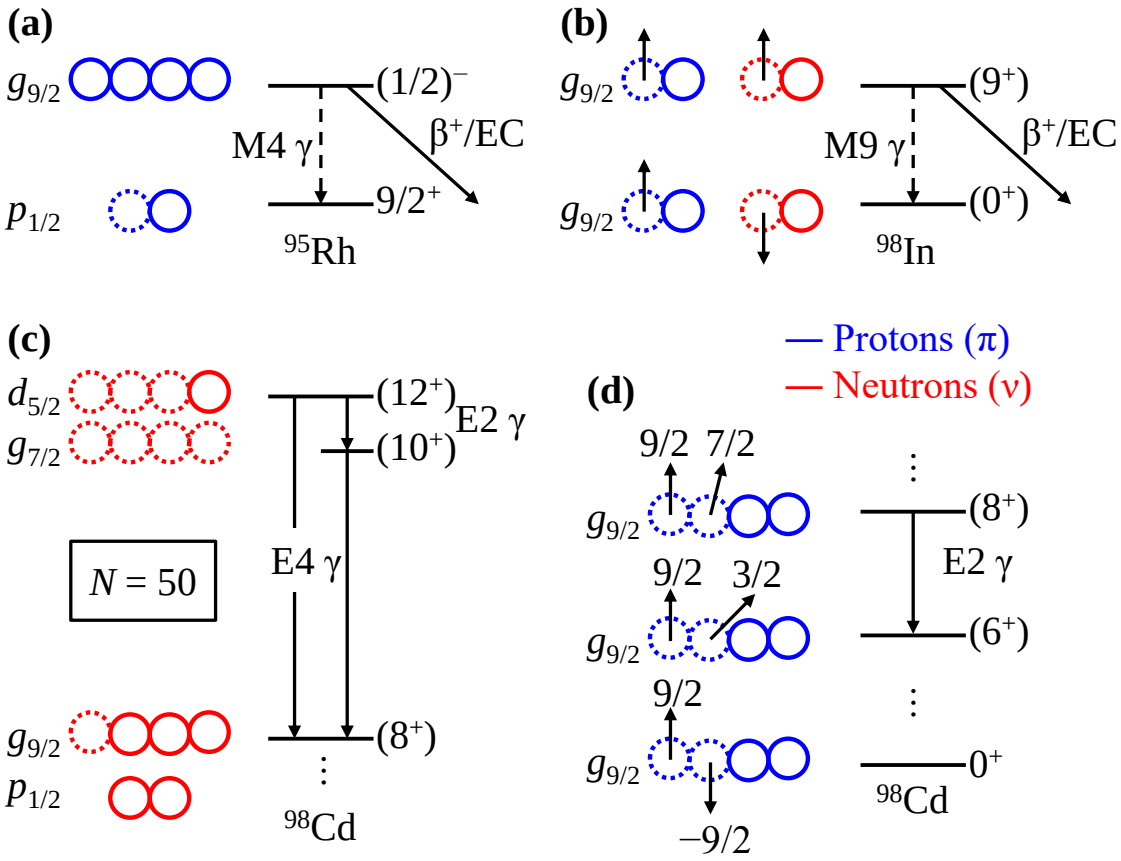

Figure 1.4: Different types of isomers present in the nuclei of interest: (a) negative-parity isomer formed by a promotion of a proton from the $p_{1/2}$ orbital into the $g_{9/2}$ orbital; (b) spin-aligned pn pair with an attractive $T = 0$ interaction; (c) core-excited spin-gap isomer, where a neutron is excited across the $N = 50$ shell gap; (d) lowest-energy spin states with a small transition energy. Hindered γ-ray transitions are labeled with their multipolarities. Each type of isomer has a rather pure wavefunction, allowing unambiguous extractions of SPEs and TBMEs of nuclei in its vicinity.

1.5 Outline of the thesis

The introduction is followed by the description of the experiment method in Chapter 2, including the isotope production mechanism, the particle identification (PID) scheme, the detector setup, and the data acquisition configuration. Chapter 3 is dedicated to the data analysis methods: ion implantation-decay event reconstruction and correlation, silicon and germanium detector calibrations in time and energy, and strategies to determine key experimental quantities such as half-lives and β-decay endpoint energies. A comprehensive set of results are categorized and listed in Chapter 4, including relevant discussions of the results in comparison to theoretical predictions. Final remarks and outlook on future experiments to enhance the understanding of nuclei in the ^{100}Sn region are given in Chapter 5.

Chapter 2

Experiment method

The decay spectroscopy experiment was performed in June 2013 at RIKEN Nishina Center and its Radioactive Isotope Beam Factory (RIBF) in Japan. This chapter is dedicated to the description of RIBF, the experimental setup, and the detector/data acquisition systems.

2.1 Isotope production and separation at RIBF

Commissioned in March 2007, RIBF [70] at RIKEN employs in-flight production of radioactive isotopes by projectile fragmentation of heavy ion beams. In comparison to other radioactive isotope research facilities, RIBF's high primary beam intensity enables the production of many exotic nuclei to be studied in detail for the first time in the world. Featuring also powerful separation and identification systems named BigRIPS and the ZeroDegree spectrometer, RIBF was an ideal facility to investigate the nuclei around ^{100}Sn.

2.1.1 Radioactive isotope production

A brief overview of the method to produce exotic radioactive isotopes in the vicinity of ^{100}Sn at RIBF is given below. More details of the isotope production, including discussions of production cross sections and comparisons to simulations, are found in Ref. [71].

Primary beam acceleration

The lightest stable isotope of xenon, $^{124}_{54}$Xe ($T_{1/2} \geq 1.6 \times 10^{14}$ years [72]) was chosen as the primary beam in order to maximize the production cross section of neutron-deficient isotopes with $Z \sim 50$. ^{124}Xe atoms in a gas were ionized with the 28-GHz superconducting electron cyclotron resonance ion source (SC-ECRIS [73]) up to the charge state 18+ ($A/q \approx 6.8$) before being injected into the RIKEN Heavy-ion Linac 2 (RILAC2) commissioned in 2011.

RIBF features a chain of cyclotrons which are operated in different modes depending on the primary beam type (see Fig. 2.1). The ^{124}Xe beam from the RILAC2 with an initial energy of 670 keV/u was accelerated through the RRC (RIKEN Ring Cyclotron), fRC (fixed-frequency Ring Cyclotron), IRC (Intermediate-state Ring Cyclotron), and the SRC (Superconducting Ring Cyclotron) up to 345 MeV/u. A sufficiently high charge state was required as the ^{124}Xe ion beam passed through the cyclotrons, which was achieved by the helium-gas charge strippers between the acceleration stages. The final primary beam charge state was 52+.

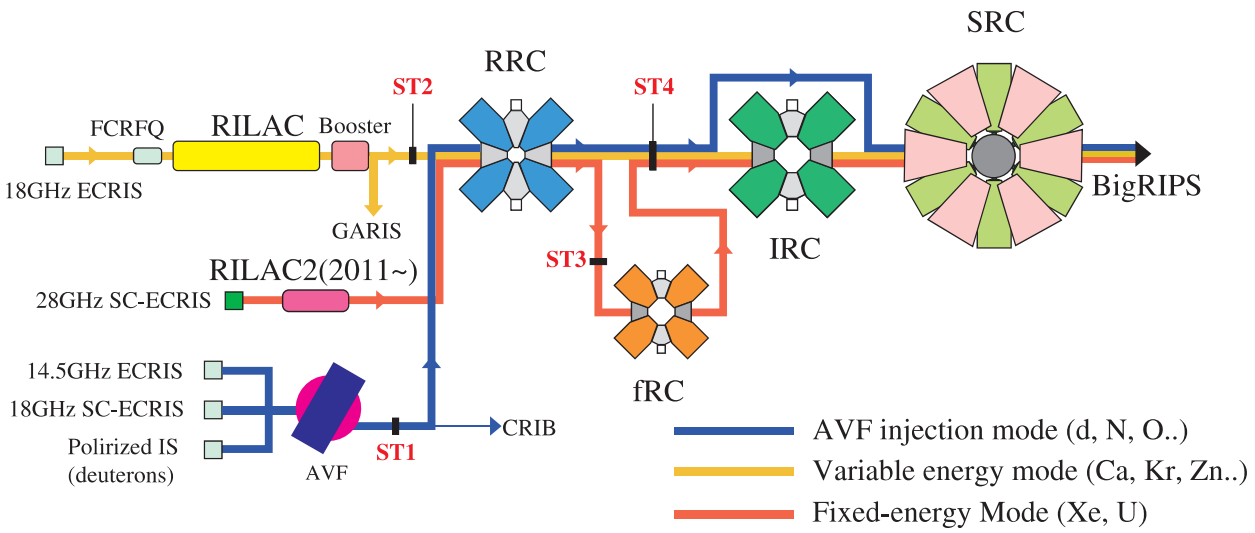

Figure 2.1: Schematic layout of RIBF, featuring different acceleration modes. The ^{124}Xe ion beam from SC-ECRIS was accelerated through RILAC2 and the four cyclotrons in the fixed-energy mode. ST3 and ST4 represent the locations of the charge strippers, which enable greater acceleration of the ion beam through the fRC and the IRC. This figure was taken from Ref. [4].

Fragmentation reaction

In this experiment, the production of neutron-deficient $Z \sim 50$ isotopes was achieved by fragmentation reactions of the ^{124}Xe beam on a 4-mm ^{9}Be target (thickness equivalent to 740 mg/cm^2). Beryllium was chosen for its high production cross section and small energy loss/straggling due to its low mass. While a thicker target would enable a higher production rate of the radioactive isotopes, they would also introduce a poorer momentum resolution of the RI beam - leading to a lower transmission efficiency. Thus the optimal thickness was determined with LISE++ simulations [74] and from tests with different thicknesses of the ^{9}Be target before the main experiment [75].

There is a distribution of charge states q for the fragmented isotopes, which is dependent on the primary beam energy and the target's properties. Since the magnetic rigidity depends on q and not the nuclear charge Z, same isotopes with different charge states would have different trajectories through BigRIPS. For the 345-MeV/u primary beam and the 4-mm thick ^{9}Be target, it was found that the majority of radioactive ions would be fully stripped of their electrons [75] such that $q = Z$. Due to the high RI beam intensity and the large beam acceptance required for a wide range of Z, isotope separation and identification settings were set to accommodate only the fully ionized species.

2.1.2 Separation and identification

Fragmentation reactions produce highly energetic radioactive isotopes with production cross sections varying several orders of magnitude as a function of A and Z; the difficulty of producing exotic

nuclei scales with the imbalance of Z/A ratios. In order to conduct experiments on exotic nuclei produced by the fragmentation method, the products of interest have to be separated from a large pool of unwanted, less exotic species and identified of their A and Z on an event-by-event basis. At RIBF, separation and identification of individual isotopes were performed by BigRIPS and the ZeroDegree spectrometer [76, 77]. The sections below illustrate the basic principles of separation and identification of the RI beam. A schematic diagram illustrating the RI beam's path through BigRIPS and the ZeroDegree spectrometer before being implanted at the decay spectroscopy station is shown in Fig. 2.2.

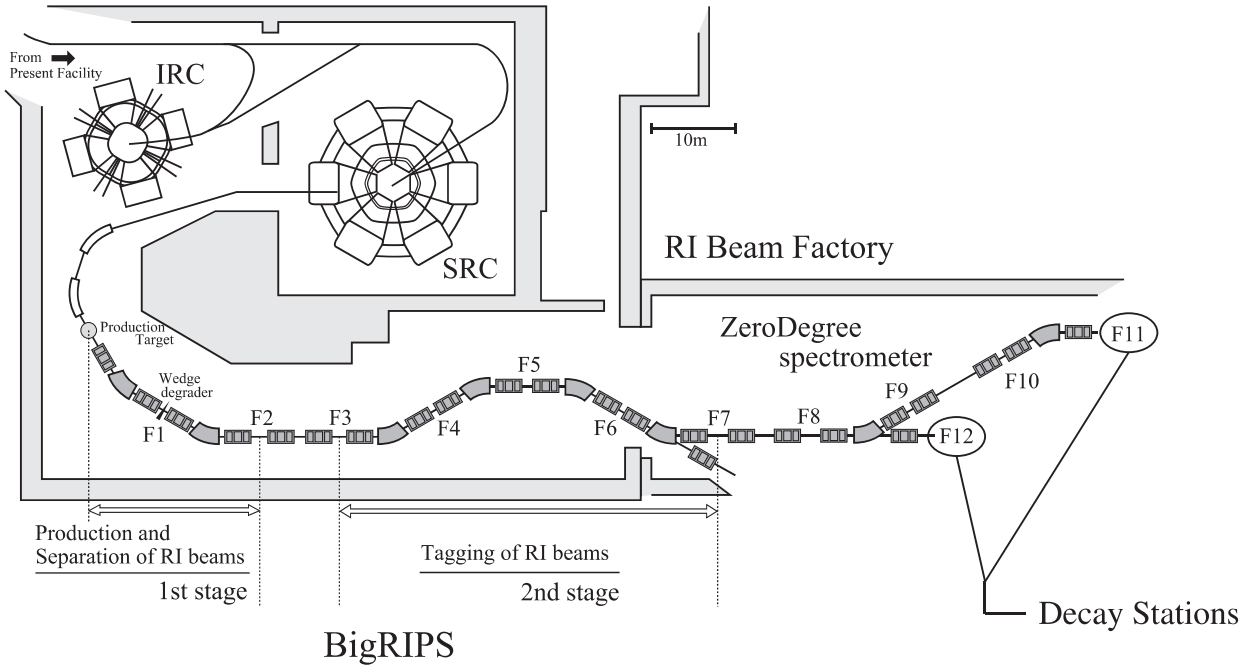

Figure 2.2: Layout of BigRIPS in conjunction with the ZeroDegree spectrometer. This schematic diagram of RIBF was taken from Ref. [5]. The decay spectrometers for the experiment were placed after F11.

Separation of unwanted species

In order to limit the rate at which the RI beam passes through the identification detectors and becomes implanted at the decay station, only the species of interest must be transmitted through BigRIPS and the ZeroDegree spectrometer. This was achieved by a two-stage isotope separation method [78, 79] using wedge degraders made of aluminum. The wedge degraders featured position-dependent thicknesses so that the radioactive isotopes with different position profiles incurred different energy losses while traveling through the degraders. The energy loss was also proportional to Z^2 as described by Eq. (2.3). Therefore the nuclei with small ΔE were deflected at the subsequent dipole magnet with large bending radii due to their large momenta. In the opposite case of large ΔE, the resulting bending radius was small. Compared to the isotopes of interest, the position

distributions of the other species were shifted further away from the reference path. Slits placed at the outer edges of a focal plane then stopped a significant fraction of the unwanted beam while preserving most of the isotopes worthy of investigation. The two-stage separation method effectively removed contaminants due to changes in the charge state of the RI beam and the secondary reaction products generated after the first degrader. The first Al wedge degrader with a 3-mm maximum thickness was placed at the F1 focal plane in Fig. 2.2. The second Al wedge degrader was placed at F5, with a slightly lower maximum thickness at 2.2 mm.

Particle identification

The TOF-$B\rho$-ΔE method and the instruments used to identify individual isotope's A and Z are presented below.

Time-of-flight measurement The first intermediate quantity required to perform PID was the speed of each ion: $\beta = v/c$. β was needed to determine both the mass-to-charge ratio A/q and the nuclear charge Z, and was deduced from the time-of-flight (TOF) measurement between two fixed locations within BigRIPS with a known path length L:

$$\beta = \frac{1}{c}\frac{L}{\mathrm{TOF}}. \tag{2.1}$$

Two plastic scintillators coupled with photomultiplier tubes were placed at F3 and F7 of Fig. 2.2, acting as the start and the stop time measurement stations with a good timing resolution ($\delta\beta/\beta =$ 0.017% for ions at 300 MeV/u, equivalent to $\beta = 0.65$ [76]). The path length between F3 and F7 was 46.6 m.

Determination of mass-to-charge ratio An ion with a mass number A and a charge state q traveling through a dipole magnet with its field strength B is deflected by the Lorentz force, resulting in the following relationship:

$$\frac{A}{q} = B\rho\frac{c}{\beta\gamma m_u}, \tag{2.2}$$

where $\gamma = (1-\beta^2)^{-1}$ is the Lorentz factor and ρ is the bend radius. $m_u = 931.5$ MeV/c^2 is a constant unit of atomic mass. Along with β from the TOF measurement, the magnetic rigidity $B\rho$ was determined experimentally from nuclear magnetic resonance probes to measure B and position-sensitive parallel plate avalanche counters (PPACs) [80] to measure ρ. Two sets of PPACs were placed at each of F3, F5, and F7, allowing trajectory reconstructions [81–83] for ρ after each bending section of BigRIPS. Combining the measurements at multiple focal planes allowed the A/q ratio to be deduced with good resolution, where the relative uncertainty in A/q was less than 0.1% [75]. Isotopes with different Z but identical A/q ratios could not be distinguished with this method alone, so the ΔE measurements were performed to determine Z.

Determination of nuclear charge Z In order to determine the radioactive isotopes' Z, a multi-sampling ionization chamber (MUSIC) [84] was placed at F11, just in front of the decay station. The energy loss of a relativistic ion with nuclear charge Z in matter is governed by the Bethe-Bloch formula [85]:

$$-\left\langle \frac{dE}{dx} \right\rangle = \frac{4\pi e^4 Z^2}{m_e \beta^2 c^2} N z \left[\ln\left(\frac{2 m_e \beta^2 \gamma^2 c^2}{I} \right) - \beta^2 \right], \tag{2.3}$$

where z, N and I are the atomic number, the atomic density, and the mean ionization potential energy of the ionization material, respectively. The ionization material was a gas mixture of Ar-CH_4 (90% and 10% composition, respectively, for a $> 99.99\%$ purity). The geometric average of multiple ΔE measurements from the MUSIC detector was combined with the velocity β obtained from the TOF measurement to calculate each isotope's Z, culminating in an unambiguous identification of the RI beam's species. The results of the isotope production and identification are presented in Section 4.1.

2.2 Decay spectroscopy setup

Described in this section are the detector systems deployed to perform decay spectroscopy measurements of the fully separated and identified isotopes. The specifications, characteristics, and motivations of each system are discussed, followed by a description of the data acquisition scheme.

2.2.1 WAS3ABi: ion, β particle and proton detectors

The Wide-range Active Silicon-Strip Stopper Array for Beta and ion detection system (WAS3ABi) [5, 86] was used for multiple purposes. Being a semiconductor with a small band gap of 1.1 eV and electron-hole pair creation energy of 3.6 eV, silicon offers good energy resolution for low-energy charged particles (50 keV FWHM for $E < 1$ MeV) at an economic cost. Being reverse-biased at approximately 250 V, they were maintained at 10°C with a cool and dry nitrogen gas to reduce electronic noise. Besides serving as an active implantation detector for the RI beam, it was used to measure times and energies of the emitted particles from decays: β particles and protons. Experimental observables arising from WAS3ABi measurements were half-lives of the isotopes and particle-decaying isomeric states, and proton/β-decay energies for Q-values of the decays. Internal conversion electron (ICE) energies and times were also measured with WAS3ABi, which were crucial in determining the transition strengths of isomeric states in ^{95}Ag (see Section 4.2.1 for details).

XY detector

The XY detector was the most upstream Si detector with a 0.3-mm thickness and having 60 by 40 strips in X and Y directions, respectively. The XY detector featured chains of discrete, position-dependent resistors in a grid formation to diagnose the incoming RI beam's 2D position profile.

Double-sided silicon strip detectors (DSSSD)

Three DSSSDs made by Canberra (Model PF-60CT-40CD-40*60) were used in this experiment. They were initially designed for the SIMBA detector [48] in the ^{100}Sn experiment campaign at GSI Helmholtzzentrum für Schwerionenforschung in Germany. Si strips with 1-mm widths segmented the X and the Y sides of each DSSSD, defining a $60\times40\times1$ mm^3 implantation zone (1-mm thickness) for the incoming radioactive ions. The fine segmentation helped to reduce random background spatial correlations of implanted ion events to decay events. As the ions with dozens of MeV/u arrived at WAS3ABi, they were stopped abruptly in one of the three DSSSDs. The kinematics of the RI beam was calculated in advance with LISE++ and moderated by supplementary Al degraders to control the implantation depth. All of the remaining kinetic energy of the ions was deposited in the Si strips, whose energy profiles were clearly distinguishable from β-decay and proton emission events, whose ΔE were less than 10 MeV. The spacing between the DSSSDs was maintained at 0.5 mm with metal washers.

All the strip channels were connected to charge-sensitive preamplifiers (CS AMP-3), shaping amplifiers (CAEN 568B), and analog-to-digital converters (ADCs; CAEN V785) for energy measurements. The X-side strip channels were connected to a different ADC than the Y-side strips, and only the X-side strip channels were connected to the time-to-digital converter modules (TDC; CAEN V1190). The TDC readout values would later be used for precise determination of the implantation position in the X-direction, described in Section 3.3.1.

Single-sided silicon strip detectors (SSSSD)

A stack of 10 SSSSDs was deployed downstream of the three DSSSDs for energy measurements of β-decay particles. The dimensions of the SSSSDs were identical to those of the DSSSDs, but the SSSSDs were segmented more coarsely. Unlike the DSSSDs which required fine position resolution for implantation-decay correlations, each SSSSD was segmented into 7 strips on the X-side only; the Y-side was not segmented. The same electronics mentioned in the previous section were used to measure energy deposits in the SSSSD channels. The TDC modules were not connected to the SSSSD channels.

Due to the finite kinetic energy of the RI beam, the SSSSDs could not be placed upstream of the DSSSDs; this removed almost a 2π solid angle coverage for proper β-decay calorimetry measurements. In addition, β particles deposit about 400-500 keV per mm in Si at $E_\beta < 10$ MeV with large scattering angles. High-energy β particles, even traveling downstream through the SSSSDs, may escape without depositing their full energies. To address the geometry limitations preventing accurate energy measurements of β particles, methods using Geant4 simulations to determine Q_β values are presented in Section 3.5.2. The WAS3ABi setup is shown in Fig. 2.3.

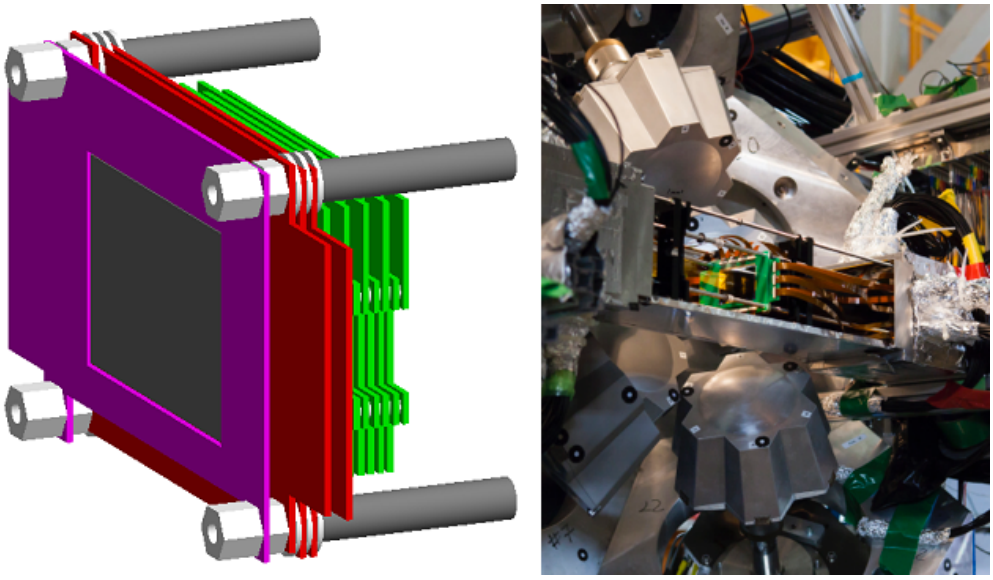

Figure 2.3: Left: model of WAS3ABi with the XY detector used in the Geant4 simulation. Only parts of the fully simulated geometry are shown for clarity. Right: photo of the actual WAS3ABi detector surrounded by the HPGe detectors of EURICA.

2.2.2 EURICA: HPGe γ-ray detectors

EURICA is an acronym for Euroball-RIKEN Cluster Array, which was used to perform γ-ray spectroscopy measurements to study the excited states of the implanted radioactive isotopes and their decay daughter nuclei. For unpolarized radioactive isotopes stopped in the implantation zone, the γ-ray emission profile is isotropic. Hence EURICA surrounded WAS3ABi with a 4π solid angle coverage.

The Euroball detector [6, 87], the progenitor of EURICA, features high-purity germanium (HPGe) cluster detectors in hexagonal tapered coaxial geometry (see Fig. 2.4). HPGe boasts in its excellent energy resolution, aided by its small band gap energy of 0.7 eV and electron-hole pair creation energy of 2.9 eV. Featuring higher material density and number of electron-hole pairs created per MeV than Si detectors, it is the ideal material to perform γ-ray spectroscopy on stopped beams. The RISING setup at GSI [48, 88], using the same Euroball detectors, conducted the latest spectroscopy experiments on ^{100}Sn and the nearby isotopes. The HPGe clusters were then moved to RIKEN in 2011 for exotic decay spectroscopy experiment campaigns.

Charge collection waveforms were analyzed online by the digital gamma finder (DGF; Xia DGF-4C) to determine the energy of the γ rays. Only 47 out of 84 mounted HPGe detectors were fully functional during the experiment, due to an unintended interruption of the periodic liquid nitrogen fills. As the detectors warmed up under the high-voltage bias, their leakage currents rose to sufficiently high levels such that many channels of the front-end electronics were permanently damaged. EURICA's γ-ray detection efficiency loss negated some of the gains in statistics provided by the intense RI beam.

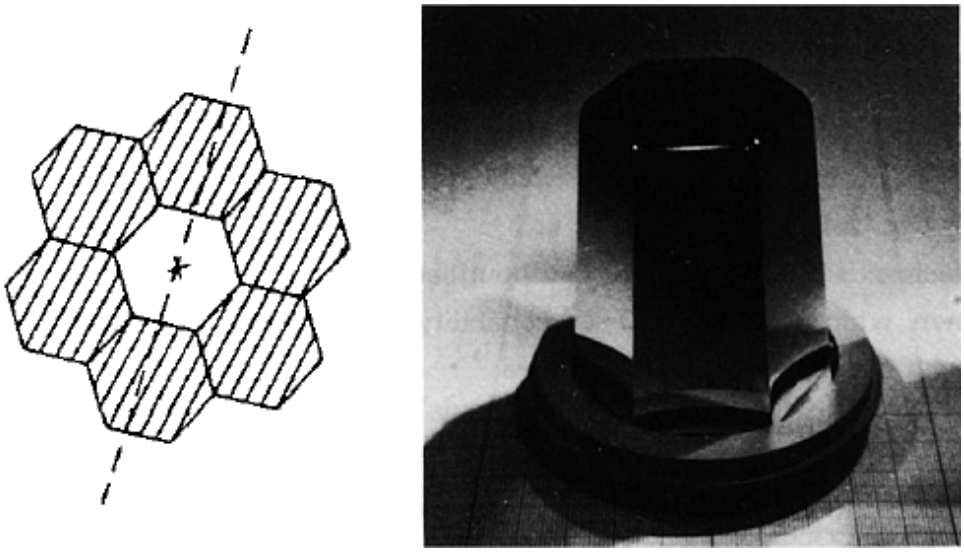

Figure 2.4: Left: front geometry of crystals in a Euroball cluster detector. Right: photograph of the first hexagonal tapered Ge detector. These figures were taken from Ref. [6].

Time measurement

In order to determine half-lives of excited states decaying by γ-ray emission, the γ-ray times were measured in two separate streams within EURICA: one from the DGF, which also handled energy measurement as mentioned above, and another from the TDC. The DGF time was provided from the looping clock with a 40-MHz frequency, leading to an intrinsic time step of 25 ns. The TDCs were tuned such that calibration slopes were less than 1 ns per channel, leading to a better time resolution. However, the timing filter amplifier for TDC data performed poorly at low energies compared to the DGF. Consequently, the detection efficiency decreased at low γ-ray energies if one requested for meaningful TDC data in the offline analysis. Hence the two streams provided complementary options for low-energy γ rays: high efficiency with poor timing resolution (DGF), or low efficiency with good timing resolution (TDC). At sufficiently high energies (> 700 keV), however, no such compromise was needed as all the measured γ rays contained good TDC information. The efficiency discrepancy between the two timing data streams as a function of γ-ray energy is shown in Fig. 3.7.

2.2.3 Data acquisition triggering scheme

Specific trigger conditions, logic conditions and gates were necessary for the data acquisition (DAQ) system to collect relevant data from multiple detector systems. The connections are summarized in a block diagram shown in Fig. 2.5. The master trigger was provided by the OR logic signal of the plastic scintillator at F11 (for incoming ion implantation) and any one of the DSSSDs (decay event). The master trigger opened the gates for energy and time measurements, and it provided reference start times for the TDC modules of the DSSSD channels and the HPGe channels. The

TDCs recorded the time difference $\Delta T = T_{stop} - T_{start}$.

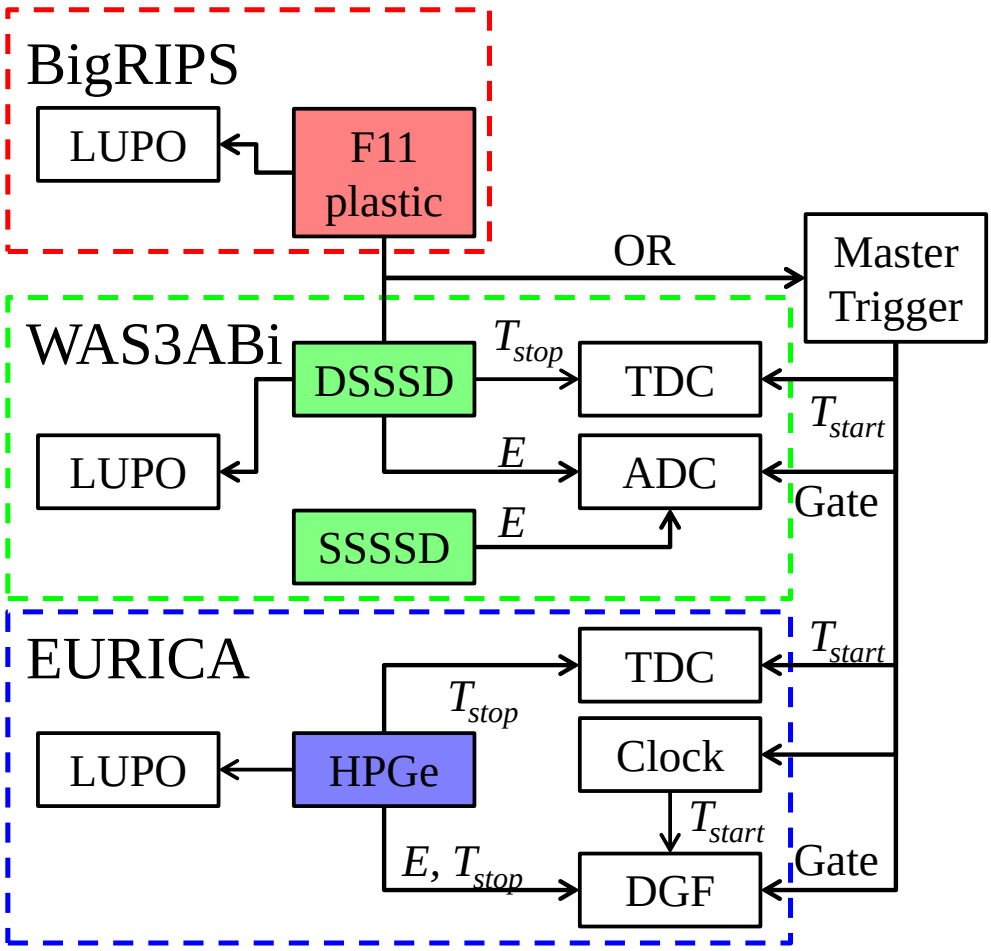

Figure 2.5: Simplified block diagram of the DAQ systems for BigRIPS, WAS3ABi, and EURICA. A color scheme separates the detectors from other electronics. For simplicity, the DAQ electronics for other detectors of BigRIPS are not shown here. Each stream's event timestamp was recorded by its own Logic Unit for Programmable Operation (LUPO), to be used in offline data merging. Logic conditions and physical quantities are labeled around the arrows. The clock to start the DGF time measurement in EURICA operated at 40 MHz for a 25-ns time step. Other electronics, such as delay modules, shaping amplifiers and discriminators are omitted in this diagram. For more detailed block diagrams, the reader is referred to Figs. 2.10 and 2.14 of Ref. [7].

In order to merge data from the three streams, each system recorded timestamps generated by its Logic Unit for Programmable Operation (LUPO) [89]. A sufficient time precision in steps of 10 ns was achieved from the 100-MHz clocks inside the LUPOs. Barring clock resets, the timestamps generated by a physics event would have a constant difference between the streams. The results of data merging from the different detector streams are presented in Section 3.1.

2.3 Summary of the experiment

An overview of the experiment status in terms of the primary beam rate and data collection rates is presented below.

2.3.1 Primary beam intensity

The average beam current for ^{124}Xe was 29.6 particles nano-Ampere (pnA) during 203.2 hours of beam time, equivalent to 1.85×10^{11} particles per second. The peak intensity of 38 pnA, a record for ^{124}Xe beam, was achieved in the later part of the experiment. The average intensity exceeded the listed value of 20 pnA by approximately 50%. Approximately at 25% through the total beam time, the SRC stopped operating due to cooling issues. After about 18 hours, the ^{124}Xe beam was restored with an increased intensity.

2.3.2 Data collection rates

During the experiment, the slit settings through BigRIPS and the ZeroDegree spectrometer were adjusted to control the DAQ rate and the distribution of different isotopes for investigation. An intense cocktail beam of radioactive nuclei resulted in a high implantation rate, which increased the rate of random background decay correlations. The rate of implantation and decay data as a function of beam time during the experiment is shown in Fig. 2.6. During the first 75 hours, efforts were made to maximize the ^{100}Sn transmission rate. During the later stages of the experiment, transmission of other nuclei (search for new and rare $N < Z$ isotopes and $N = Z$ nuclei, for instance) were prioritized over the most abundantly produced $N = 50$ isotopes. From Fig. 2.6, one could estimate the average implantation and decay rate per hour for different periods. The peak rates for implantation and decay data were 53 Hz and 97 Hz around $T_{beam} \sim 20$ hours respectively, and approximately 10 Hz and 20 Hz for later times. Naturally, isotopes with longer half-lives had lower signal-to-background ratios in their decay correlations.

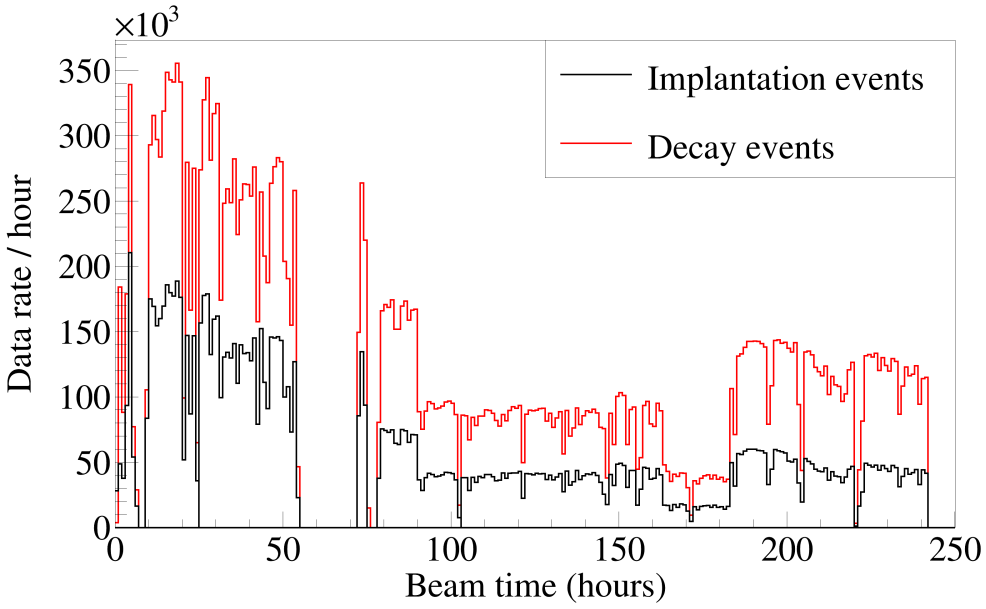

Figure 2.6: Data collection rates as a function of beam time over the course of the experiment. The stoppage of data acquisition starting at around 55 hours occurred during the SRC troubleshooting period. The fluctuation of the rates were caused by the variation in the primary beam rate, and different acceptance and transmission settings of BigRIPS and the ZeroDegree spectrometer.

Chapter 3

Data analysis

In this chapter, analysis methods of the experimental data are presented. Event reconstruction, detector characterization and calibration are followed by the methods to obtain experimental half-lives, decay branching ratios, new transitions, and Q_β values using Geant4 simulations.

3.1 Merging data from different detector systems

With three independent data acquisition systems but without a global triggering system, the data from each of BigRIPS, WAS3ABi, and EURICA detectors had to be merged in the offline analysis. This was carried out by matching event timestamps that were generated from a global 100-MHz clock signal (each clock tick was thus generated in 10-ns steps) that was recorded by each data stream's LUPO. As shown in Fig. 3.1, a proper merging of the data was achieved in a 100-200 ns window for all three systems. The time discrepancy between the systems was caused by the cables with different lengths, corresponding to unique signal delay times.

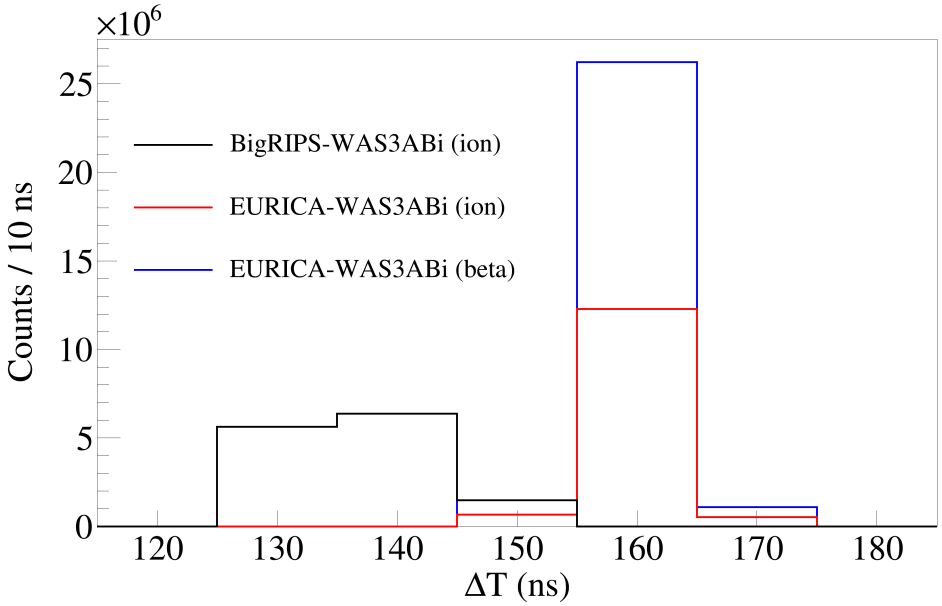

Figure 3.1: Event timestamp difference distribution for three pairs of detector/event type combinations. The events shown in this histogram could be properly merged.

3.2 Detector calibrations

The following sections highlight the methods and results of offline calibrations for WAS3ABi and EURICA data.

3.2.1 EURICA - energy, time and efficiency calibration

The characterization and calibration of HPGe detectors of EURICA for energy, time, and efficiency are described in the following sections.

Energy calibration

Standard calibration sources such as ^{60}Co and ^{152}Eu were used to perform an energy calibration of the HPGe detectors. The energies of β-delayed γ rays from the sources, ranging from 121 keV to 1400 keV, were used as calibration points. For each of the 47 HPGe channels, a first-order polynomial fit was performed to convert the DGF channel values into energies. The linearity of the slope was verified at 4207 keV, which was the γ-ray energy emitted from the known (12^+) isomeric state in ^{98}Cd [90]. The centroids of energy peaks of known isomeric transitions from segmented data sets were used to check for possible drifts in the calibration parameters over the course of the experiment. The results showed gain drifts less than 1% and offset shifts less than 0.2 keV for all 47 channels. The valid energy range of EURICA for this experiment was $E_{min} = 35$ keV and $E_{max} = 6200$ keV.

Time calibration

The time calibration of EURICA involved energy-dependent walk corrections (including WAS3ABi trigger walk for β-delayed γ rays) and a TDC channel-to-ns conversion.

Walk and time zero correction Both the DGF and the TDC modules of EURICA exhibited a time walk as a function of γ-ray energy. This phenomenon was caused by the energy-dependent signal rise time in the electronics, combined with a leading-edge threshold trigger. As seen in Fig. 3.2 for a TDC channel, low-energy γ rays resulted in extra delays of their time signals. This was corrected by plotting the time versus energy distribution of the prompt γ rays and fitting the time profile in energy slices. Then the raw TDC channel values were subtracted by the fit function to set the zero times for the γ rays. The same method was applied to the DGF time data.

Analogous to EURICA, WAS3ABi exhibited time walk as a function of energy deposited in each strip. Since EURICA also triggered on β-decay events triggered in WAS3ABi , the walk effect in WAS3ABi was carried over to the EURICA timing data. This effect is shown in Fig. 3.3, where the γ-ray times are systematically shifted in relation to the maximum energy deposited in any DSSSD strip for a β event. A phenomenological function of the form $A + B\log(E^{Si}_{max}) + C\log^2(E^{Si}_{max})$ was applied to correct both the walk and the zero offset for γ-ray times in β decay events.

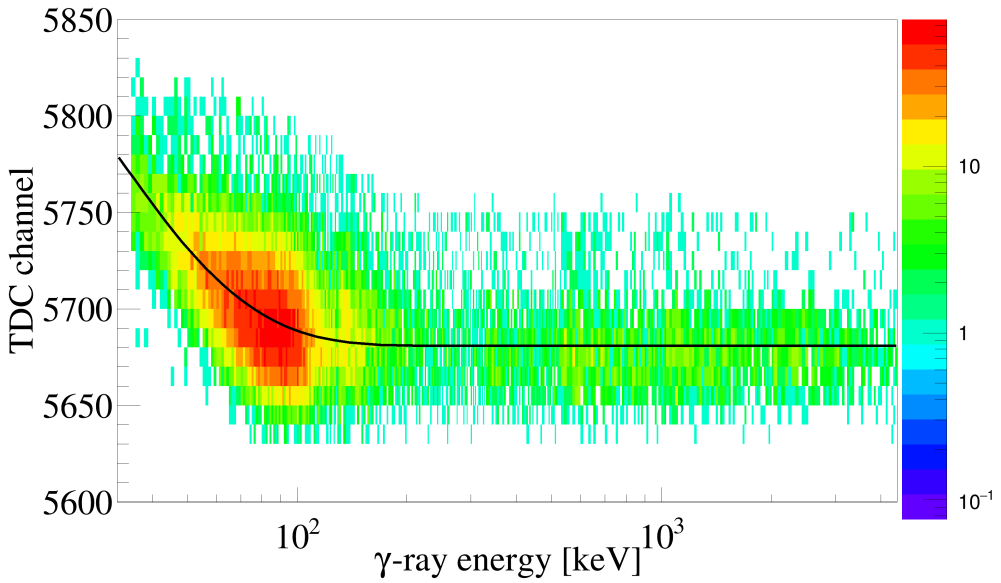

Figure 3.2: TDC distribution as a function of prompt γ-ray energies for one EURICA channel. A fit of the centroids of the energy slices is shown as a black line, the function of which was used to correct for γ-ray energy-dependent time walk.

Each individual DSSSD strip had its unique cable and trigger delays which affected the definition of the start time. Beta particles in general deposited energy in multiple strips without clear hints to the original position of the decay. Thus correcting for time zero on an event-by-event basis for β decays was impossible. However, the offsets could be estimated by examining γ-ray time distributions as a function of the strip number for single-strip β events. Fig. 3.4 shows systematic offsets up to 20 ns caused by several X-side strips in the middle DSSSD. Consequently, all half-life measurements of γ-decaying isomers populated by β decays were carried out with a delayed time gate.

TDC channel-to-ns calibration After walk correction was performed for both the TDC and the DGF modules, each crystal had its TDC channel plotted against the DGF time of the γ rays emitted from isomeric transitions in ^{96}Ag, which was produced abundantly with the half-life of the isomer being 1.56(3) μs [65]. This half-life was long enough to generate enough statistics up to the full range of 12 μs. First-order polynomial fits were applied in the range -500 to 11500 ns, and the resulting slopes were approximately 0.78 ns/ch for all channels.

EURICA's time resolution For half-life measurements of γ-decaying isomers, including those with limited statistics for maximum likelihood (MLH) analysis, a detailed characterization of EURICA's timing modules was necessary. As already mentioned, the TDC modules provided a better timing resolution than the DGF modules at the cost of efficiency at low energies (see Fig. 3.7). In

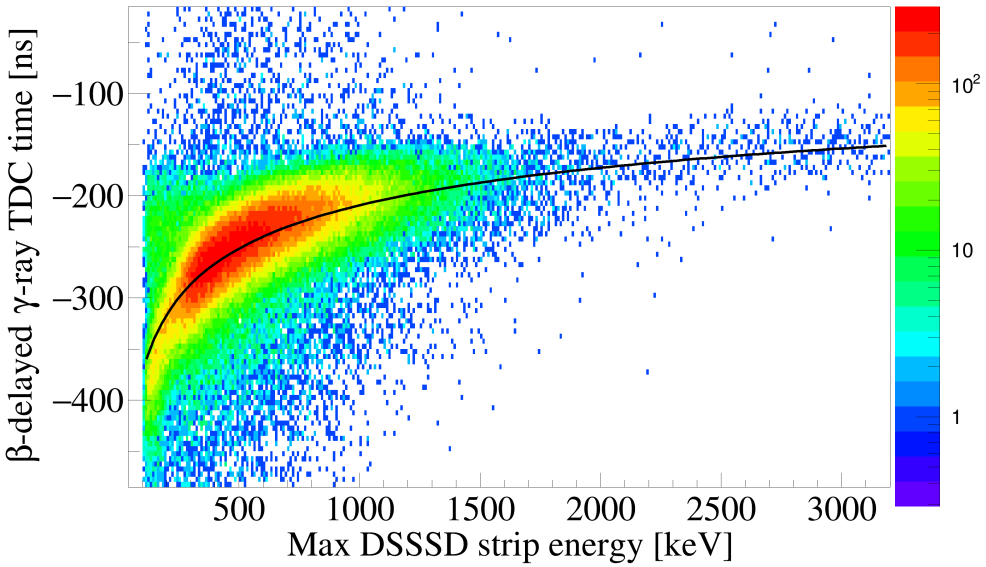

Figure 3.3: γ-ray TDC time as a function of maximum DSSSD energy in β events. If the event's maximum energy deposit in a DSSSD was low, the start trigger time in WAS3ABi became delayed; hence the difference between the WAS3ABi time and the γ-ray time was reduced. A fit function (black line) was used to correct the time walk for β-delayed γ rays.

the half-life analysis, the tradeoff between the statistics and the time resolution was considered for individual γ-decaying isomers. In addition, β-delayed γ rays had a greater time jitter than those from ion implantation due to the additional jitter in WAS3ABi trigger time, as well as systematic time zero shifts among the different strips. These are shown in Fig. 3.5. The zero offset correction was more accurate for the TDC than the DGF modules. For the DGF time data, the walk correction residuals were correlated with the γ-ray energy due to the limitations of the correction function.

Efficiency calibration

Knowing the energy-dependent γ-ray detection efficiency is crucial for decay spectroscopy experiments, for experimental quantities such as branching ratios and isomeric ratios depend on the intensities of the transitions. These are necessary for calculating electromagnetic transition strengths, and β-decay branching ratios, which provide important insight into the structure of excited states and transition matrix elements. First, a method to improve the γ-ray detection efficiency known as γ-ray addback is described below.

Addback γ-rays interact with matter in one of three ways: photoabsorption, Compton scattering, or pair production. In a photoabsorption event, all of the γ-ray energy is deposited at a single interaction point. On the other hand, a γ ray that undergoes Compton scattering will either be

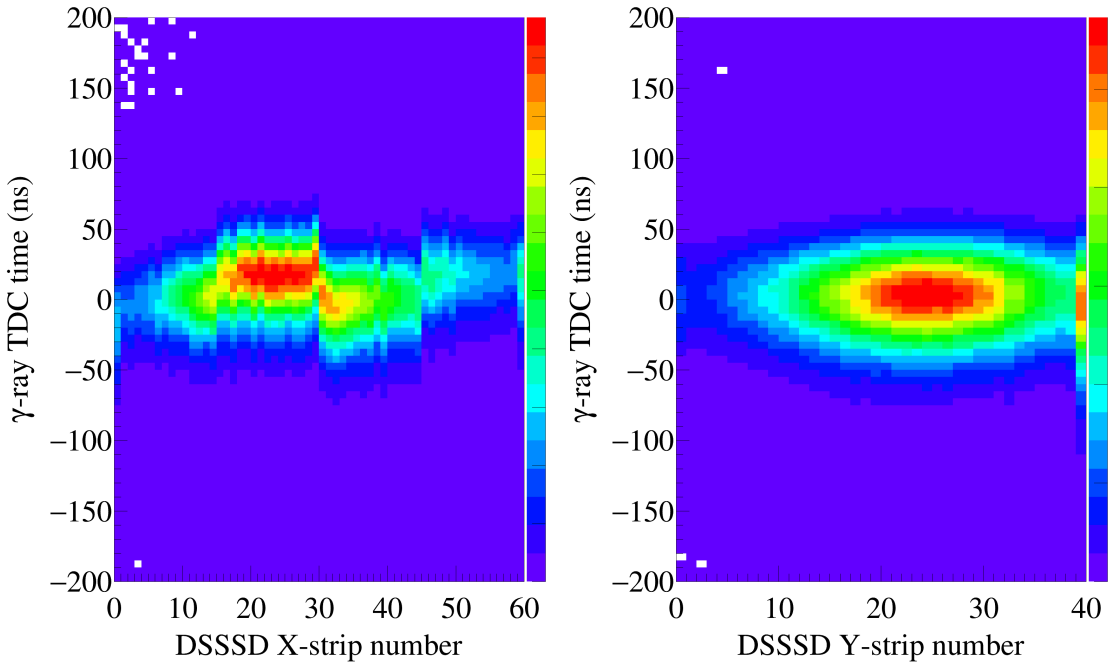

Figure 3.4: γ-ray TDC time distribution of β events with energy deposits in single DSSSD strips. Depending on the position of the β decay, systematic offsets of up to 20 ns are visible in the X-side strips. No such dependence is seen in the Y-side strips, except for a small shift at the last strip.

fully absorbed with multiple interaction points, or escape the detector material with a fraction of its original energy. Pair production is possible only for $E_\gamma > 2m_e = 1022$ keV, and the γ ray produces electron-positron pairs which share a part of the γ-ray energy. The positron will often deposit the full kinetic energy in the detector before annihilating with an electron, producing two 511-keV γ rays which undergo further photoabsorption or Compton scattering processes, unless they escape.

The addback scheme attempts to reconstruct the full γ-ray energy that may have been fragmented due to inter-crystal Compton scattering or pair production. In a given cluster, the energies in adjacent crystals were added back if the time difference between the γ rays was less than 100 ns in DGF time. The energy-dependent walk correction described in Section 3.2.1 was applied before applying the γ-ray addback scheme. It is possible that energies of multiple distinct γ rays that decay in a cascade be added back to a spurious summed energy; then the intensity of the energy peak under suspicion must compared against the non-addback spectrum.

Efficiency data and fit While standard techniques of efficiency calibration using well-known radiation sources ^{60}Co and ^{152}Eu exist, the radiation geometry from such sources was quite different than the experimental radiation geometry governed by ion implantation distributions. Thus the absolute efficiency of EURICA as a function of γ-ray energy was determined from the $\gamma\gamma$ coincidences of known isomeric transitions from ^{94,96}Pd, ^{96}Ag, and ^{98}Cd obtained in the experiment data.

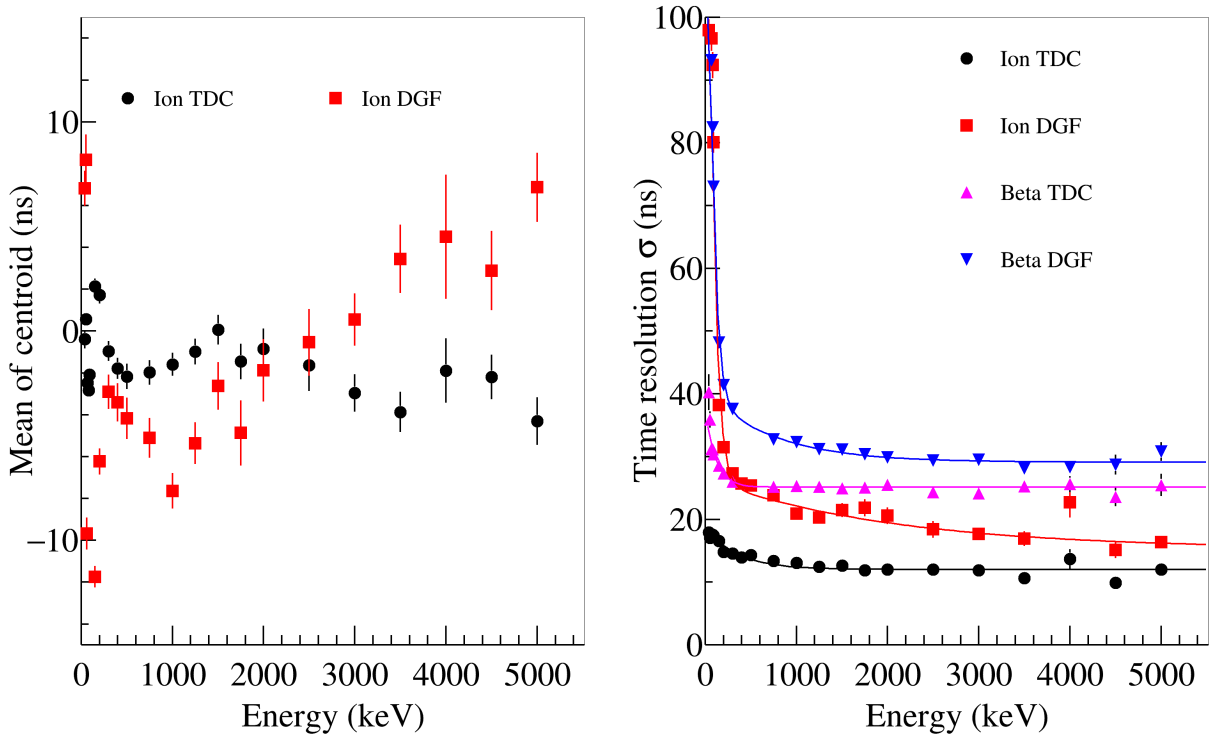

Figure 3.5: Left: mean centroid positions of prompt γ ray times as a function of energy following ion implantation events, after time walk correction. For β-delayed γ rays, the centroids of the prompt γ rays are poorly defined due to the strip-dependent time offsets, and are not reported here. Right: time resolution as a function of γ-ray energy in EURICA for the 4 types of events.

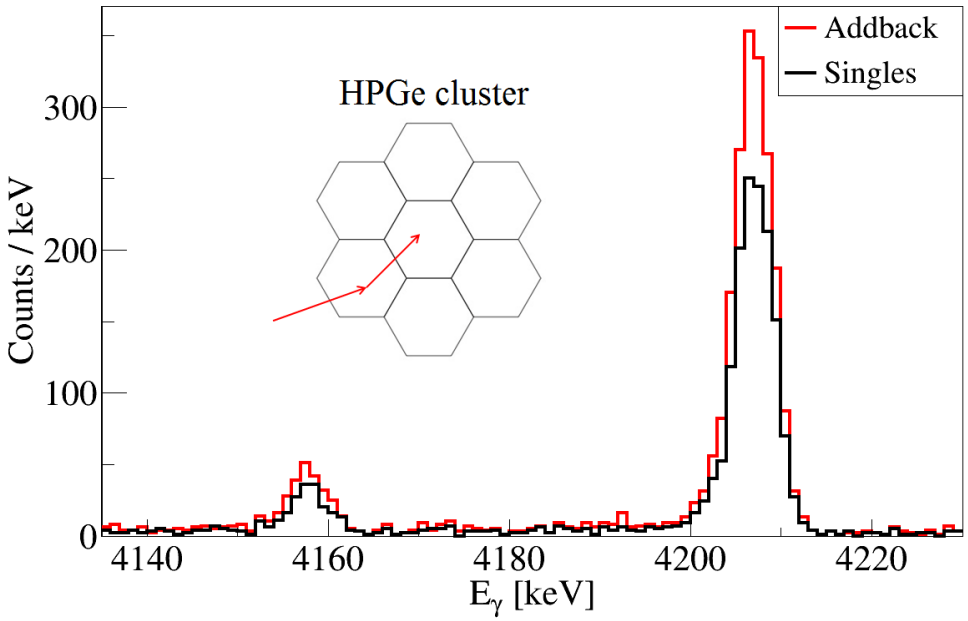

Figure 3.6: Black histogram: γ-ray spectrum of high-energy isomeric transitions in ^{98}Cd without addback. Red histogram: the same spectrum produced with addback. An improvement in counts at 4156 and 4207 keV is evident with the addback method that recovers the full energy of Compton-scattered γ rays, an example event of which is shown in the inset.

Given two γ rays γ_1 and γ_2 that depopulate an excited state in a cascade, the absolute efficiency ϵ_1 at the energy of γ_1 can be determined as:

$$\epsilon_1 = \frac{n_{12}}{n_2}\left(\frac{1+\alpha_1}{I_1}\right), \tag{3.1}$$

where n_{12} is the number of γ_1-γ_2 coincidence counts, and n_2 is the number of γ_2 singles counts. ICEs and branching into multiple states are taken into account by the IC coefficient α_1 and the relative intensity I_1. The subscripts 1 and 2 in Eq. (3.1) could be reversed to obtain ϵ_2.

The efficiencies at each γ-ray energy are plotted in Fig. 3.7 with different fit functions. Empirical fifth-order polynomials in $\ln(E_\gamma)$ were used:

$$\ln(\epsilon) = A + B\ln(E_\gamma) + C[\ln(E_\gamma)]^2 + D[\ln(E_\gamma)]^3 + E[\ln(E_\gamma)]^4 + F[\ln(E_\gamma)]^5, \tag{3.2}$$

and projecting back the fit constants A to F in linear scales generated the fit curves as shown in Fig. 3.7. Even though the efficiency for γ rays with high-resolution TDC timing information decreased significantly at low energies due to higher energy thresholds, the improvement in the time resolution had a higher merit in certain scenarios.

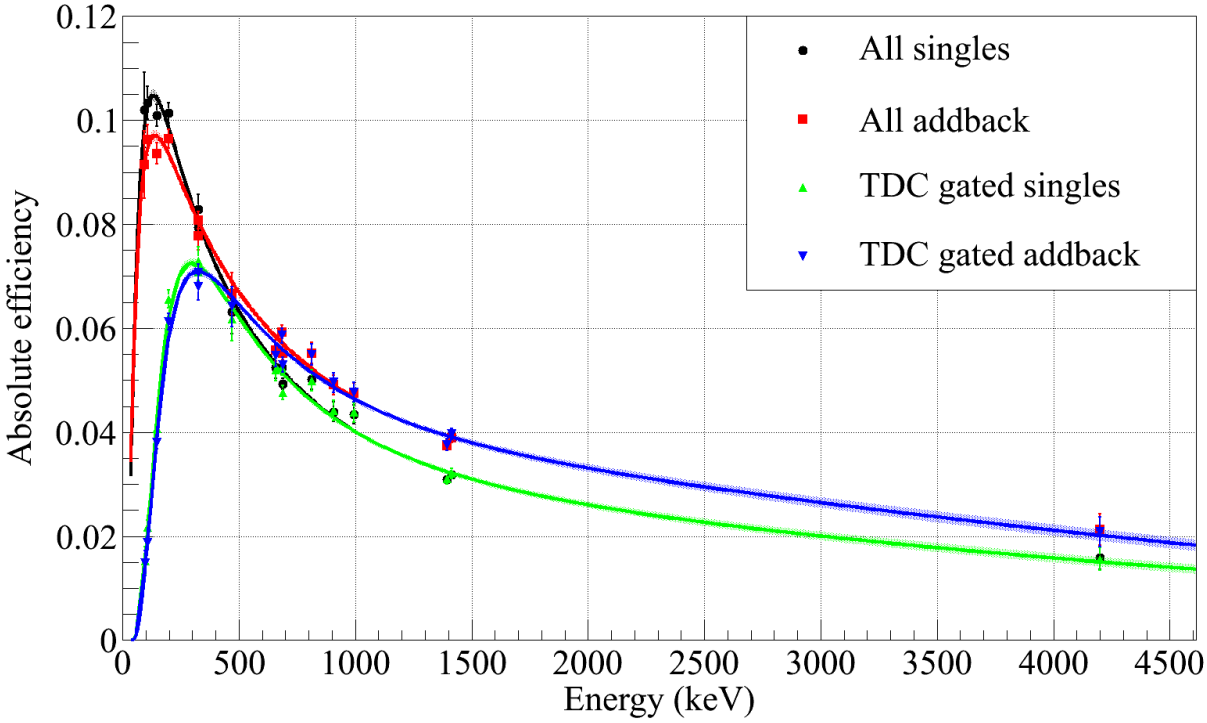

Figure 3.7: Absolute detection efficiency of EURICA as a function of γ-ray energy in four different modes. The addback scheme enhances efficiency at higher energies, but below 300 keV some loss in efficiency occurs due to false addback. High energy thresholds for the TDC modules, which provided better timing resolutions than the DGF modules, caused lower efficiencies at $E_\gamma < 500$ keV.

3.2.2 WAS3ABi - energy and time calibration

The sections below highlight the methods for the energy calibration in all DSSSD and SSSSD strips, as well as the TDC calibration for DSSSD X-side strips to be used for ion implantation events.

Energy calibration

The energy calibration of the DSSSDs and the SSSSDs of WAS3ABi was done using γ rays from a ^{60}Co source. For γ rays that Compton scattered once in the Si strips and deposited the rest of the energy in a HPGe detector of EURICA, the energy matrix E_γ(HPGe) vs E_γ(Si) (see Fig. 3.8) would show two diagonal bands that correspond to the total γ-ray energies: 1173 keV and 1332 keV. Calibration constants from first-degree polynomial fits would then be algebraically solved to convert the ADC channel values into physical energies.

After calibrating the energies, minimum energy thresholds were applied to reject the low-energy noise. E_{min} of 100 keV was required for the DSSSD strips with a few exceptions: strip 5 (120 keV) and 49 (150 keV) in DSSSD A, X-side. For the SSSSDs, the threshold was 200 keV for all strips; their larger widths required higher thresholds, compared to the DSSSD strips.

For the Y-side strips of the DSSSDs, high-energy calibrations in the 10-20 MeV range was required for accurate determination of ion implantation position. This was carried out by plotting an E-versus-E matrix for adjacent Y-side strips and fitting a line which bisected the distributions at the highest energies.

Time calibration

As mentioned in Section 2.2.1, only the DSSSD X-side strip channels recorded useful TDC information. Similar to EURICA, WAS3ABi time data was subject to an energy-dependent walk. However, the resolution of TDC time for WAS3ABi was too poor to merit proper walk correction. However, during ion implantation events, the time walk in WAS3ABi was negligible due to immense amounts of energy being deposited in each strip. The calibration of interest in this case was the time-zero offset for ion implantation events.

On the X-side of the DSSSDs, an incoming ion deposited energies beyond the ADC saturation thresholds (about 6000 keV) across multiple strips, rendering position determination via energy measurements imprecise. On the other hand, the TDC time difference between the F11 trigger and a strip on the X-side allowed the ion implantation position to be deduced unambiguously (see Fig. 3.10), using the fact that signals with higher amplitudes produce waveforms with faster leading edges. The time-zero calibration of the WAS3ABi TDCs involved fitting the minimum time distribution of each strip's TDC spectrum and centering the peak to zero.

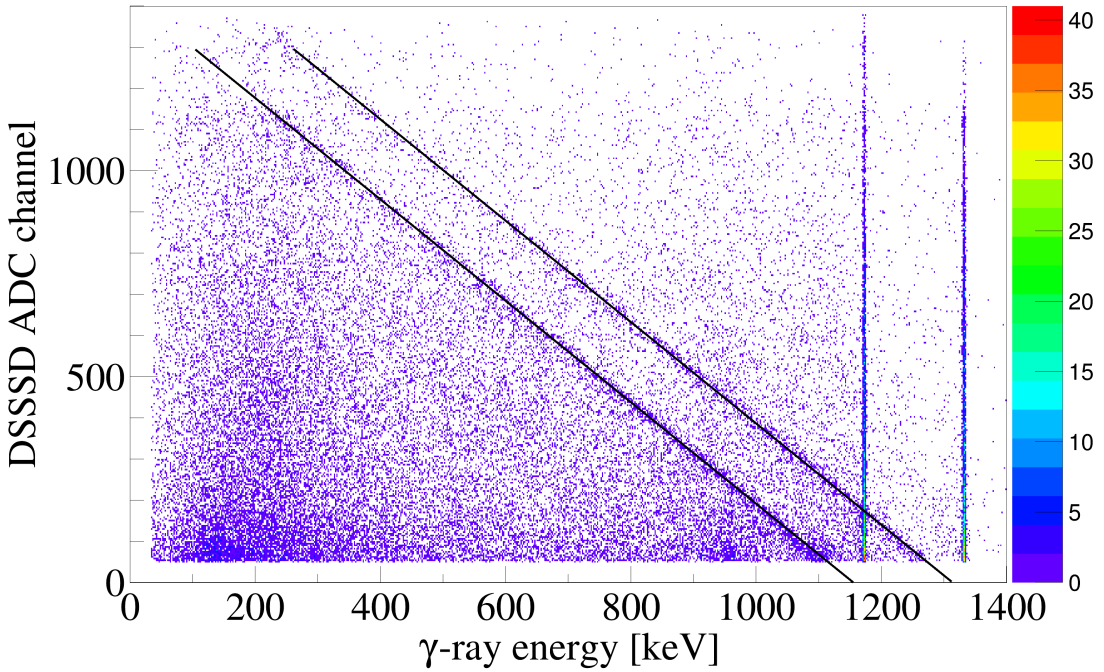

Figure 3.8: γ-ray energies detected in EURICA versus the ADC channel values of one of the DSSSD strips of WAS3ABi from a ^{60}Co source. Two diagonal bands are visible, whose energy sums should be 1173 and 1332 keV. Silicon strip energy calibration constants were obtained by fitting the energy profiles selected along the diagonal bands.

3.3 WAS3ABi event classification

WAS3ABi acts as both an implantation zone for heavy ions and a calorimeter for β particles and protons. These different types of events were separated by analyzing the energy hit pattern in both the DSSSDs and the SSSSDs. Low-mass charged particles constituting background events could also be rejected by applying separate rejection criteria.

3.3.1 Ion implantation

Ion implantation events were accompanied by data from both the BigRIPS and the WAS3ABi data streams. The sections below describe the analyses performed to determine the implanted ion's charge and mass, as well as its position in the DSSSD for decay correlation.

Isotope identification cut

Selection cuts of the PID data from BigRIPS were made by examining the profiles of Z and A/q distributions. For example, Fig. 3.9 shows the Z projection of a subset of the MUSIC data, cut on $A/q = 2$ events such that the identified isotopes were $N = Z$ nuclei. For each isotope, projection cuts were performed on both the A/q ratio and the Z-distribution profile to optimize the PID cut parameters. Contamination due to distribution overlaps from neighboring species was less than 1% for most isotopes. Gain and offset drifts in the PID data, due to slit setting changes, were observed. Hence the full dataset was divided into multiple subsets before applying the PID cuts.

Position determination

The implantation position was determined primarily on the basis of energy deposition in the DSSSD (see Fig. 3.10 as an example event). On the X-side, the saturation of the ADC modules meant imprecise position determination using the strip energies. Thus the strip with the minimum TDC time was designated as the implantation strip. On the Y-side, the ADC modules were not saturated by implantation events, and the strip with the highest energy deposit was chosen. The last DSSSD stack with $\Delta E > 10$ MeV in at least one of the Y-side strips was interpreted as the depth of the ion implantation.

One could then plot the implantation position distribution for each isotope. For instance, a comparison between the exotic ^{95}Cd ions and the abundantly produced ^{99}Cd ions, illustrating clear differences in the centroid positions in the XY plane and implantation depth, is shown in Fig. 3.11. As evident from the XY position distribution plots, there were losses due to the finite size of the DSSSDs. The percentage loss varied from 7 to 15% for more abundantly produced nuclei, depending on the isotope and the different separator settings which affected the rare isotope beam optics. For all isotopes, the majority of the ions was implanted in the middle DSSSD.

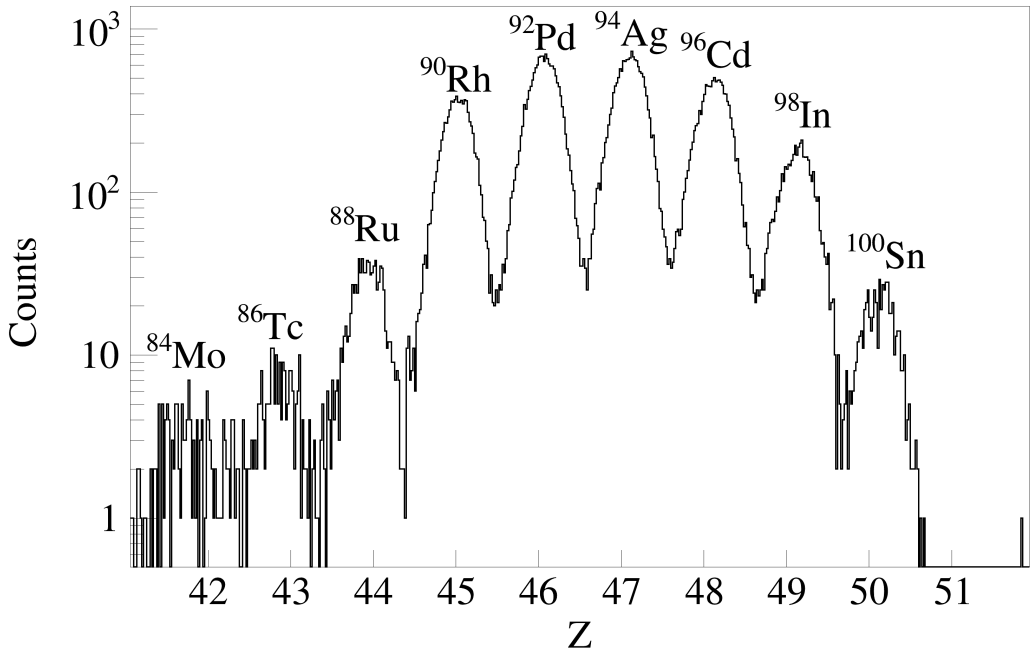

Figure 3.9: Projection of Z for $A/q = 2$ for a subset of BigRIPS data, leading to the identification of $N = Z$ nuclei.

3.3.2 β decay and proton emission

Excluding EC, proton-rich nuclei undergoing β decay and proton emission result in charged particles depositing energy in WAS3ABi. The sections below compare and describe the general characteristics of each type of decay, leading to a separation technique between the protons and positrons.

Characteristics of β events

It was shown from simulations that β particles in the energy range 100 keV to 10 MeV produce tracks with a wide range of scattering angles. The probability that a β particle travels in a straight trajectory without gaps in strips was rather low, and it could scatter back and forth between the stacks of both the DSSSD and the SSSSD. Initial attempts to build tracking algorithms were abandoned to remove the possibility of systematic underestimation of the full β energy.

Signature of proton emission

As noted in Section 1.3.3, proton emission is possible from decays of several of the nuclei presented in this thesis. In contrast to β particles, a proton usually deposits all of its kinetic energy in one Si pixel (one strip each in X and Y) due to its large mass and small $\beta = v/c$, leading to large $\langle dE/dx \rangle$ in Eq. (2.3). This property was used to distinguish protons from β particles (see Fig. 3.12). A minimum threshold of 1500 keV deposited in a pixel was the selection criterion for proton events.

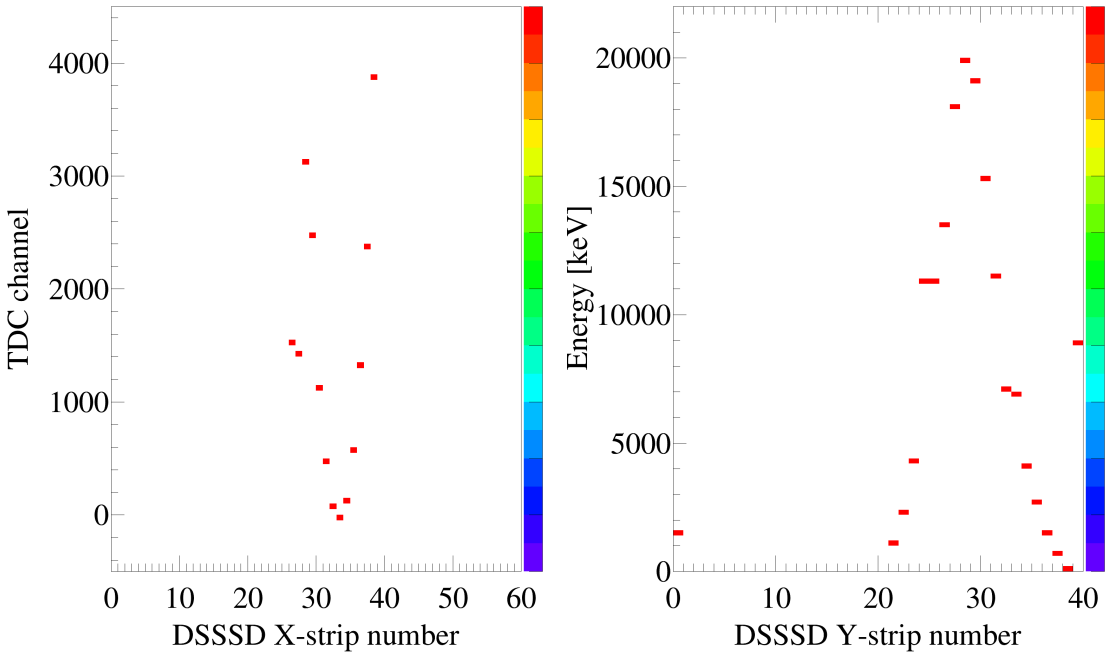

Figure 3.10: Left: TDC values for a DSSSD's X-side strips during an implantation event. The minimum value is found at strip 33. Right: energies of the Y-side strips of the same DSSSD. The strip with the maximum value is 28, leading to the implantation position coordinates (33, 28) for this event.

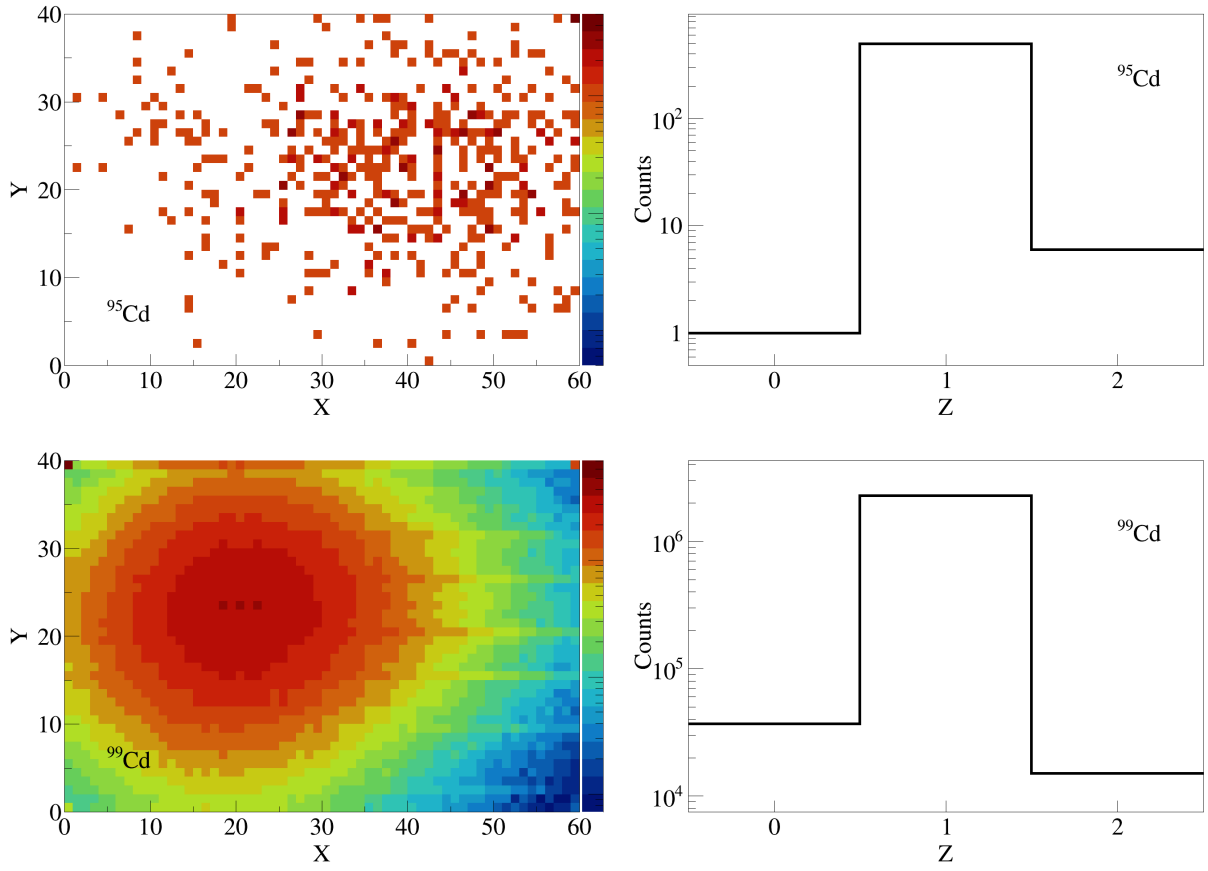

Figure 3.11: Implantation position and depth distributions of ^{95}Cd (top) and ^{99}Cd (bottom). Only the implantations into the middle DSSSD are shown. The differences in the distributions, caused by different A/q ratios and kinematics, are clearly visible.

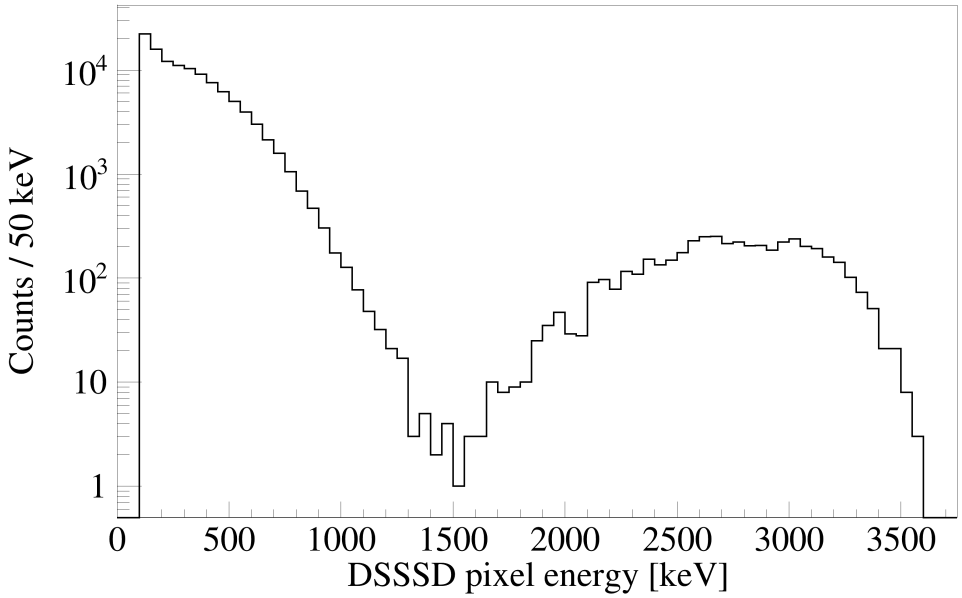

Figure 3.12: Single-pixel energy spectrum of decay events following ^{97}Cd implantation. Proton events could be classified with $E > 1500$ keV unambiguously from β particles, whose ΔE per strip was usually far less.

Fig. 3.14 shows the detection efficiency of simulated protons as a function of the input proton energy and the depth from the surface of the middle DSSSD. It is counterintuitive at first to see a valley in the detection efficiency profile as a function of the emission depth, but the explanation is the following: an escaping proton near the surface of the middle DSSSD deposits nearly all of its remaining energy in the neighboring DSSSD, such that the energy deposited in the surrounding DSSSD can surpass the 1500-keV threshold for the proton signature. However, if the proton is emitted from a deeper depth in the middle DSSSD and escapes to the neighboring DSSSD, then the proton's energy will be divided among the two DSSSDs so that neither of them may detect energy deposits exceeding the 1500-keV threshold. This effect vanishes for proton energies greater than 2800 keV. The protons emitted in this isotopic region have energies between 2 and 4 MeV, and the weighted detection efficiency in this energy range is 97% for ions being implanted near the surface (where $\Delta z < 0.05$ mm from the surface of the DSSSD). The rate of such events is a few orders of magnitude lower than the deep implantation events; thus the proton detection efficiency was assumed to be 100%.

3.3.3 Background rejection

Light particles (mostly deuterons with $A/q = 2$) were a major source of background events in WAS3ABi. Such particles were ejected from the hot fragments at the Be target, traveling all the way through BigRIPS and the ZeroDegree spectrometer before penetrating the silicon detector stacks. These events are characterized by a straight track through WAS3ABi with a fairly constant

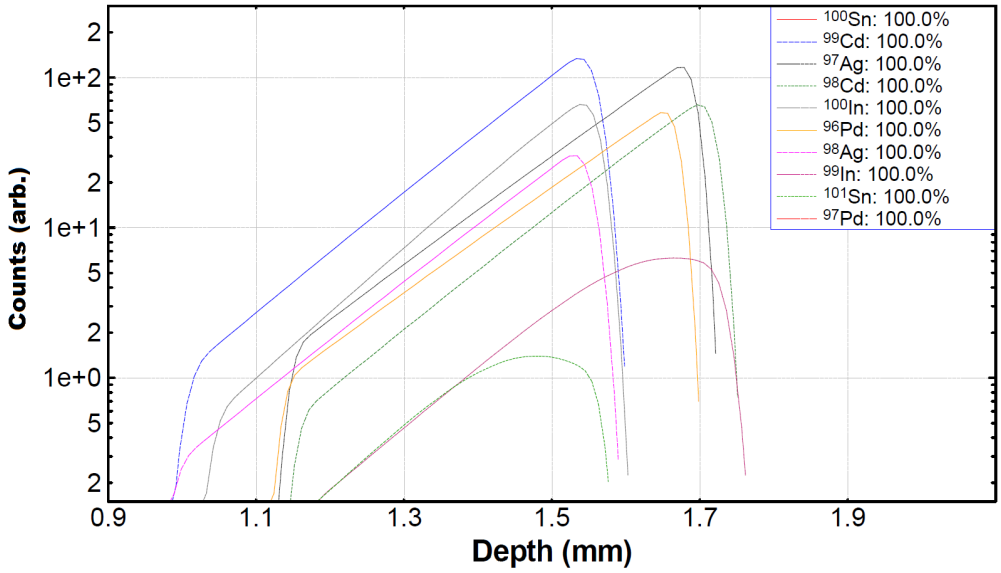

Figure 3.13: Implantation depth distributions of several abundantly produced isotopes from LISE++ calculations.

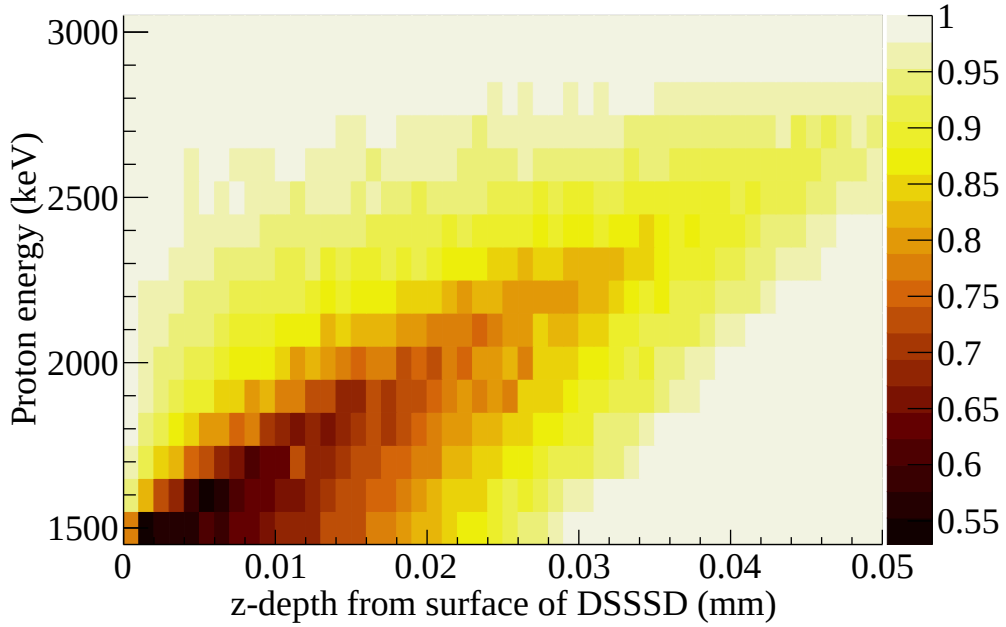

Figure 3.14: Proton detection efficiency as a function of proton energy and implantation depth from the surface of a DSSSD as simulated in Geant4.

energy deposit between 600 to 1400 keV per strip. These were rejected by cutting on the number of SSSSD stacks with energy deposits in the aforementioned energy range. Other background events, such as pileup implantation events, were removed from analysis using appropriate high-energy strip threshold cuts.

3.4 Implantation-decay correlation

Once an unstable isotope was implanted in a detector, it would undergo decays resulting in β and/or proton emission at the implantation position. Since the decay time is governed by the exponential decay probability density function (PDF), a decay event has to be correlated to an isotope in the offline analysis with position and time gates. The text below describes the implantation-decay correlation scheme.

3.4.1 Position correlation scheme

In spatial correlation, any β or proton event with an energy deposit above the minimum-energy threshold was correlated with the implanted isotope, if the decay event left energy signatures inside a cross-shaped window in the X- and Y-directions centered around the implantation pixel (a 3×3 zone without the corners). The Z-direction correlation was limited to the same DSSSD. The extensions in the XY directions was to accommodate certain events in which a β particle may have deposited an energy below 100 keV in the starting pixel. On the other hand, decays accompanied by proton emission yielded a unique position determination due to its high and complete energy deposit in a single pixel. Hence βp and proton events were correlated more cleanly.

3.4.2 Correlation time window

The correlation time window was adjusted according to the implanted isotope: from -5 s to 10 times the isotope's literature half-life, up to a maximum of 20 s. Correlations with negative times were events that had deposited energy around the implantation zone before the isotope of interest was implanted, and they were used to estimate the random background correlations. The upper limit on the time window was required to reduce computational time and remove from consideration decays of long-lived species which are better known from literature and overwhelmed by the background correlations. There was no limit to the number of decay correlations per isotope within the time window, for introducing a cutoff would introduce a bias for shorter half-lives. The significance of the bias would depend on both the random decay correlation rate and the actual half-life of the isotope.

3.5 Techniques for experimental observables

This section is devoted to the description of analysis strategies for processed experimental quantities, such as half-lives of isotopes/isomers and β-decay endpoint energies.

3.5.1 Half-life associated with particle emission

The nuclei of interest decaying via β^+/EC, βp or direct proton emissions had half-lives on the order of 10 ms to 10 s. The PDF describing this process is a simple exponential decay function:

$$f(\lambda_1, t) = \lambda e^{-\lambda t} = \frac{\ln 2}{T_{1/2}} \left(\frac{1}{2}\right)^{t/T_{1/2}} \tag{3.3}$$

However, the decay products in this experiment were unstable, and their subsequent decay contribution to the time spectrum must be taken into account. Fig. 1.2 captures many possible decay processes for an isotope of interest. Isomeric states are not included in the figure, which add more contributions to the initially simple PDF. Two methods were used to measure the half-lives of nuclei and their isomers.

Comprehensive fit without γ-ray gate

The first method is a fit with a comprehensive probability density function in the form of the Bateman equation [91], which includes many parameters of the descendant isotopes' decays. This method requires an accurate and precise parametrization on all of the half-lives and decay branching ratios (β^+, EC, βp, $1p, 2p$) of generations of nuclei following the parent decay. It is crucial to note that the correlation efficiency varies with each decay branch; EC events cannot be recorded with WAS3ABi, but decays accompanying proton emission can be assumed to be correlated 100% of the time. The β-decay correlation efficiency is lower than 100% due to a non-zero probability of positrons depositing energies below 100 keV in the pixels of the spatial correlation window, below the minimum energy threshold. The cutoff on the number of generations to be considered depends on the fit range, and the ratio between the parent isotope's expected half-life and the descendant nuclei's known half-life; the PDF of the descendant nuclei with significantly longer half-lives than the correlation time range and the half-life of the ancestors could be estimated as a constant background.

The β decay process populates the daughter nucleus, while at the same time the unstable daughter nucleus decays with a rate λ_2. If the parent decay has additional branches ($\beta p, 1p$, or $2p$), the daughter nuclei will be different with individual decay rates $\lambda_2^{\beta p}$, λ_2^{1p}, and λ_2^{2p}. Some instances of the parent nucleus may be populated in its isomeric state with its own half-life. The EC branch does not contribute to the β-decay time distribution, but must be included in the normalization condition. ICEs from an excited state of the daughter nucleus may offset the losses from EC processes.

With a finite time range to correlate implantation-decay events, the Bateman equation can be truncated to include only the components with $T_{1/2}$ less than or comparable to the time range. As the amplitude of the PDF is inversely proportional to $T_{1/2}$, contributions from isotopes and states with significantly longer half-lives become negligible. In this region of nuclei, the decay rate decreases by about an order of magnitude after each generation. Consequently, the granddaughter

decay component contributes to only 3% of the total β-decay counts, if the correlation time window is 10 times the parent nucleus' half-life.

The probability density function in the case of a pure β^+ decay has the form (constraining it to the daughter component)

$$f(\lambda_1, \lambda_2, t) = \frac{\lambda_1 \lambda_2}{\lambda_2 - \lambda_1}(e^{-\lambda_1 t} - e^{-\lambda_2 t}), \tag{3.4}$$

where λ_2 is the decay rate of the daughter nucleus.

Depending on the available statistics, the half-life was obtained either by χ^2 minimization on binned data, or the MLH analysis on unbinned data. The aim of the MLH method is to maximize the log likelihood function $\ln[L(\lambda)] = \ln[\prod_i^n f(t_i; \lambda)]$, where t_i is the set of decay times of n events and λ is the decay rate. In the simplest case of a pure parent decay, this corresponds to:

$$\left.\frac{\partial \ln[L(\lambda)]}{\partial \lambda}\right|_{\lambda=\lambda_{max}} = \frac{\partial}{\partial \lambda}\sum_i^n \ln(\lambda e^{-\lambda t_i}) = \sum_i^n \frac{1}{\lambda} - t_i = 0, \tag{3.5}$$

such that $\lambda_{max} = \sum_i^n t_i/n$: the average value of the decay times. The uncertainty on this decay rate (and consequently the $T_{1/2}$ value) is determined by locating $\lambda_<$ and $\lambda_>$ around the optimal λ_{max} such that the log likelihood value increases by $\epsilon/2$ from the minimum:

$$\ln[L(\lambda_<)] = \ln[L(\lambda_>)] = \ln[L(\lambda_{max})] + \epsilon/2, \tag{3.6}$$

where the confidence level $\epsilon = 1$ is taken to mean 1σ uncertainties given by $\lambda_<$ and $\lambda_>$. For a detailed description of the MLH method, the reader is referred to the thesis by C. B. Hinke [48] and citations therein.

Fit of γ-ray gated time spectrum

As a second method, half-life determination using γ-ray gates takes advantage of the fact that a β decay usually populates the daughter nucleus in an excited state, which then undergoes γ-ray emission. By fitting the β-decay time profile in coincidence with the known γ-ray transition energies, the half-life of the β-decaying state of interest can be obtained. In the case of low statistics, the γ-ray gated decay time distribution can be fitted by the normalized PDF f_{MLH}:

$$f_{MLH}(\lambda, t_{min} < t < t_{max}) = \frac{\lambda e^{-\lambda t} + C(t)}{\int_{t_{min}}^{t_{max}}(\lambda e^{-\lambda t} + C(t))dt}. \tag{3.7}$$

On the other hand, the decay time distribution with sufficient statistics can be fitted with a χ^2 method on binned data with an unnormalized PDF F_{χ^2}:

$$F_{\chi^2}(\lambda, t) = Ne^{-\lambda t} + C. \tag{3.8}$$

In both Eq. (3.7) and Eq. (3.8), the random background component is represented the parameter C (or $C(t)$ for MLH). One should take caution to not gate on a transition whose energy peak coincides with one of the descendants' γ-ray energy, or from an isomeric state from the same nucleus with a different $T_{1/2}$. For the MLH method, the inability to perform proper background subtraction with low statistics requires a parametrization of the random background time profile. This was done by gating on the side regions of the energy peak of interest and performing an empirical fit (usually an exponential with a constant background) - the fit function of which would then be included in the overall MLH fit. The argument for a constant background in the χ^2 fit is the following: in this data set, half-lives obtained with low-statistics γ-ray gates are usually short-lived compared to those of abundant species. So only much longer-lived species will contribute to the background, where a constant amplitude is a good approximation in a small time range for decay correlations. On the other hand, caution is advised even with the background-subtracted χ^2 method. Since the background subtraction is often not perfect, little variations in background γ-ray gates may have a large effect on the background-subtracted time spectrum - especially in the case of weak-intensity γ rays.

3.5.2 β endpoint energy determination

The β^+ decay of an atomic nucleus is a three-body process, which results in an emission of a positron and an electron neutrino that share the total kinetic energy. In terms of the Lorentz factor $\gamma = E_k/m_e c^2 + 1$ involving the positron's kinetic energy E_k and the rest mass of the positron $m_e = 511$ keV$/c^2$, the energy distribution function is:

$$f(\gamma, \gamma_{max}) \propto \gamma\sqrt{\gamma^2 - 1}(\gamma_{max} - \gamma)^2 F(Z', \gamma), \tag{3.9}$$

where $F(Z', \gamma)$ is the Fermi function. For non-relativistic β particles, an approximate form is used:

$$F(Z', \gamma) \approx \frac{2\pi\eta}{1 - e^{-2\pi\eta}}, \eta = \mp\frac{Z'\alpha}{\sqrt{1 - \gamma^{-2}}} \text{ for } \beta^{\pm}, \tag{3.10}$$

with the fine-structure constant $\alpha \approx 1/137$ and Z', the nuclear charge of the daughter nucleus. The endpoint energy Q_β is the energy difference between the initial and the final states, and is used to determine γ_{max}.

While this β decay energy distribution function is well known, the experimental energy spectrum is distorted by multiple factors: the minimum strip energy threshold cut, escape events (where the β particle trajectory goes out of either the DSSSD or the SSSSD), Bremsstrahlung radiation, and in-flight annihilation of a positron and an electron. Many of these processes systematically shift the β-decay energy distribution towards lower values. There is a possibility of a small positive shift in energy due to ICEs following β decay, which has a large conversion coefficient for low-energy γ-ray transitions. To take these effects into account in determining the endpoint energy, the simulation software Geant4 was used.

Geant4 simulation

Geant4 [92], a simulation toolkit developed initially for high-energy physics, is now a multipurpose software with various interaction models and robust geometry. A geometry to model positron interactions in the WAS3ABi setup had already been generated and checked for validity [93]. A display of a few positron events in WAS3ABi is shown in Fig. 3.15.

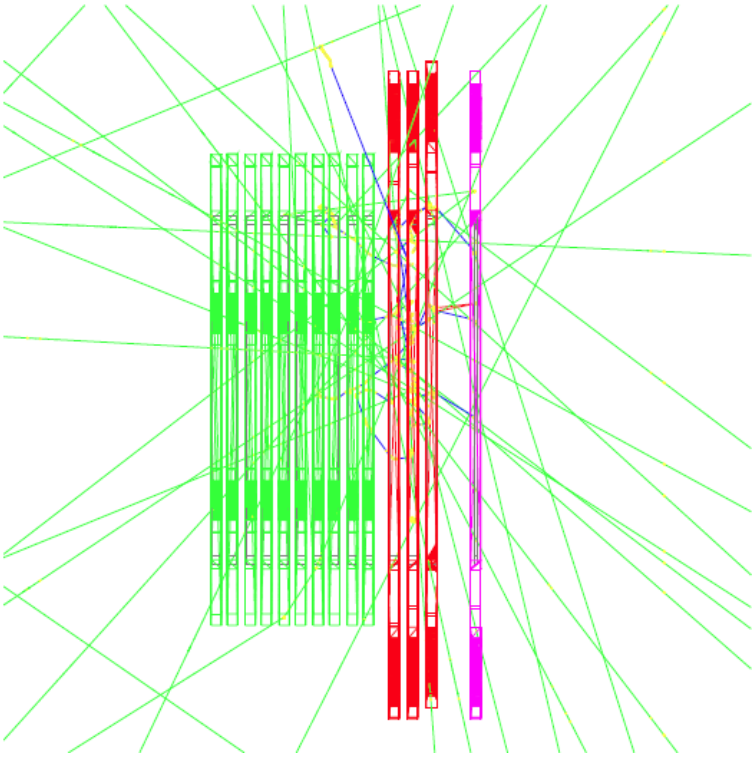

Figure 3.15: Geant4's simulated event display of a few positrons in WAS3ABi. The XY detector, the 3 DSSSDs, and the 10 SSSSDs are visible. Positron tracks are drawn in blue, and 511-keV annihilation γ rays are the green lines. Large scattering angles of positrons inside WAS3ABi and escape events enforced a Q_β analysis using simulations.

Aside from the details of the detector geometry, the main inputs to the simulation are: the distribution of βs' starting position in XY, as determined from the implantation position profile (see Fig. 3.11), and the β decay energy spectrum with a trial endpoint energy. The approach is to vary the trial endpoint energy and perform χ^2 comparisons between the simulation output and the experimental Q_β spectrum. For consistency, the output files from simulations were analyzed using the same conditions as with the experimental data. If the decay is suspected to populate multiple final states with comparable branching ratios and without a prospect of γ-ray gates to isolate a single feeding, then multiple energy distributions with multiple endpoints are added. In that case, additional contributions to the endpoint energy spectrum must be constrained in both the energy and the branching ratios from prior knowledge (whether from literature or γ-ray gates). Fig. 3.16 is an example of the Q_β determination of ^{98}Cd's dominant decay to the 1691-keV level in ^{98}Ag.

This Q_β value was corrected for internal conversion electron (ICE) energies originating from 61-keV $M1$ and 107-keV $E2$ transitions, the IC probabilities being 63% and 53% respectively. The sum of the expected energy contributions to the Q_β spectrum was 95 keV, which was subtracted from the raw Q_β value to yield Q_β(corrected) = 2735(30) keV. Then the Q_{EC} (ground-state to ground-state energy difference in a β decay) value, equal to the mass differences between the parent and the β-decay daughter nucleus, was calculated by the following formula:

$$Q_{EC} = \Delta M(\text{parent}) - \Delta M(\text{daughter}) = Q_\beta + 2m_e + E_x, \tag{3.11}$$

where $2m_e$ and E_x is the excitation energy in the daughter nucleus. Combining Q_β = 2.735(30) MeV, $2m_e$ = 1.022 MeV and E_x = 1.691 MeV, The final Q_{EC} value for ^{98}Cd was 5.448(30) MeV - consistent with the literature value of 5.430(58) MeV [2].

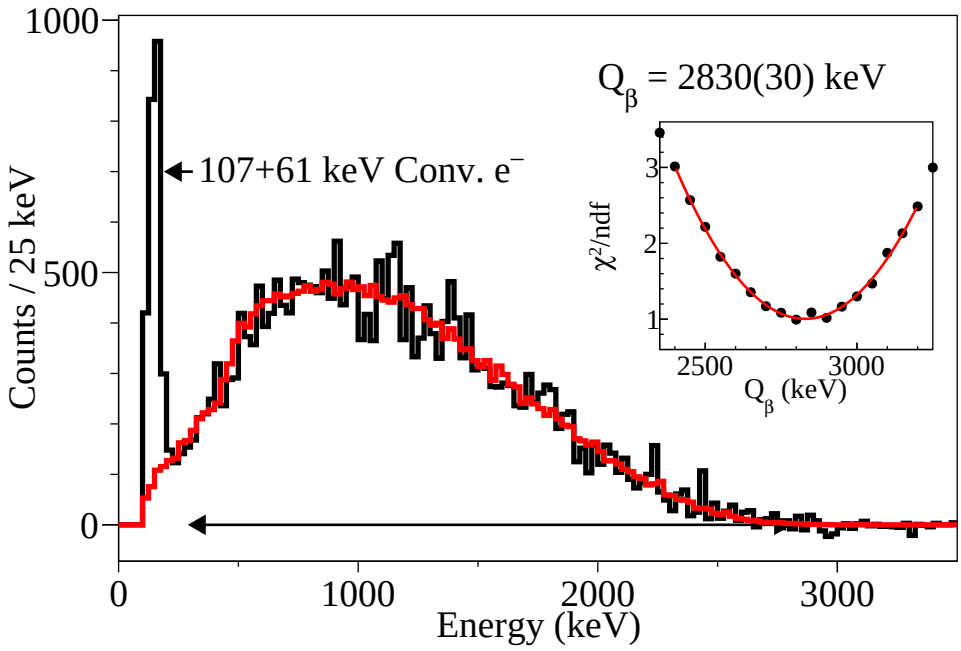

Figure 3.16: Q_β determination of ^{98}Cd's most dominant GT-decay branch to a (1^+) state in ^{98}Ag with Geant4 simulation. The experimental energy spectrum (black) extracted with a 1176-keV γ-ray gate was compared with simulated spectra (red) at various trial energies. The χ^2 evaluation range is given by the arrow at the baseline, avoiding the energy range containing ICEs emitted during EC. The inset shows the reduced χ^2 results with a minimum at 2830(30) keV.

3.5.3 Half-life associated with γ-ray emission

For γ-decaying isomeric states, the γ rays with isomer half-lives on the order of 10 ns to 1 μs were analyzed by both χ^2 and MLH fits, depending on the available statistics. In either case, the main component of the fit function was an exponential decay function convoluted by a Gaussian, to

account for the non-negligible time jitter of the γ-ray detector and its electronics. The mean of the Gaussian for the prompt time distribution was assumed to be zero after the time-walk correction. Then the PDF of the isomeric γ-ray decay time distribution is given by:

$$f(t;\sigma,\lambda) = \frac{\lambda}{2} e^{\lambda(\lambda\sigma^2-2t)/2} \mathrm{erfc}\left(\frac{\lambda\sigma^2 - t}{\sqrt{2}\sigma}\right), \tag{3.12}$$

where $\mathrm{erfc}(x)$ is the complementary error function defined as

$$\mathrm{erfc}(x) = 1 - \mathrm{erf}(x) = \frac{2}{\sqrt{\pi}} \int_x^\infty e^{-t^2} dt, \tag{3.13}$$

and σ is the energy-dependent time jitter shown in Fig. 3.5. This PDF is commonly used in fitting short half-lives of isomeric states from fast scintillator detectors such as cerium-doped $LaBr_3$ (see Fig. 5 in Ref. [94]). A large background of Bremsstrahlung radiation emitted during the ion implantation was avoided by fitting only the γ-ray times with $T_\gamma > 50$ ns. Many isomers were populated directly during fragmentation, whose $T_{1/2}$ could be obtained by simply fitting the gated γ-ray time spectrum after implantation. If the isomeric state of interest had a parent state that was also isomeric with $T_{1/2}$ comparable to the flight time through BigRIPS, the time difference spectrum between the feeding γ ray and the de-excitation γ ray was used in the analysis. This would require $\gamma\gamma$ coincidence data.

3.5.4 Isomeric ratios

An isomeric ratio R is the percentage of radioactive isotopes populated in a long-lived excited state. This work follows the definition of an isomeric ratio as noted in Ref. [95] as the percentage of an isomeric state populated promptly during fragmentation, relative to the flight time through the separator:

$$R = \frac{Y}{N_{imp} F G}, \tag{3.14}$$

where Y is the number of isomeric states deduced from WAS3ABi or EURICA data, N_{imp} is the number of implanted ions, F is the correction factor for isomeric decays during the flight time, and G is the correction factor for finite time correlation windows (β particles or γ rays). In the case of an isomeric state fed by a higher-energy isomer in the same nucleus, the feeding contribution from the parent isomer was subtracted from Y. While isomeric ratios are dependent on many external factors (beam energy, beam/target nuclei, target thickness) before considering the structure of the radioactive nuclei, knowing them enables a prediction about the statistics required to perform isomer decay spectroscopy in a neighboring region of nuclides.

For β- and βp-decaying isomers, the half-lives are significantly longer than the ~ 600 ns flight time in BigRIPS and the ZeroDegree spectrometer. In this case the isomeric ratio is calculated based on the number of decays observed divided by the number of implanted isotopes, combined with ion-β correlation efficiency, WAS3ABi deadtime, and the finite correlation time window corrections. For γ-decaying isomers, the half-lives are comparable to the flight time through the separator and

must be taken into account when calculating the ratios. In addition, IC is blocked for bare nuclei ($q = Z$); the half-life of the isomeric state during flight is increased by the hindrance factor F:

$$F = \frac{T'_{1/2}}{T_{1/2}} = \sum_i (1 + \alpha_i) b_i, \tag{3.15}$$

where the summation includes all decay branches with individual IC coefficients and branching ratios. This is an additional correction required to determine R.

3.5.5 Determination of deadtime loss

The deadtime loss corresponds to the percentage of unrecorded data due to multiple events occurring within a single data acquisition period. Given a Poisson process with a time-dependent event frequency λ (note Fig. 2.6), the loss was estimated as $\lambda\tau$, where τ is the WAS3ABi deadtime (600 μs). It was important to include the low-energy events ($E < 100$ keV for all DSSSD strips) in the deadtime calculation, which were removed from further analysis during the initial data sort. The deadtime loss correction was crucial for the βp branching ratio measurements, presented in Section 4.3.4.

Chapter 4

Results and discussion

The results obtained from the experiment are presented in this chapter. Where appropriate, supplementary details of the analysis methods for individual nuclei are provided. Given the variety of topics explored and the large number of nuclei investigated, the results were immediately followed by discussions based on comparisons to theoretical calculations.

4.1 Isotope production

Isotopes which were successfully identified by the BigRIPS-ZeroDegree spectrometer are presented in Fig. 4.1. Both Z and A/q shown in the figure are experimentally derived quantities, with slight deviations in the centroids for each of the isotopes from theoretical values due to the inhomogeneous magnetic field strengths of the dipole magnets and imperfect calibrations of the BigRIPS and ZeroDegree spectrometer data. Nevertheless, the validity of this PID plot was confirmed with γ-ray transitions from previously known isomers.

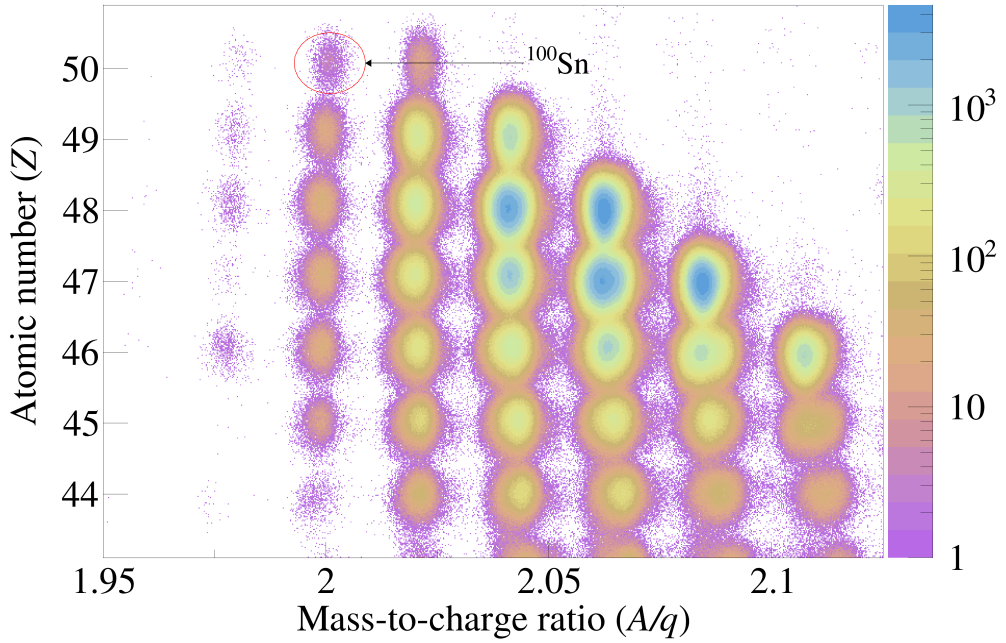

Figure 4.1: PID plot of the isotopes produced in this experiment. Events corresponding to ^{100}Sn are circled and labeled.

Multiple instances of $N = Z - 2$ isotopes were produced and identified for the first time: ^{90}Pd, ^{92}Ag, ^{94}Cd, and ^{96}In [96]. A tentative identification of ^{98}Sn and ^{86}Ru is elaborated in Ref. [75]. The low counts for these most neutron-deficient isotopes are primarily because of low production cross sections. Due to insufficient statistics, $N = Z - 2$ nuclei are not discussed further in this thesis. On the other hand, not all of the identified nuclei could undergo decay spectroscopy (i.e. ^{87}Ru) because they were deflected away from the WAS3ABi implantation zone at the last focal plane; the dispersion magnet settings were optimized for ^{100}Sn and were not suited to accommodate ^{87}Ru isotopes into the implantation area.

4.1.1 Limits of proton stability: ^{89}Rh, ^{93}Ag, and ^{97}In

A more careful examination of the $N = Z - 1$ nuclei statistics in Fig. 4.1 reveals a relative deficit of counts for ^{93}Ag and ^{89}Rh relative to the smooth trend expected for the production cross-sections. Half-life measurements, and proton separation energies were calculated based on a theory of proton emission [9] for these nuclei. A comprehensive analysis and discussion is provided in Ref. [96], which concludes that the proton dripline has been reached for $Z = 45$ and 47. Based on this analysis, the dripline does not appear to have been reached for $Z = 49$ as ^{97}In did not show any loss in the PID statistics. Intriguing new decay spectroscopy results for ^{97}In are discussed in Section 4.3.3.

4.2 Isomeric γ-ray/internal conversion electron spectroscopy

Element-preserving γ-ray and ICE transitions have been measured to determine their experimental electromagnetic transition strengths and isomeric ratios. A summary of the results is provided in Section 4.2.1. An overview of the isomeric ratios in comparison to theoretical predictions is given in Section 4.2.2. Highlights of isomeric γ-ray spectroscopy results are presented and discussed in the subsequent sections.

4.2.1 Half-life and isomeric ratio measurements

A summary of individual half-life fit results obtained in this analysis is given in Fig. 4.2 and Table 4.1. The details of the γ-ray gates for each nucleus are provided in Appendix A. For some isomers, independent half-life measurements were not performed due to insufficient statistics, or too long half-lives compared to the 12-μs EURICA time window. Isomeric ratios were calculated with the method described in Section 3.5.4. In comparison to the literature values, all of the measured half-lives were consistent within 2σ. Notable differences were found in ^{98}Ag's (3^+) and ^{98}Cd's (8^+) isomers, and the $T_{1/2}$ precision was significantly improved for ^{98}Cd's (12^+) isomer. New measurements involving several isomers are reported and discussed in the sections below.

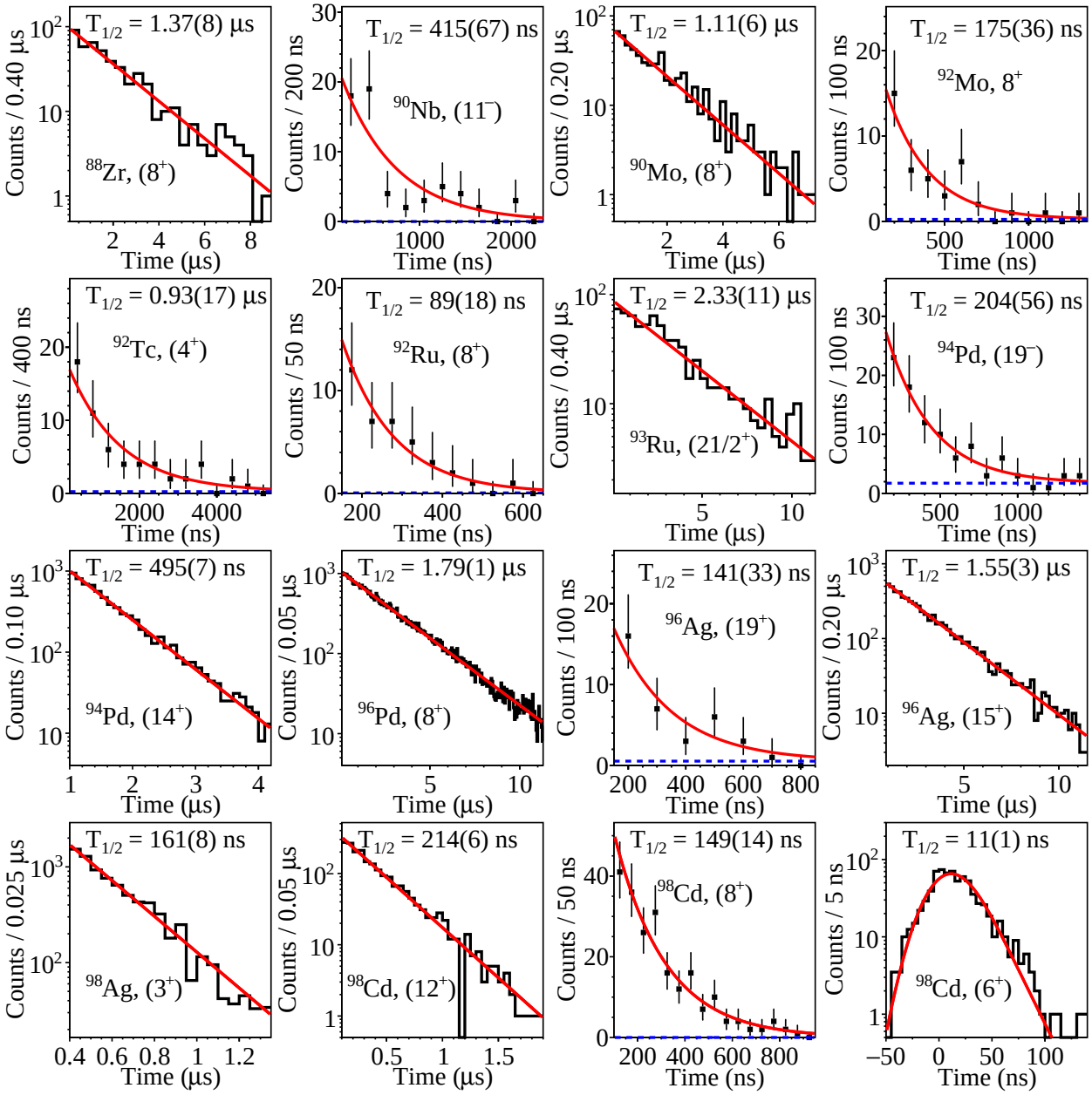

Figure 4.2: Time distribution of isomeric γ-ray transitions and half-life fits. Half-lives obtained with ICE-γ coincidences in ^{95}Ag and new γ-ray transitions in ^{96}Cd are presented in Fig. 4.4 and Fig. 4.7, respectively. For low-statistics data, unbinned MLH fits (data shown in linear scales with error bars) were performed to determine $T_{1/2}$. For sufficient statistics, χ^2 fits were made on binned histograms in logarithmic Y-axis scales. See Section 4.2.1 for the half-life analysis of the (6^+) isomer in ^{98}Cd.

Table 4.1: γ-decaying isomers with measured half-lives. Isomeric decay information (excitation energy E_x, isomeric state's spin and parity J^π, isomeric ratio R, transition multipolarity $\sigma\ell$, transition energy E_γ, total IC coefficient α, and branching ratio b) is given. Literature $T_{1/2}$ are shown for comparisons, where the values are taken from the NuBASE2012 evaluation of nuclear properties [2]. Only $\alpha > 0.01$ are tabulated.

Nucleus	E_x (keV)	J^π	R (%)	$\sigma\ell$	E_γ (keV)	α	b (%)	$T_{1/2}$ (μs)	
								This work	Literature
^{88}Zr	2888	(8^+)	69(5)	$E2$	77	2.87(4)		1.37(8)	1.320(25)
^{90}Nb	1880	(11^-)	11(3)	$E2$	71	3.97(6)	27(6)	0.415(67)	0.472(13)
				$M2$	1067		73(6)		
^{91}Nb	2034	$(17/2^-)$	47(12)	$E2$	50	13.9(2)			3.76(12)
^{90}Mo	2875	8^+	61(3)	$E2$	63	6.30(9)		1.11(6)	1.12(5)
^{92}Mo	2760	8^+	48(10)	$E2$	148	0.291(4)		0.175(36)	0.190(3)
^{92}Tc	270	(4^+)	10(1)	$E2$	56	9.8(1)		0.93(17)	1.03(7)
^{93}Tc	2185	$(17/2^-)$	54(5)	$E1$	0.31	8900			10.2(3)
				$E2$	40	33.9(6)			
				$M2/E3$	751				
^{92}Ru	2834	(8^+)	32(33)	$E2$	162	0.225(4)		0.089(18)	0.100(14)
^{93}Ru	2083	$(21/2^+)$	53(2)	$E2$	146	0.331(5)		2.33(11)	2.49(15)
^{94}Ru	2644	8^+	68(6)	$E2$	146	0.331(5)			71(4)
^{94}Pd	7209	(19^-)	7(3)	$E1$	106	0.129(2)	80(4)	0.204(56)	0.197(22)
				$E3$	1651		20(4)		
	4883	(14^+)	30(1)	$E2$	95	1.65(2)		0.495(7)	0.511(7)
^{96}Pd	2531	8^+	76(1)	$E2$	106	1.11(2)		1.79(1)	1.81(1)
^{95}Ag	4859	$(33/2^+)$	7.7(7)	$E3/M3$	875				39(3)
	2531	$(23/2^+)$	41(7)	$E3$	428	0.031(1)		2.1(2) ms	< 16 ms
	344	$(1/2^-)$	2.9(8)	$E3$	267	0.191(3)		90(18) ms	< 500 ms
^{96}Ag	6952	(19^+)	1.4(8)	$E2$	98	1.55(2)	81(9)	0.141(33)	0.16(3)
				$E4$	4265		19(9)		
	2647	(15^+)	18.7(4)	$E2$	44	27.9(4)		1.55(3)	1.54(3)
	2461	(13^-)	12.4(13)	$M2/E3$	486	$\simeq 0.02$	17(3)		100(10)
				$E3$	743		83(3)		
^{98}Ag	168	(3^+)	4.2(10)	$E2$	107	1.13(2)		0.161(8)	0.22(2)
^{96}Cd	(5605)	(13^-)	10(5)	$(E1)$				0.199(26)	
^{98}Cd	6635	(12^+)	10(1)	$E2$	50	18.9(3)	12(2)	0.214(6)	0.24(4)
				$E4$	4207		88(2)		
	2428	(8^+)	97(36)	$E2$	147	0.377(6)		0.149(14)	0.189(19)
	2281	(6^+)		$E2$	198	0.133(2)		0.011(1)	< 0.02

Discovery of 44-keV γ-ray transition in ^{96}Ag

The structure of ^{96}Ag was investigated up to the core-excited (19^+) isomer by Boutachkov et al. [65], who reported multiple γ-decaying isomeric states with a missing γ-ray energy emitted from the 2687-keV (15^+) isomer due to its low transition energy. As shown in Fig. 4.3, this γ-ray energy was determined to be 43.7(2) keV with a half-life of 1.48(27) μs, consistent with the literature value of 1.54(3) μs. Coincidence with the subsequent 667-keV γ ray was also confirmed, and $\alpha = 33(6)$ was deduced from the transition intensity analysis; this value agrees with the BrIcc [97] calculation of $\alpha(E2) = 27.9(4)$. An updated level scheme of ^{96}Ag with this E_γ is shown in Fig. 4.24.

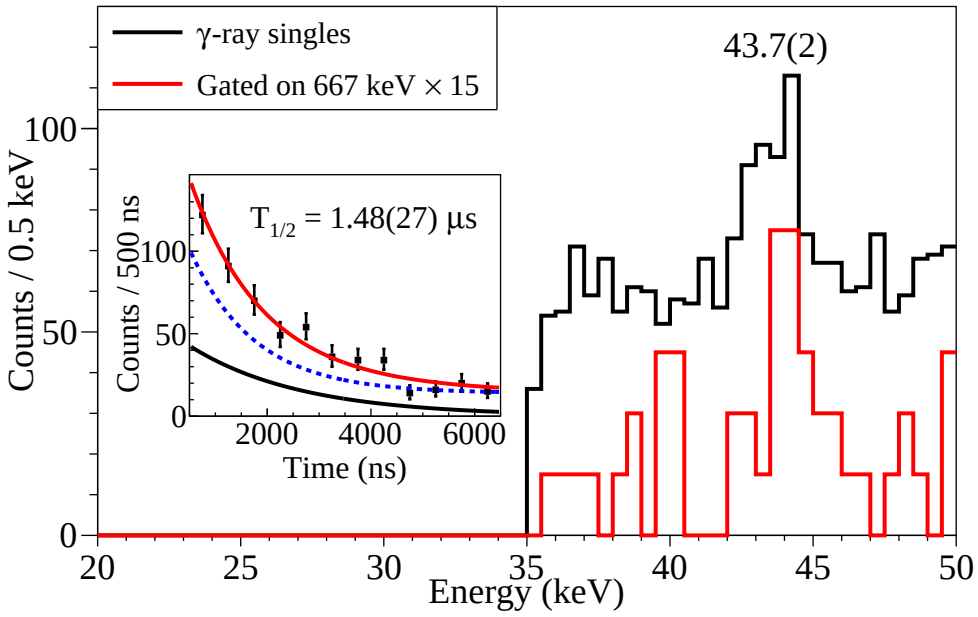

Figure 4.3: γ-ray energy spectrum following ^{96}Ag implantation. The black histogram corresponds to the time-delayed γ rays, and the red histogram is a scaled $\gamma\gamma$-coincidence spectrum gated on the 667-keV transition. The peak at 43.7(2) keV corresponds to the $(15^+) \rightarrow (13^+)$ $E2$ isomeric transition, where the inset shows the γ-ray time distribution of the low-energy peak with a consistent half-life for the (15^+) state.

Combining this new energy measurement with the $T_{1/2}$ of the isomeric state resulted in $B(E2) = 3.0(1)$ W.u. This value is in excellent agreement with $B(E2) = 3.0$ calculated in the pg model space while employing effective polarization charges of $e_p = 1.5e$ and $e_n = 0.5e$ to account for non-zero polarization of the core. The wavefunction of this isomer is a stretched $\pi g_{9/2}^{-3} \nu g_{9/2}^{-1}$ configuration as discussed in Ref. [65], the purity of which is supported by the agreement with the SM calculations with valence space limited to the $g_{9/2}$ orbital.

Half-life measurement of ^{98}Cd's (6^+) state

The 2281-keV (6^+) state in ^{98}Cd is a part of the $\pi g_{9/2}^{-2}$ seniority scheme. Its half-life, previously constrained as < 20 ns [90], was measured by fitting the γ-ray coincidence start-stop time difference spectra obtained from the 147-688 keV pair and the 147-1395 keV pair (see Fig. 4.28 for the level scheme). The 147-198 keV $\gamma\gamma$ coincidence pair was not included in the analysis due to a high Bremsstrahlung radiation background. The result is shown on the bottom right plot of Fig. 4.2, where the fit function reflects a time jitter of EURICA comparable to the measured half-life of 11(1) ns. This measured half-life corresponds to $B[E2; (6^+) \rightarrow (4^+)] = 5.5(5)$ W.u. This value is slightly greater than $B(E2) = 3.63$ W.u. calculated in the *pg* model space, and a much better agreement is found with the value of 5.14 obtained in the *gds* model space [90] (see Section 1.1.2 for details on the model space). Both calculations used polarization charges of $+0.5e$.

Half-lives of long-lived isomeric states in ^{95}Ag via ICE-γ spectroscopy

Three γ-decaying spin-gap isomers in ^{95}Ag have been reported with upper limits on half-lives up to 500 ms [98]. Given the fixed 12-μs time window for γ-ray spectroscopy data, these isomeric transitions were not observable with isomeric γ-ray data. However, internal conversion electrons from the two lower-energy states were detected with WAS3ABi. The detection of subsequent γ-ray transitions enabled half-life analyses of the isomers as if they were β-decaying states. The results are shown in Fig. 4.4. The half-lives of the isomers were 90(18) and 2.1(2) ms for the $(1/2^-)$ state and the $(23/2^+)$ state, respectively (see the insets of Fig. 4.4). The corresponding transition strengths based on the suggested multipolarities are $B[E3; (1/2^-) \rightarrow (7/2^+)] = 0.22(4)$ W.u. and $B[E3; (23/2^+) \rightarrow (17/2^-)] = 0.37(3)$ W.u. These $E3$ transitions compare well to $B(E3; 19^- \rightarrow 16+) = 0.28(3)$ W.u. in ^{94}Pd and $B(E3; 13^- \rightarrow 10+) = 0.18(2)$ W.u. in ^{96}Ag. The isomeric ratios for the states were calculated using the absolute γ-ray intensities and corrected for WAS3ABi deadtime loss and internal conversion coefficients.

Moschner et al. [99] analyzed a separate dataset containing ^{95}Ag isomers and assigned a 39(3)-μs half-life to the highest-energy isomeric state. Based on this half-life, they also suggest a change in the spin of the isomer to $(33/2^+)$ as well as the multipolarity to $E3/M3$. This half-life would be too long for the EURICA time window and too short for WAS3ABi with its 600-μs deadtime. This value was adopted to calculate the $(33/2^+)$ state's isomeric ratio.

4.2.2 Isomeric ratios and the sharp cutoff model

The isomeric ratios for γ-decaying isomers were combined with those from β-decaying isomers tabulated in Table 4.3 to be compared with theoretical predictions, similar to several works [95, 100, 101] with fragmentation reactions performed at various primary beam energies and masses.

Theoretical predictions of isomeric ratios involves the distribution of final angular momenta J of the fragments. In addressing the statistical abrasion-ablation model [102] for fragmentation,

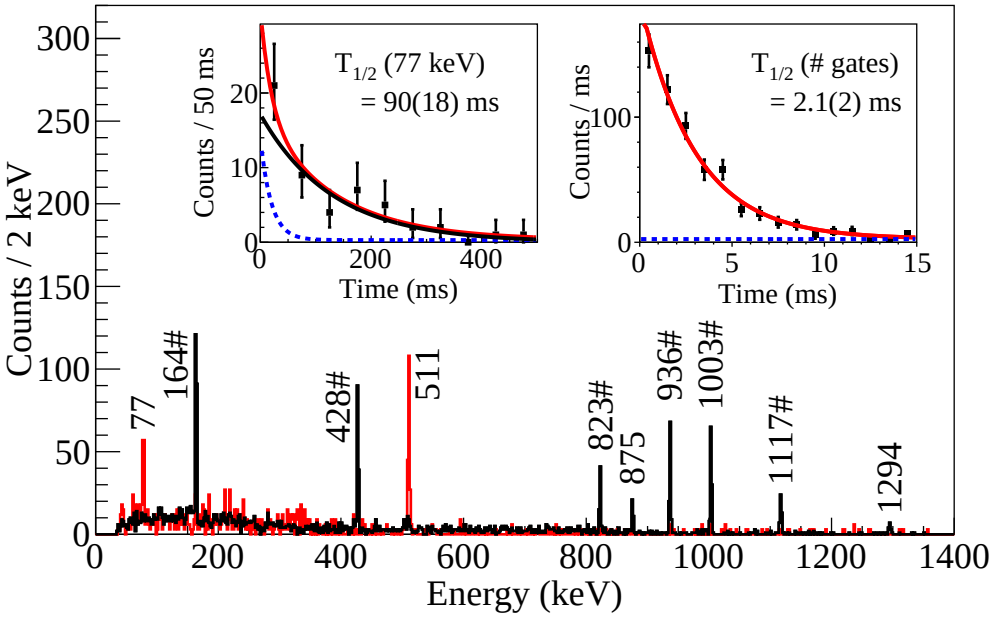

Figure 4.4: Black histogram: γ-ray energy spectrum with WAS3ABi total energy less than 500 keV and in a time window between 0 and 20 ms after ^{95}Ag implantation. Red histogram: γ-ray energy spectrum gated on 267-keV ICE energies in WAS3ABi with a time window up to 500 ms. The insets show the half-lives of the two isomeric states obtained with the different γ-ray gates. Transitions at 875 and 1294 keV are γ rays emitted from the higher-spin isomer which are randomly correlated with ICE events.

Ref. [103] gives a simple analytical formula for the probability density function:

$$P_J = \frac{2J+1}{2\sigma_f^2} e^{-J(J+1)/2\sigma_f^2}, \tag{4.1}$$

where σ_f is the spin-cutoff parameter of the final fragment:

$$\sigma_f^2 = \langle j_z^2 \rangle \frac{(A_p - A_f)(\nu A_p + A_f)}{(\nu+1)^2(A_p - 1)}. \tag{4.2}$$

The first quantity $\langle j_z^2 \rangle$ - the average square of the angular momentum projection of a nucleon in the fragment - is calculated based on the semi-classical treatment of angular momentum distribution in the Woods-Saxon potential:

$$\langle j_z^2 \rangle = 0.16 A_p^{2/3} (1 - \frac{2}{3}\beta), \tag{4.3}$$

where β is the quadrupole deformation parameter of the fragmented nucleus. Negligible deformation is expected for isotopes in the vicinity of a magic nucleus such as ^{100}Sn, so $\beta = 0$ was assumed. A_p and A_f are the mass numbers of the projectile ($A_p = 124$ for ^{124}Xe in this experiment) and the fragment nucleus. The parameter ν is the mean number of evaporated nucleons per abrasion of one nucleon, which was varied among different works. In Refs. [95, 101] involving 750-MeV/u ^{238}U and 1-GeV/u ^{208}Pb beams, $\nu = 2$ was assumed; in Ref. [100] with a 60-MeV/u ^{92}Mo beam, $\nu = 0.5$ was chosen to calculate R_{theo}. Since there is no quantitative determination of ν specific to the 345-MeV ^{124}Xe beam used in this experiment, it was left as a free parameter in this analysis.

After having established the required relationships and ingredient quantities to calculate the distribution of J, the sharp cutoff model was employed. For a given isomeric state with spin J_m, the sharp cutoff model assumes that $J > J_m$ states populated after the fragmentation reaction promptly undergo spin-decreasing γ-ray transitions until they are trapped at the isomer. Then the theoretical isomeric ratio R_{theo} is given by

$$R_{theo} = \int_{J_m}^{\infty} P_J dJ = e^{-J_m(J_m+1)/2\sigma_f^2}. \tag{4.4}$$

The ratios R_{exp}/R_{theo} are plotted as a function of J in Fig. 4.5 assuming $\nu = 0.5$, which shows a relatively spin-independent agreement between the theoretical and the experimental ratios for all the positive-parity isomers without $N = 50$ core excitation. The results were also independent of the decay mechanism (γ decay versus β decay), highlighting the consistency of the two very different methods described in Section 3.5.4 to determine experimental isomeric ratios. It was observed that for $\nu > 0.5$, R_{theo} was more severely underestimated with increasing spin; for $\nu < 0.5$, R_{exp}/R_{theo} approached unity for $J \leq 16$ but showed a systematic trend decreasing below 1 at higher spins. From Fig. 4.5 the limitations of the sharp cutoff model are exposed in three scenarios: negative-parity isomers, low-spin isomers with $\Delta J > 0$, and $N = 50$ core-excited isomers. All of these involve the details of the nuclear structure, and the explanations are provided below.

Negative-parity isomers are wavefunctions with nucleon excitation from the $p_{1/2}$ orbital; contri-

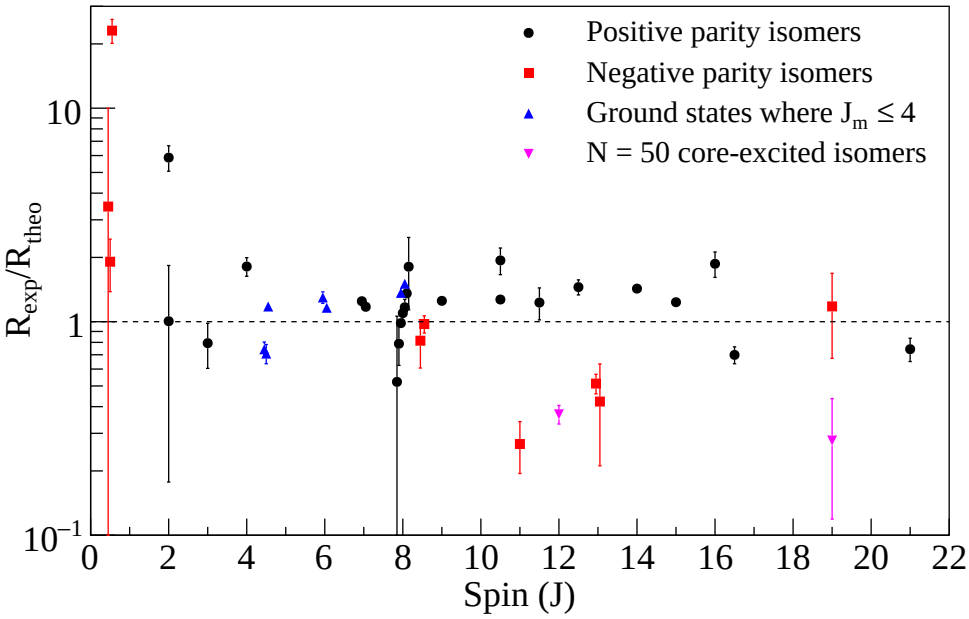

Figure 4.5: Comparison of experimental isomeric ratios to the sharp cutoff model calculations. Isomeric ratios of both γ-decaying and β-decaying states presented in Table 4.1 and Table 4.3 are presented.

butions from the lower-energy $f_{5/2}$ and $p_{3/2}$ orbitals may also be present, but are generally small. Due to the large occupation number available for the positive-parity $g_{9/2}$ orbital compared to the $p_{1/2}$, the level densities at a given J are significantly higher for positive-parity states. Combined with the fact that parity-changing transitions are hindered, γ-ray branching ratios from higher-spin J^+ states to isomeric J^- states must be limited. It is also crucial to note that both (13^-) isomers from ^{96}Ag and ^{96}Cd have higher-spin positive parity isomers ((19^+) and (15^+) in ^{96}Ag, and (16^+) in ^{96}Cd) which should introduce a spin cutoff in the integral of Eq. (4.4). In comparison, the experimental ratios for $(17/2^-)$ isomers in ^{91}Nb and ^{93}Tc are better reproduced by the model. For these nuclei, $N = 50$ and the shell closure implies that the low-energy excitation scheme is solely driven by protons in the $p_{1/2}$ and the $g_{9/2}$ orbitals. Without involving core excitations in the neutron orbitals, there are few positive-parity states with $J > 17/2$. The (19^-) isomer in ^{94}Pd is quite high in spin, where it is reasonable to expect little disparity between the number of possible nucleon configurations among positive and negative parity states; the only higher-spin, positive-parity state available in ^{94}Pd is (20^+), which can only be constructed by maximally stretching both the proton and the neutron spin projections within the $g_{9/2}$ orbital.

Isomers with spin-increasing transitions violate the premise of the sharp cutoff model that prompt transitions from higher-spin states will be funneled down to lower-spin isomers. This was previously observed based on the vastly different isomeric ratios of ^{90m}Mo and ^{92m}Tc populated from fragmentation of a 58-MeV/u ^{112}Sn primary beam [104]. A slight amendment to the model for these isomers was to forgo the integral given by Eq. (4.4) and use the discrete probability density

function of Eq. (4.1) to calculate their R_{theo}. The results of this modification on $J_m \leq 4$ isomers are reflected in Fig. 4.5, which still have large deviations from experimental results. Thus the population ratios of the ground states ($R_{g.s.} = 1 - \sum_i R_i$) were analyzed as if they were isomeric, and they were better reproduced by the model (blue triangles).

Core excitation is another structure-driven effect that the sharp cutoff model fails to address. The ratios for ^{98}Cd's (12^+) and ^{96}Ag's (19^+) core-excited isomers were overestimated by approximately a factor of 3. In these configurations, one neutron is excited across the $N = 50$ shell gap by 4-5 MeV, leaving a hole in the $g_{9/2}$ orbital (see Fig. 1.4(c)). This configuration requires an evaporation of a more deeply-bound $g_{9/2}$ neutron at the cost of the shell gap energy while preserving a neutron in one of the valence orbitals above $N = 50$, the rarity of which is reflected by the low R_{exp}/R_{theo}. This finding is relevant for the isomeric ratio estimation of the hypothetical (6^+) core-excited isomer in ^{100}Sn addressed in the next section.

Discussion of the hypothetical 6^+ isomer in ^{100}Sn

No delayed γ rays were found to be associated with ^{100}Sn implantation events, in reference to Section 1.3.1. Thus upper limits on the half-life of the hypothetical 6^+ isomeric state decaying by an $E2$ γ ray are proposed. The expression for the half-life upper limit is given by:

$$T_{1/2} < \frac{\ln(2) T_F}{H[\ln(\epsilon N_{ion} R) - \ln(N_\gamma H)]}, \tag{4.5}$$

where T_F is the flight time of ^{100}Sn ion through the separator, ϵ is EURICA's detection efficiency, N_{ion} is the number of implanted ^{100}Sn isotopes, R is the isomeric ratio, N_γ is the number of available γ-ray events for observation, and $H = 1 + \alpha$ is the hindrance factor for γ decays. The details of R, N_γ and H are summarized below.

From Fig. 4.5 and the sharp cutoff model, $R(^{100m}$Sn) can be estimated. Noting that the excited states of ^{100}Sn must involve core excitations, the weighted average of R_{exp}/R_{theo} from ^{98}Cd's (12^+) and ^{96}Ag's (19^+) core-excited isomers was used to calculate the hypothetical $R(6^+)$ of ^{100m}Sn. This value was 25%. In order to reflect the crudeness of the sharp cutoff model and to visualize the dependence of $T_{1/2}$ on R, two additional ratios of 12.5% and 50% were also assumed. From Poisson statistics, 4 events could result in zero observations at the 2σ confidence limit; thus N_γ was set to 4. The origin of H comes from the physics of internal conversion. The IC branch, significant for low-energy γ rays, is blocked for fully stripped isotopes during separation and identification. Therefore the apparent half-life of the γ-decaying isomer during ^{100}Sn's flight through the separator is increased by the factor H. However, H appears twice in Eq. (4.5) because once the ions are implanted in the Si detectors, the expected γ-ray counts is reduced by the factor H through the ICE decay branch.

Upper limits on $T_{1/2}$ as a function of R and γ-ray energy are plotted on Fig. 4.6. In addition, a band corresponding to the theoretical $B(E2)$ range of the isomeric transition is drawn, taken from Refs. [49–51]. From the $B(E2)$ band and the conservative assumption $R = 12.5\%$, it is reasonable

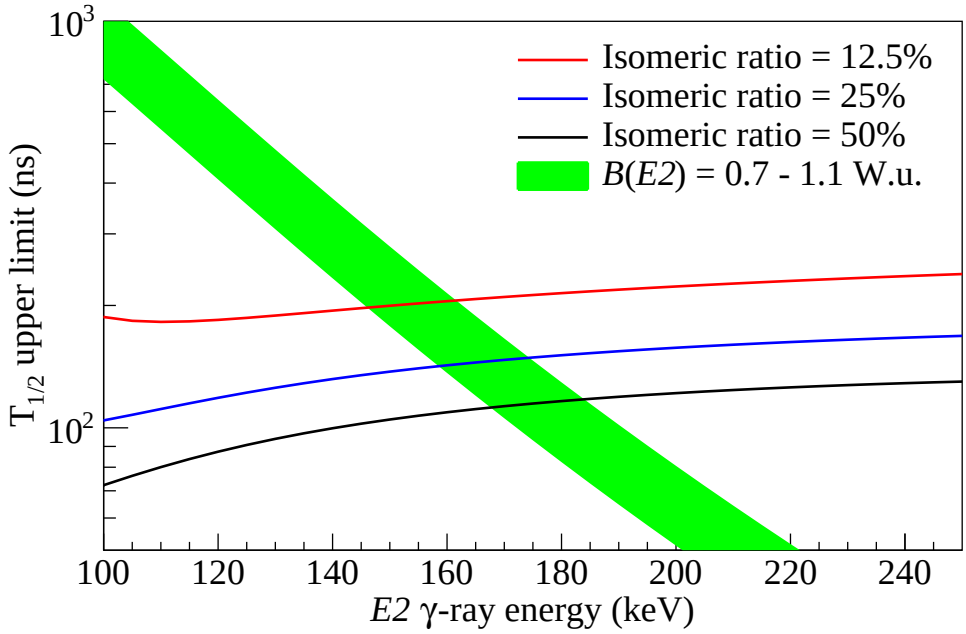

Figure 4.6: Upper limits on the half-life of a hypothetical 6^+ isomer in ^{100}Sn as a function of γ-ray energy at different isomeric ratios. The dependence of the half-life based on the theoretically predicted $B(E2)$ range of the isomeric transition is drawn as a red band.

to suggest $E_\gamma > 140$ keV and $T_{1/2} < 300$ ns for the isomeric transition.

4.2.3 Structure of ^{96}Cd from isomeric γ-ray spectroscopy

A total of 8 new and time-delayed γ rays were observed from ^{96}Cd implantation events, as exhibited in Fig. 4.7. Individual half-lives and intensities (assuming negligible α) of these transitions were consistent with one another within statistical uncertainties, and coincidence analysis results supported the suggestion of a γ-ray cascade from a single isomeric state. These results were confirmed [105] by a separate experiment performed at RIKEN in 2012 by R. Wadsworth et al. Their energy spectrum showed hints of a 1562-keV γ ray, whose energy is a sum of 457- and 1105-keV γ rays; a parallel decay branch is suggested and supported by the comparatively low intensities of the 456/1105-keV γ rays given in Table 4.2.

Table 4.2: Relative intensities of the γ rays in the isomeric decay of ^{96}Cd, normalized to the most intense 811-keV transition.

Energy (keV)	I (%)	Energy (keV)	I (%)
307	$67(^{+36}_{-28})$	811	100
418	$44(^{+28}_{-21})$	1025	$66(^{+42}_{-31})$
441	$57(^{+33}_{-25})$	1041	$76(^{+46}_{-35})$
457	$45(^{+29}_{-21})$	1105	$58(^{+40}_{-29})$

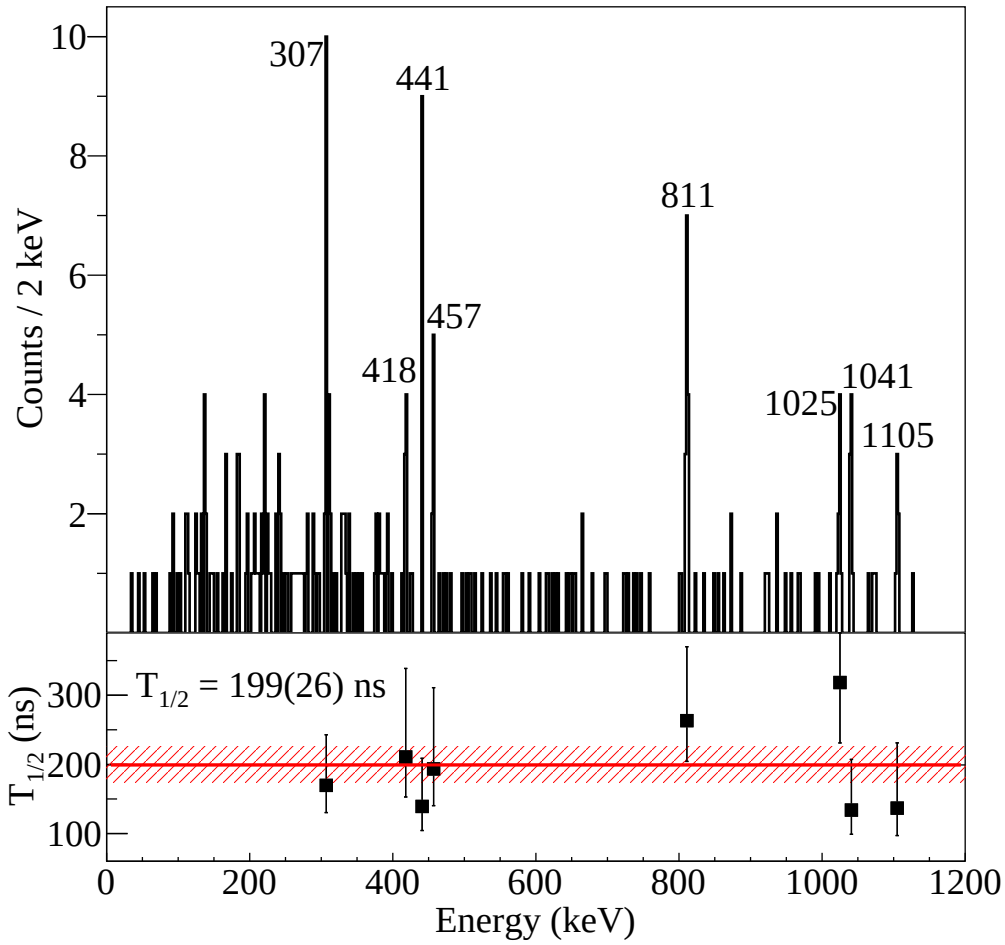

Figure 4.7: Top: γ-ray energy spectrum following ^{96}Cd implantation, where $50 < T_\gamma$ (ns) < 1200. Bottom: individual half-lives of the labeled transitions deduced with the MLH method. The combined half-life and its uncertainty are presented in both numerical values and the fit line with a 1σ band.

The discovery of the isomeric γ-ray transitions enables a quantitative investigation into the excitation level scheme of the heaviest even-even $N = Z$ nucleus, exceeding ^{92}Pd [54]. However, due to limitations in statistics the structure ^{96}Cd must be inferred by combining the experimental information with the most plausible assumptions supported by SM predictions. Several theoretical level schemes generated with different model spaces are compared with the proposed experimental scheme in Fig. 4.8. Good agreement was found between the proposed level scheme and the theoretical calculations, where the order of several transitions is ambiguous due to their similar energies. The experimental energies appear to be intermediate values of *pg* and *gds* results, which suggests a noticeable wavefunction contribution from orbitals across the $N = Z = 50$ shell. Similar energy spacings of the first three excited states are found, consistent with the level scheme of ^{92}Pd and quite different from the $N = 50$ seniority scheme. As noted in Ref. [8], the $T = 0$ *pn* interaction responsible for the spin-gap (16^+) isomer in this nucleus is manifested in low-spin states.

Two possibilities arise for the precursor of the isomeric γ-ray cascade: a low-energy $E2$, or a parity-changing transition. From the number of γ rays observed and the calculated levels, a $14^+ \rightarrow 12^+$ $E2$ transition emerges as a valid option. However, The energy gap is too small compared to any of the observed γ rays. The lowest-energy 307-keV γ ray with $T_{1/2} = 199(26)$ ns corresponds to $B(E2) = 0.04(1)$, which is 2-3 times smaller than the smallest $B(E2)$ observed from ^{93}Ru's ($21/2^+$) isomer. In addition, the 14^+ state would have a lesser likelihood of being isomeric with a prompt $E2$ decay branch to the spin-gap (16^+) isomer. On the other hand, a parity-changing transition could be $E1, M2$ or $E3$. Taking the three lowest-energy γ rays, the transition strengths of each multipolarity are: $B(E1) \sim 10^{-8}$ W.u., $B(M2) \sim 0.1$ W.u., and $B(E3) \sim 10^4$ W.u. The $B(E3)$ value is unphysical, and the same can be said for $B(M2)$ as experimental $B(M2) < 10^{-4}$ W.u. from negative-parity isomers in ^{90}Nb, ^{93}Tc, and ^{96}Ag. In comparison to ^{94}Pd's (19^-) isomer decay with $B(E1) = 2.5(5) \times 10^{-7}$ W.u., the $B(E1)$ value for ^{96}Cd's isomer is small but not unreasonable. Based on the number of γ rays observed, it is likely that $J^\pi_m = 12^-$ or 13^-.

The disambiguation of the spin of the isomer must come from the details of the two wavefunctions corresponding to the 12^- and the 13^- states. The main feature of the 13^- state is the excitation of a nucleon from the $p_{1/2}$ orbital into the $g_{9/2}$ orbital, and it contrasts with the 12^+ state which is entirely composed of unpaired nucleon holes in the $g_{9/2}$ orbital. On the other hand, the 12^- state is an admixture of both; it is reflected by the mean nucleon occupation number in the $p_{1/2}$ orbital of 1.5. An analogy is found between the (19^-) isomer and the (18^-) state in ^{94}Pd. The small $B(E1)$ value from the ^{96}Cd's isomer suggests little overlap between the initial and the final states mediated by the $E1$ operator. Therefore the spin of the isomer is more likely to be (13^-). This argument is supported by the calculations in the *fpg* model space where the 12^- state is almost degenerate with the 12^+ state. But the same reasoning cannot be applied in the *pg* model space. Another remaining issue is a possible $E1$ decay branch to the 14^+ state which becomes available if $J^\pi_m = 13^-$. Accurate descriptions of the negative-parity states and their decay branches are required.

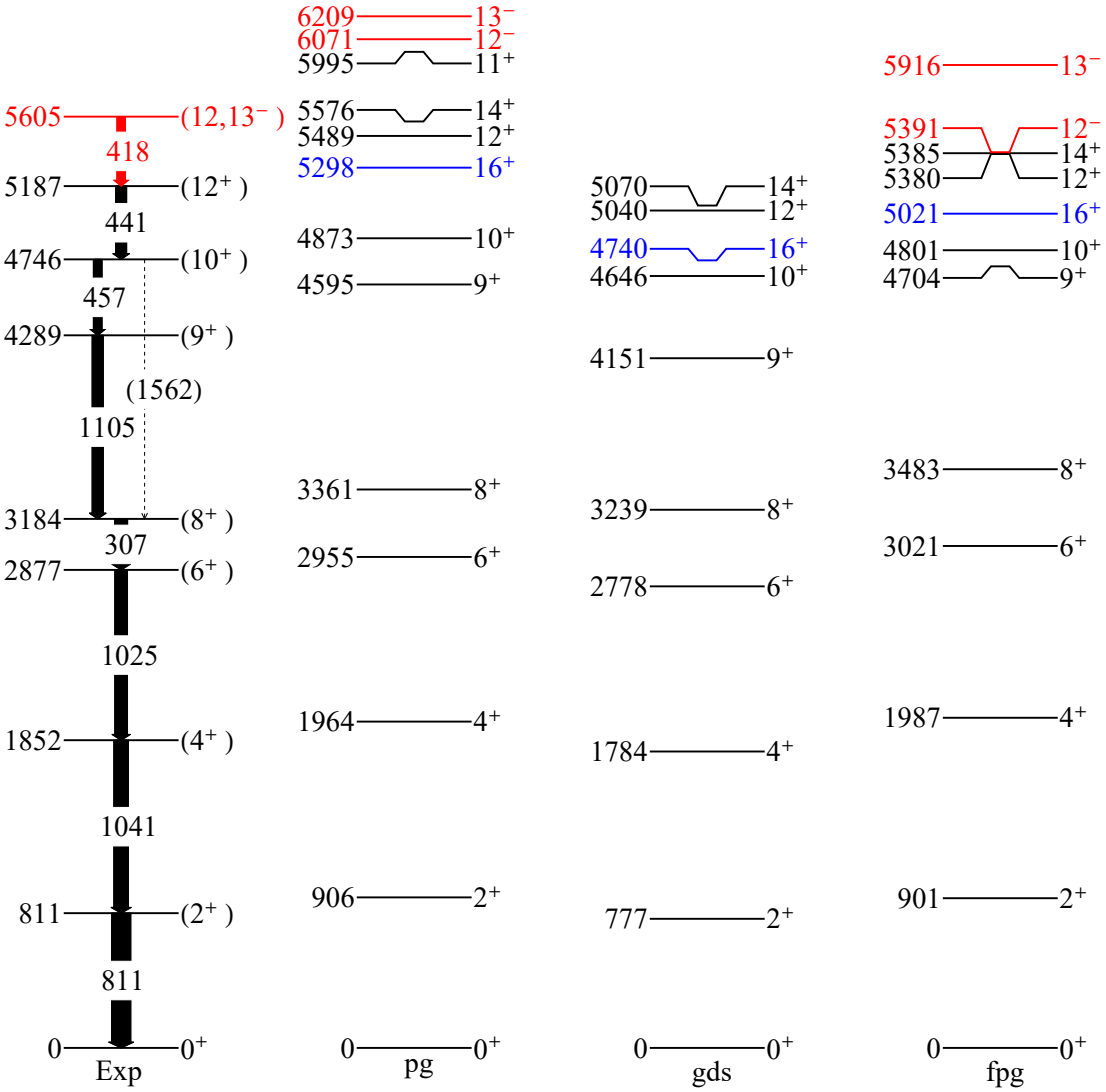

Figure 4.8: Level schemes of ^{96}Cd. The widths of the arrows on the proposed experimental level scheme indicate relative γ-ray intensities. Negative-parity states are drawn in red, and the experimentally verified β-decaying (16^+) isomer [8] is marked in blue for theoretical level schemes. The acronyms of the calculated level schemes indicate model spaces listed in Table 1.1.

4.3 Particle spectroscopy of β, βp, and proton decays

Many of the core objectives of this experiment were investigated with β-decay spectroscopy. The results are presented in two subsections: $T_{1/2}$ measurements (Section 4.3.1), and Q_β measurements (Section 4.3.2). Due to the sheer length and breadth, β-delayed γ-ray spectroscopy results are presented independently under (Section 4.4).

4.3.1 Half-life measurements

Half-life measurements were performed by fitting the β-decay time spectra with parent and daughter decay components as described in Section 3.5.1. The experimental results are presented in Fig. 4.9 and Table 4.3.

Odd-odd $N = Z$ nuclei: ground states and isomers

The half-life measurements of three odd-odd $N = Z$ nuclei are presented: ^{90}Rh, ^{94}Ag and ^{98}In. In addition to the superallowed Fermi decay of the (0^+) ground states, all three of them have been reported [61] to possess GT-decaying spin-gap isomers created by $T = 0$ attractive pn interactions. Due to the large difference between the half-lives, the decay time spectra were plotted and fitted in logarithmic time scales as prescribed in Ref. [106] to equalize effective binning for both decay channels. The results are shown on the left side of Fig. 4.10.

In each of the half-life fits, the constant background decay component becomes an exponential in $\ln(t)$. The dark green dashed line corresponds to the β-decay daughter component. For ^{94}Ag, the (21^+) isomeric state was too scarcely populated in this experiment to merit an independent $T_{1/2}$ measurement. Thus this additional parent decay component (light green) was constructed with the adoption of the literature half-life (0.40(4) s [2]). For ^{98}In, significant βp branching of the (9^+) isomeric state could not be ignored. While the βp decay channel did not directly contribute to the spectrum due to the maximum strip energy cut ($E < 1500$ keV), β decays from the βp daughter ^{97}Ag were included in the fit (light green dashed line). The obtained half-lives for both the fast superallowed Fermi component and the slow GT component were more precise than the previous literature values by almost an order of magnitude.

$N = Z - 1$ nuclei

The half-life measurements of the exotic $N = Z-1$ nuclei ^{91}Pd, ^{95}Cd, ^{97}In, and ^{99}Sn were performed for the first time. MLH fits were used, and the decay curves and the $T_{1/2}$ values are shown on the left side of Fig. 4.11.

Compared to the other $N = Z - 1$ isotopes, the initial fit result for ^{97}In reported a significantly smaller parent-decay amplitude; the number of decay events determined from the fit was only 31(3)% of the number of ^{97}In implantations, whereas the weighted average from ^{91}Pd, ^{95}Cd, and ^{99}Sn was 48(2)%. To resolve this mystery, it was postulated that a fraction of ^{97}In isotopes were produced in a proton-emitting isomeric state with a half-life in the range of 3 to 140 μs. These events

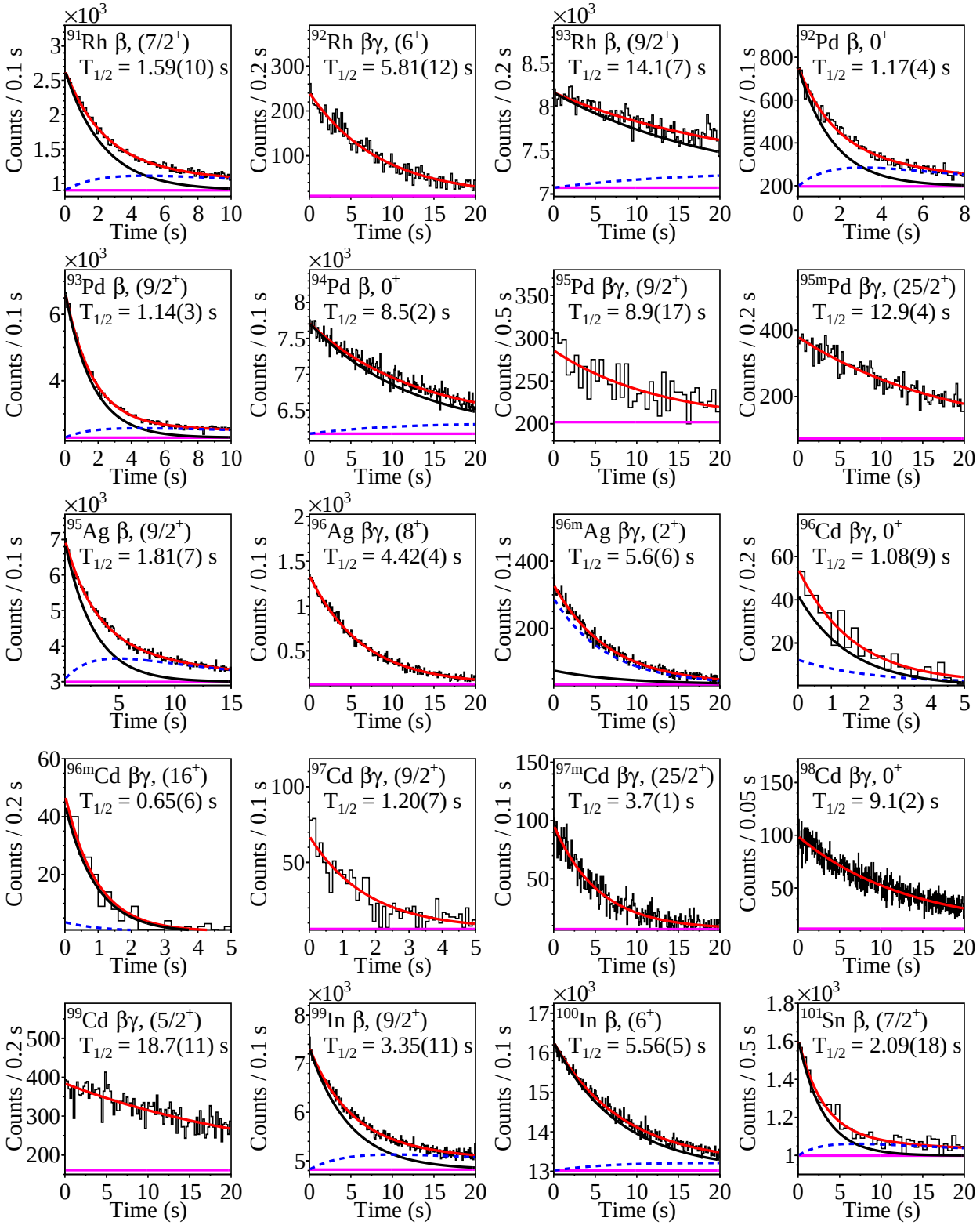

Figure 4.9: β-decay time distributions of isotopes and isomeric states. This list is not exhaustive. Spectra obtained with γ-ray gates are labeled as "$\beta\gamma$" beside isotope labels. χ^2 and MLH fits were performed to obtain the half-lives.

Table 4.3: Properties of β-decaying isotopes and isomers (spin J, isomeric ratio R, $T_{1/2}$ values, isomeric state energy E_x, and Q_{EC} values) with $N \geq Z \geq 45$ and $T_{1/2} < 20$ s obtained from β-decay data. E_x marked with & are NuShellX results, and those marked with # are extrapolated predictions taken from Ref. [2].

Nucleus	J^π	R (%)	$T_{1/2}$ (s)		E_x (MeV)	Q_{EC} (MeV)	
			This work	Literature		This work	Literature
^{90}Rh	(0^+)		0.0280(33)	0.015(7)		11.62(58)	12.9(4)
^{90m}Rh	(7^+)	86(3)	0.52(2)	1.1(3)	0.500&		
^{91}Rh	$(7/2^+)$		1.59(10)	1.60(15)			9.44(40)
^{92}Rh	(6^+)		5.81(12)	4.66(25)			11.302(5)
^{92m}Rh	(2^+)	3.4(28)	2.54(44)	0.53(37)	0.05(10)#		
^{93}Rh	$(9/2^+)$		14.1(7)	13.9(16)			8.205(3)
^{92}Pd	0^+		1.17(4)	1.1(3)		7.47(29)	7.93(50)
^{93}Pd	$(9/2^+)$		1.14(3)	1.15(5)			9.87(40)
^{94}Pd	0^+		8.5(2)	9.0(5)			6.807(5)
^{95}Pd	$(9/2^+)$		8.9(17)	7.5(5)			8.376(5)
^{95m}Pd	$(21/2^+)$	77(11)	12.9(4)	13.3(3)	1.875		
^{94}Ag	(0^+)		0.0277(15)	0.037(18)		12.45(47)	13.69(64)
^{94m}Ag	(7^+)	77(3)	0.51(3)	0.55(6)	0.521&		
^{94n}Ag	(21^+)	2.4(3)		0.40(4)	6.35(50)#		
^{95}Ag	$(9/2^+)$		1.81(7)	1.76(9)			10.36(40)
^{96}Ag	(8^+)		4.42(4)	4.44(4)			11.67(9)
^{96m}Ag	(2^+)	22(3)	5.6(6)	6.9(6)	0.00(5)#		
^{96}Cd	0^+		1.08(9)	0.88(9)		8.65(46)	8.94(41)
^{96m}Cd	(16^+)	22(3)	0.65(6)	0.30(11)	5.3(20)#		
^{97}Cd	$(9/2^+)$		1.20(7)	1.10(8)			10.38(32)
^{97m}Cd	$(25/2^+)$	37(3)	3.7(1)	3.8(2)	1.5(5)#		
^{97n}Cd	$(1/2^-)$	5.3(10)	0.78(7)				
^{98}Cd	0^+		9.1(2)	9.2(3)		5.448(30)	5.430(58)
^{99}Cd	$(5/2^+)$		18.7(11)	16(3)			6.781(6)
^{98}In	(0^+)		0.0290(12)	0.037(5)		12.76(37)	13.74(21)
^{98m}In	(9^+)	59(2)	1.11(9)	1.03(13)	0.573&		
^{99}In	$(9/2^+)$		3.35(11)	3.1(2)			8.55(20)
^{100}In	(6^+)		5.56(5)	5.85(16)			9.88(18)
^{100}Sn	0^+		1.19(10)	1.11(15)		7.16(19)	7.03(35)
						7.78(19)	
^{101}Sn	$(7/2^+)$		2.09(18)	1.97(16)			8.30(42)

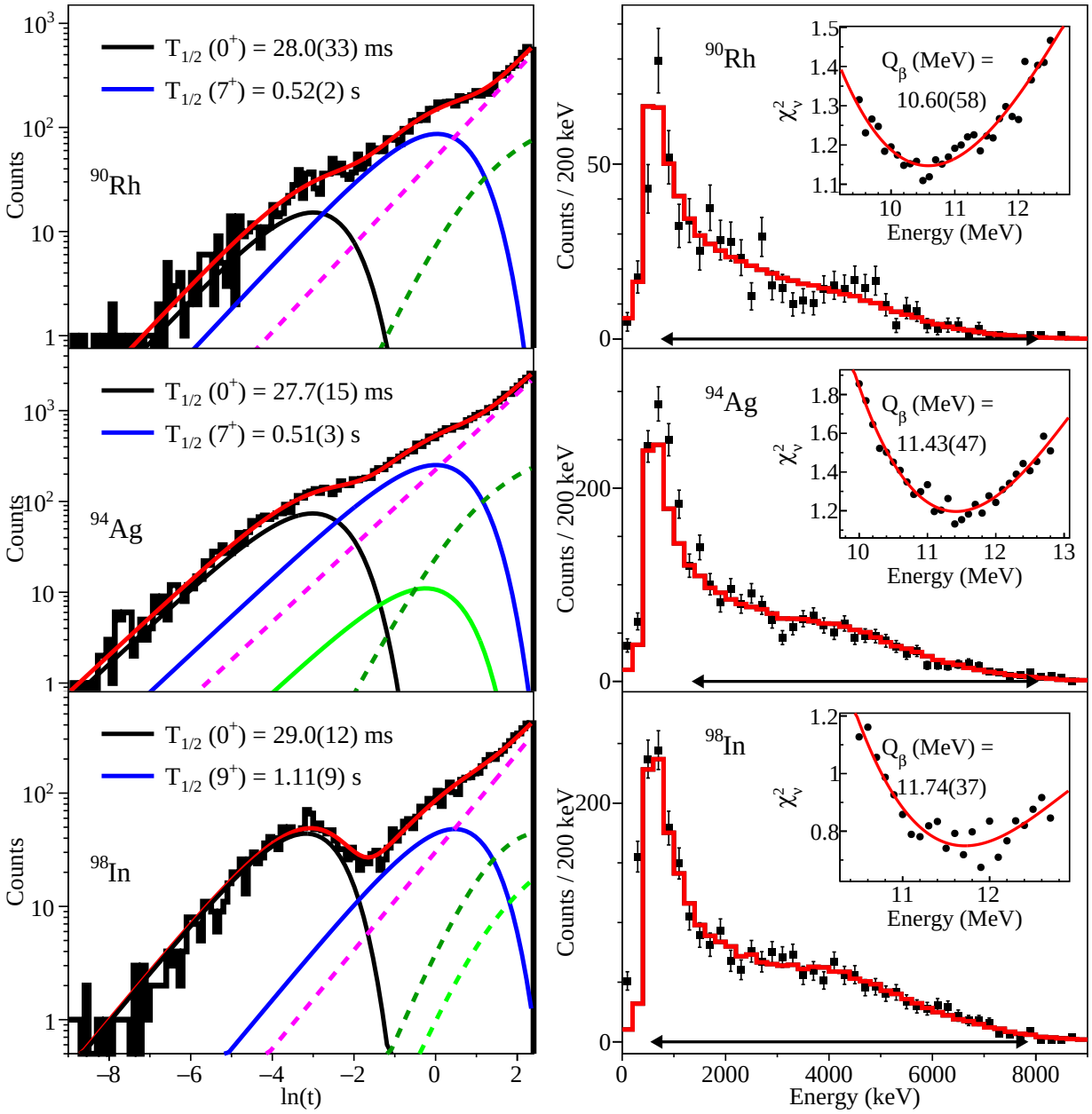

Figure 4.10: Left: half-lives of ground and isomeric states of odd-odd $N = Z$ nuclei; the parent decay components are presented as solid lines, and background and daughter decay components are shown as dashed lines. Right: Q_β measurements of the same nuclei in reference to the ground-state energy; both the ground state and the isomeric state components were included.

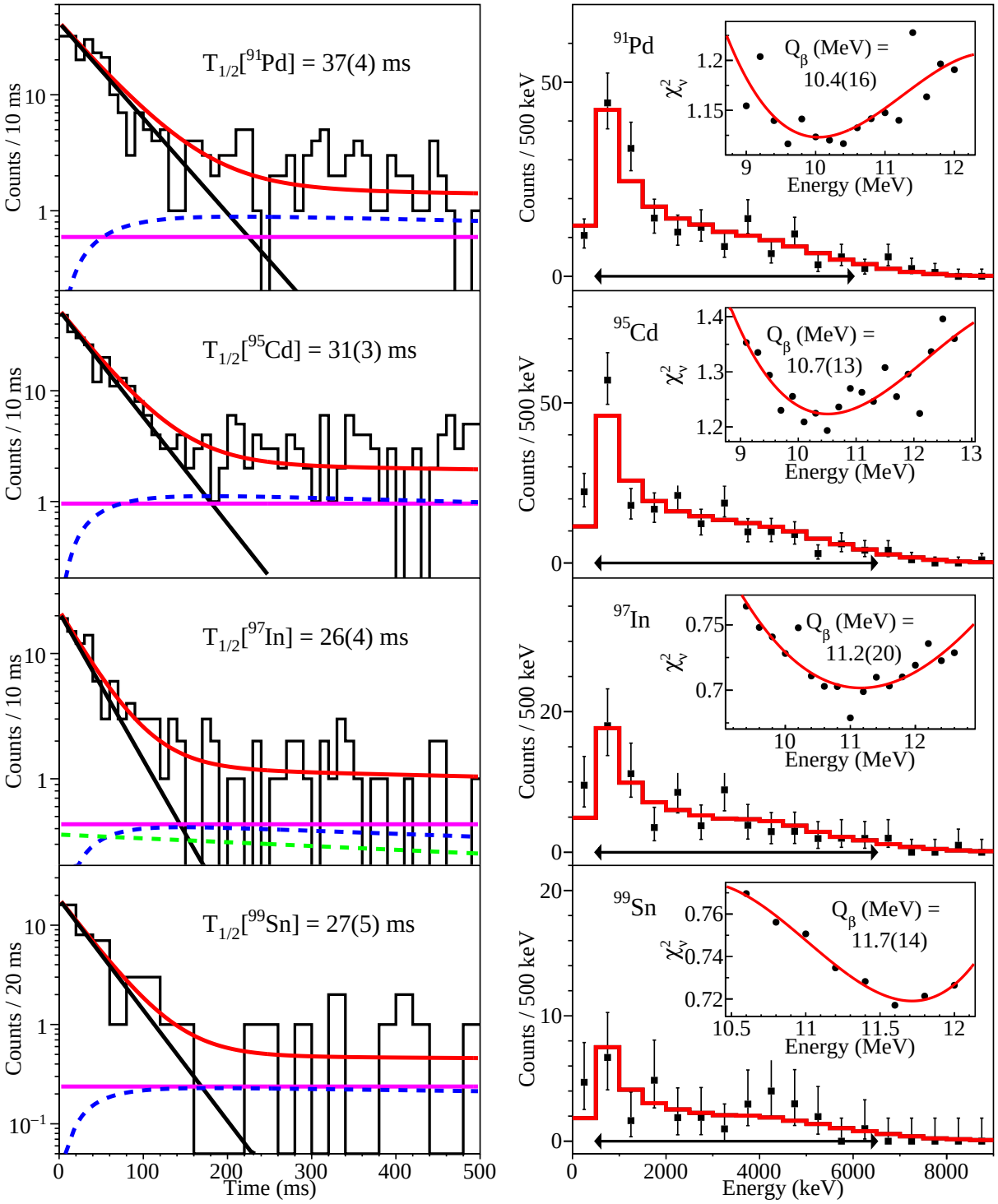

Figure 4.11: Left: half-lives of $N = Z-1$ nuclei obtained from experiment. MLH fits were performed with separate components: parent decay (black), daughter decay (dashed blue), and background (magenta). For ^{97}In, the relative deficit of the parent decay amplitude was compensated by a β-decay component of ^{96}Cd (dashed green) which would be populated by $1p$ emission from a hypothetical isomeric state. Right: Q_β analysis results of these nuclei.

would not be detected in WAS3ABi because of the 600-μs deadtime window immediately following ion implantation. A revised fit containing the ^{96}Cd component (proton daughter of ^{97}In, dashed green line in Fig. 4.11) reported 39(5)% population of the hypothetical isomer. The implications of two possible states in ^{97}In are discussed in Section 4.3.3. A plot showing the systematics of the half-lives of $N = Z - 1$ nuclei from $Z = 41$ to 50 is shown in Fig. 4.12. Being near the proton dripline, isotopes with odd-Z are highly susceptible to spontaneous one-proton emission and their short half-lives verify that the proton dripline has been reached. On the other hand, from the long β-decay half-lives exceeding 10 ms, it is concluded that the even-Z isotopes are not yet susceptible to direct proton emission.

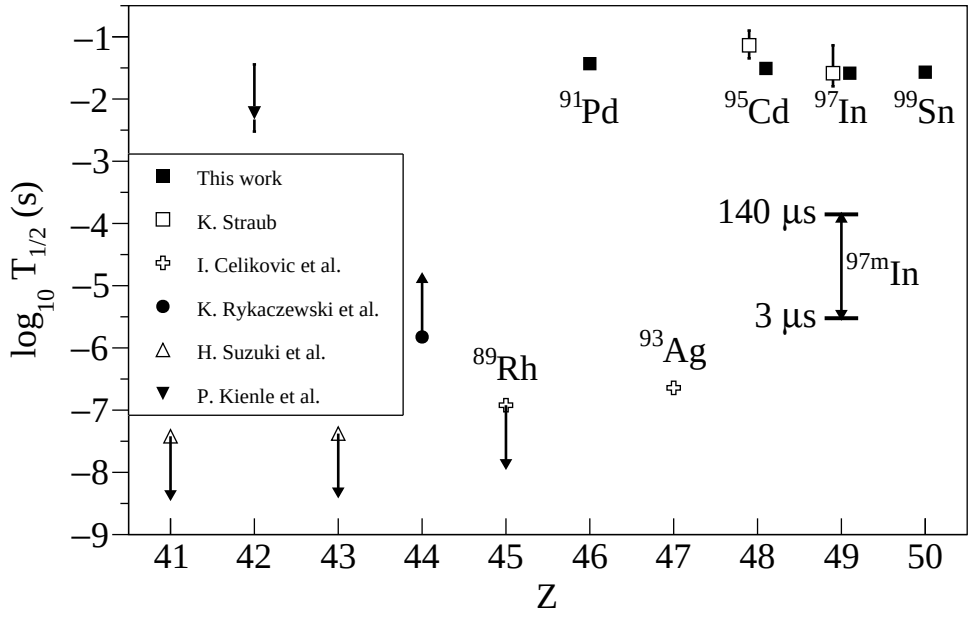

Figure 4.12: Half-life systematics of $N = Z-1$ nuclei with valence protons in the $g_{9/2}$ orbital. Odd-Z nuclei are proton unbound and possess very short half-lives compared to even-Z counterparts. For ^{97}In, a long-lived β-decaying state has been confirmed with better precision. Circumstantial evidence points to a short-lived proton-emitting state ^{97m}In with upper and lower limits on its half-life.

4.3.2 Experimental Q_β and Q_{EC} values

The method using Geant4 simulations described in Section 3.5.2 was used to obtain experimental Q_β values. It was found in general that the Q_β results were more reliable for small correlation time windows ($t < 5$ s) or with very clean γ-ray gates, where the signal-to-background ratios of decay events remain high. Besides ^{98}Cd, few long-lived nuclei possessed dominant β-decay branches accompanied by a high-energy γ ray. Consequently only short-lived $N \leq Z$ isotopes were subjected to Q_β analysis.

Q_β and Q_{EC} values of ^{92}Pd, ^{96}Cd, and ^{100}Sn

Q_β of three even-even, $N = Z$ isotopes ^{92}Pd, ^{96}Cd, and ^{100}Sn were measured with γ-ray gates. The Q_β measurement of ^{92}Pd was performed with the newly discovered 257-keV γ-ray shown in Fig. 4.20 as a selection cut, and its result is shown in the top plot of Fig. 4.13. The conversion of the resulting $Q_\beta = 6.27(29)$ MeV into the Q_{EC} value involves the addition of the 0.257-MeV γ-ray energy, $2m_e = 1.022$ MeV, as well as the (2^+) isomer's energy, which is listed as 0.05(10) MeV [2]. The final value of $Q_{EC} = 7.47(29)$ MeV was derived, which agrees with the theoretical prediction of 7.93(50) MeV listed in Table 4.3. Combined with $T_{1/2} = 1.17(4)$ s, the resulting $\log(ft)$ value was 3.84(11) assuming 100% β-decay branching ratio to the yrast (lowest energy state for a given spin and parity J^π) (1^+) state - a reasonable value for an allowed $0^+ \rightarrow 1^+$ GT decay.

The Q_β measurement of the ground state of ^{96}Cd was performed after gating on the 421-keV γ ray shown in Fig. 4.22. The conversion of the resulting $Q_\beta = 7.21(46)$ MeV into the Q_{EC} value involves the addition of the 0.421-MeV γ-ray energy and $2m_e = 1.022$ MeV. Unlike ^{92}Pd, the final (2^+) state in ^{96}Ag was considered degenerate with the (8^+) ground state [2]. Thus for ^{96}Cd $Q_{EC} = 8.65(46)$ MeV was deduced, also consistent with the theoretical prediction of 8.94(41) MeV listed in Table 4.3. Combined with $T_{1/2} = 1.16(8)$ s and assuming a 64(3)% β-decay branching ratio to the yrast (1^+) state in ^{96}Ag, the resulting $\log(ft)$ value was 4.35(15) - also reasonable for an allowed $0^+ \rightarrow 1^+$ GT decay.

The experimental Q_β spectrum of ^{100}Sn was obtained by gating on the ^{100}In γ rays shown in Fig. 4.31, except for the 2048-keV γ ray due to low statistics. The χ^2 evaluation result is $Q_\beta = 4.04(18)$ MeV, which is higher than the 3.29(20) MeV reported in Ref. [14] but consistent with 3.75(9) MeV reported in Ref. [69] within 2σ, based on an independent analysis of the same dataset. The low uncertainty in the result from Ref. [69] is due to higher statistics in the β-decay energy spectrum without applying the γ-ray gates. The Q_{EC} value of ^{100}Sn depends on the structure of the daughter nucleus ^{100}In, and is discussed in Section 4.4.7.

Q_β and ft values of odd-odd $N = Z$ nuclei

Odd-odd $N = Z$ nuclei ^{90}Rh, ^{94}Ag, and ^{98}In undergo fast superallowed Fermi decays and possess large Q_β values. For these isotopes, β-decay energy spectra were generated from decay events within 100 ms after implantation and corrected for background. Despite setting a short time window to improve the purity of the clean Fermi decay, a significant fraction of the Q_β spectrum originated from isomeric state decays due to the high population ratios (see Table 4.3). Therefore the isomeric decay channels were included in the Q_β evaluation.

At each trial energy, a simulated Q_β spectrum was generated for each isomeric decay branch and scaled according to its β-decay branching ratio based on γ-ray intensities. The input Q_β value of this spectrum was adjusted by the excitation energies of both the initial and the final state. One major uncertainty arises from the excitation energy of the isomer. For ^{94}Ag, $E(7^+) = 660$ keV was proposed from shell-model calculations [107] while NuBASE2012 reports a conservative estimate of 1350(400) keV as the excitation energy.

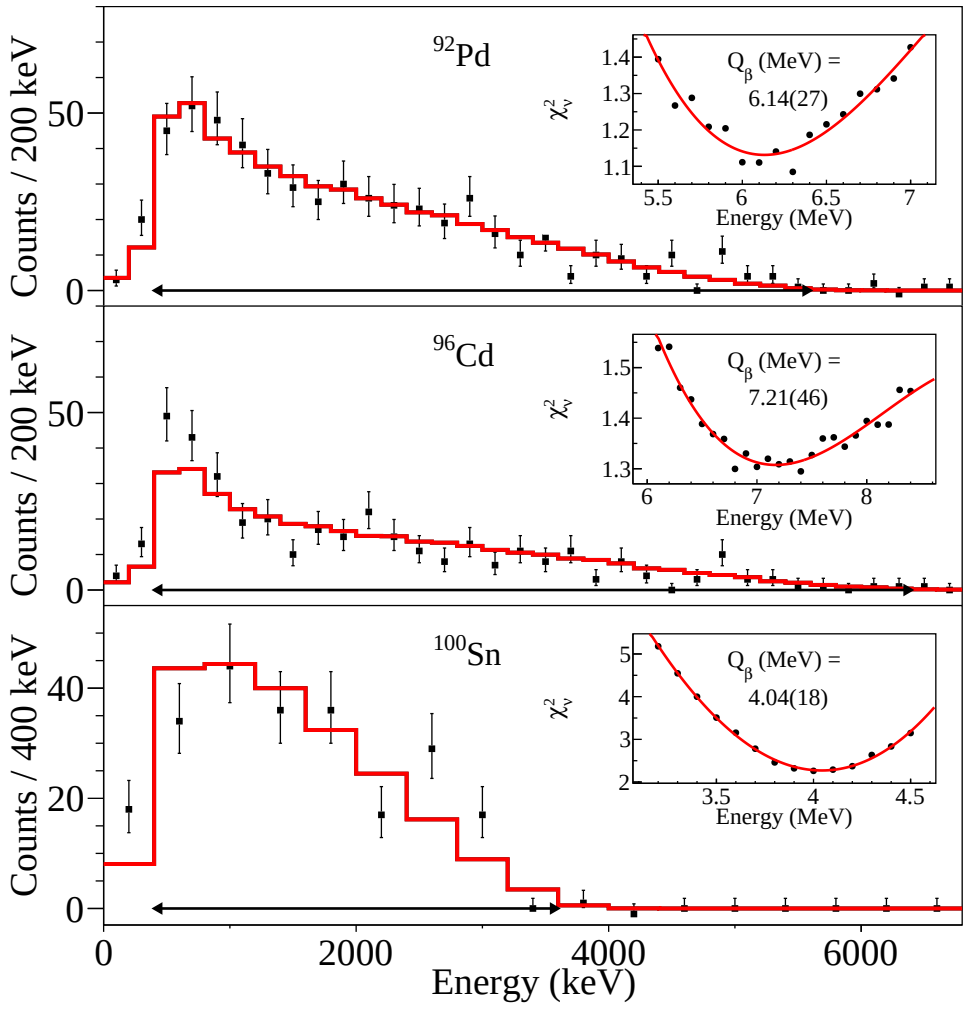

Figure 4.13: Q_β spectra of ^{92}Pd (top), ^{96}Cd (middle), and ^{100}Sn (bottom) obtained from γ-ray gates and fitted with different trial Q_β energies.

The simulated Q_β histograms were added and compared to the experimental energy spectra. The results are shown on the right side of Fig. 4.10. Conversion of the ground-state to ground-state Q_β values into Q_{EC} requires just the addition of $2m_e = 1.022$ MeV for β^+ decays. Two γ-ray transitions with noticeable internal conversion coefficients from the β-decay of ^{98m}In are 147 and 198 keV, with ICE emission probability of 27.5(4)% and 11.8(2)% respectively. These effects are visible in the first two bins of the Q_β spectrum of ^{98}In, The sum of the probability-weighted energies is 64(1) keV, which is small compared to the systematic uncertainty of the energy of the (9^+) isomer; this energy correction was not included in the Q_{EC} calculation.

The $\log(ft)$ values of the ^{98m}In were were 4.8(4) for the decay into the 6585-keV (10^+) state with $I_\beta = 4.9^{+4.5}_{-2.9}$% mentioned in Section 4.4.5, and 4.8(2) for the decay into the 2428-keV (8^+) isomer. These are consistent with the known $\Delta J = 1$ GT-decay $\log(ft)$ systematics. The raw ft values for the superallowed Fermi decays were $2.1(6) \times 10^3$ s for ^{90}Rh, $3.2(7) \times 10^3$ s for ^{94}Ag, and $3.4(6) \times 10^3$ s for ^{98}In. In comparison to the up-to-date corrected $\mathcal{F}t$ value of 3072.27(62) [37] with corrections on the order of 1%, the preliminary ft measurements are consistent within the large statistical uncertainties caused by large δQ_β. Much more precision in the mass measurement of these odd-odd $N = Z$ nuclei is needed to include them in the quantitative discussion of the consistency of the $\mathcal{F}t$ value.

$N = Z - 1$ nuclei

The $N = Z - 1$ nuclei ^{91}Pd, ^{95}Cd, ^{97}In, and ^{99}Sn undergo predominantly ground-state to ground-state Fermi decays with large Q_β values. The results are shown on the right side of Fig. 4.11. Combining the $T_{1/2}$ and Q_β measurements assuming 100% ground-state to ground-state transitions ($Q_{EC} = Q_\beta + 2m_e$), the corresponding $\log(ft)$ values are calculated and tabulated in Table 4.4. These $\log(ft)$ values are quite small and consistent with $\Delta J = 0$ allowed decays, as expected from $T_z = -1/2$ nuclei with a large energy window and the similarity of the initial and the final states.

Table 4.4: Summary of β-decay information on ^{91}Pd, ^{95}Cd, ^{97}In, and ^{99}Sn, in reference to Fig. 4.11. 100% ground-state to ground-state β-decay branching ratios were assumed in calculating the $\log(ft)$ values. $T_{1/2}$ constraints for the proton-emitting $(1/2^-)$ isomer ^{97m}In are also presented.

Nucleus	J^π	$T_{1/2}$ (ms)		Q_{EC} (MeV)	$\log(ft)$
		This work	Literature		
^{91}Pd	$(7/2^+)$	37(4)	> 1.5 μs [61]	11.4(16)	3.4(4)
^{95}Cd	$(9/2^+)$	31(3)	73^{+53}_{-28} [18]	11.7(13)	3.4(3)
^{97}In	$(9/2^+)$	26(4)	26^{+47}_{-10} [18]	12.2(20)	3.4(5)
^{97m}In	$(1/2^-)$	3-140 μs			
^{99}Sn	$(9/2^+)$	27(5)	> 200 ns [18]	12.7(14)	3.5(3)

Masses of isotopes near the proton dripline

First Q_β measurements for the heaviest $N \leq Z$ nuclei enable tests of different mass models at the proton dripline near ^{100}Sn. Four independent mass models were used to compare with experimental results: the finite-range droplet model (FRDM) [108], the Koura-Tachibana-Uno-Yamada model (KTUY05) [109], the Duflo-Zuker model (DZ) [110], and the Hartree-Fock-Bogoliubov model (HFB27) [111]. An additional comparison was provided by empirical extrapolations the atomic mass evaluation (AME2012) [112]. The comparisons to the experimental Q_{EC} values are shown in Fig. 4.14. For the proton-unbound ^{93}Ag nucleus, its $S_p = -1060(30)$ keV [96] was used with the mass of ^{92}Pd to calculate its Q_{EC}value.

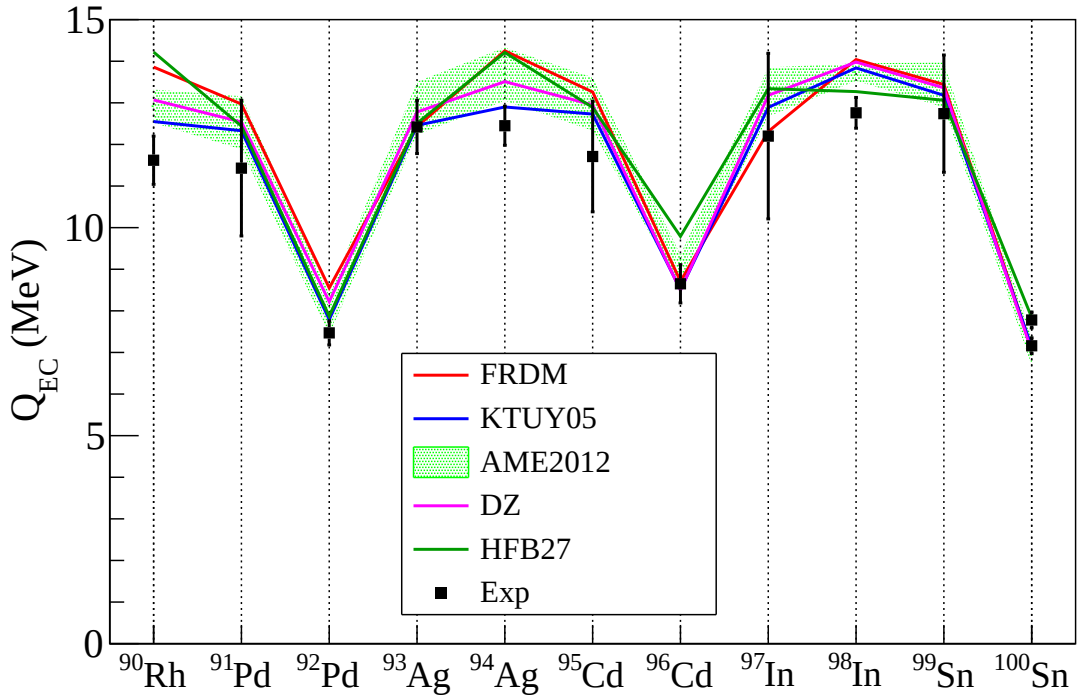

Figure 4.14: Comparison of experimental Q_{EC} values of the select $N \leq Z$ nuclei measured in this work to different mass models and extrapolated data (see text for references). For AME2012, the 1σ-uncertainty band is drawn. For ^{100}Sn, two Q_{EC} values inferred from the first two possible level schemes shown in Fig. 4.32 are plotted.

Several general remarks can be made. First, the trend of low Q_{EC} values of even-even, $N = Z$ nuclei is replicated by the models. These nuclei benefit maximally from pairing interactions and the attractive pn interaction. Second, the experimental Q_{EC} values for odd-odd $N = Z$ nuclei are consistently lower than the predictions. Underestimation of the attractive $T = 0$ pn interaction in these nuclei may be the cause. Third, it is ambiguous to rank the different mass models; KTUY05 performs rather well for most of the nuclei except ^{98}In, and HFB27 in general predicts poorly but has the closest Q_{EC} value for ^{98}In. Lastly, large deviations of predicted Q_{EC} values are present for

odd-odd $N = Z$ nuclei.

4.3.3 Limits of proton binding in ^{97}In

Unlike the other odd-Z, $T_1 = -1/2$ nuclei, ^{97}In undergoes β decay with a $T_{1/2}$ and Q_β similar to even-Z counterparts. On the other hand, as elaborated in Section 4.3.1, missing decay correlations for ^{97}In can be explained by suggesting another state which decays almost completely within the deadtime of WAS3ABi of 600 μs. There is a 3-μs lower limit on this hypothetical state's half-life, which is based on the perseverance of ^{97}In isotopes through the separator [96]. The upper limit on the half-life of this isomer was determined by assuming less than 4 proton-emitting isomers to survive after 600 μs. The basis for choosing this number was based on Poisson statistics, where zero observations of protons lie outside of the 2σ confidence level with $1\sigma(4 \text{ samples}) = 2$. The derived upper limit was 140 μs. Based on the trend illustrated in Fig. 4.12, this short-lived state is likely to be a proton emitter. On the other hand, no single-pixel, proton-emission candidate events have occurred within the correlation time window. A conservative lower limit on the proton emission $T_{1/2}$ of the $(9/2^+)$ state was determined by taking the -2σ value of the β-decay $T_{1/2}$ (18 ms) and multiplying by the number of $(9/2^+)$ states (128) divided by 4 to yield 576 ms.

A theoretical support for a coexistence of two states comes from a near-degeneracy of the $p_{1/2}$ and the $g_{9/2}$ orbitals for $N \sim Z$ nuclei approaching ^{100}Sn. At the moment designation of ground and isomeric states is ambiguous. For the proton-emitting state, Q_p values from various mass models (using ground-state masses) are compared with estimates given by a simple theory on proton emission [9], shown as the inset of Fig. 4.15. Two alternatives are proposed: proton emission with $l = 1$ from the $p_{1/2}$ orbital and $l = 4$ from the $g_{9/2}$ orbital. Due to the centrifugal barrier, proton emission from the $p_{1/2}$ is favored over the $g_{9/2}$. The upper and lower limits on the half-lives can be translated into a range of the emitted proton energy Q_p. The upper limit on the Q_p value from the $g_{9/2}$ state is 0.65 MeV, which is less than the 0.66-0.76 MeV predicted for the emission with $l = 1$. Then ^{97}In is suggested to have a ground state spin and parity of $9/2^+$, with a proton-emitting isomeric state with spin $1/2^-$. The energy difference between the two states is reflected in Fig. 4.15, which could be as large as, or greater than 760 keV if the $(9/2^+)$ state lies above the $S_p = 0$ line. The S_p value of the $(9/2^+)$ could also be deduced with Q_β spectroscopy or mass measurements; the current experimental Q_β value is too imprecise to be useful.

Different mass models diverge in their mass predictions up to 1 MeV for ^{97}In, and the interpretation from the experimental values happen to lie in between them. A decay spectroscopy experiment which is able to measure both the Q_β from the $(9/2^+)$ state and the energy of the proton emitted from the $(1/2^-)$ state would serve as a benchmark test of these mass models.

4.3.4 βp branching ratios

Branching ratios and half-lives of β-delayed proton emission were measured by analyzing the βp decay time distributions. Except for the most exotic isotopes where statistics are low, βp decay time spectra are shown in Fig. 4.16. The number of βp events was determined from either counting

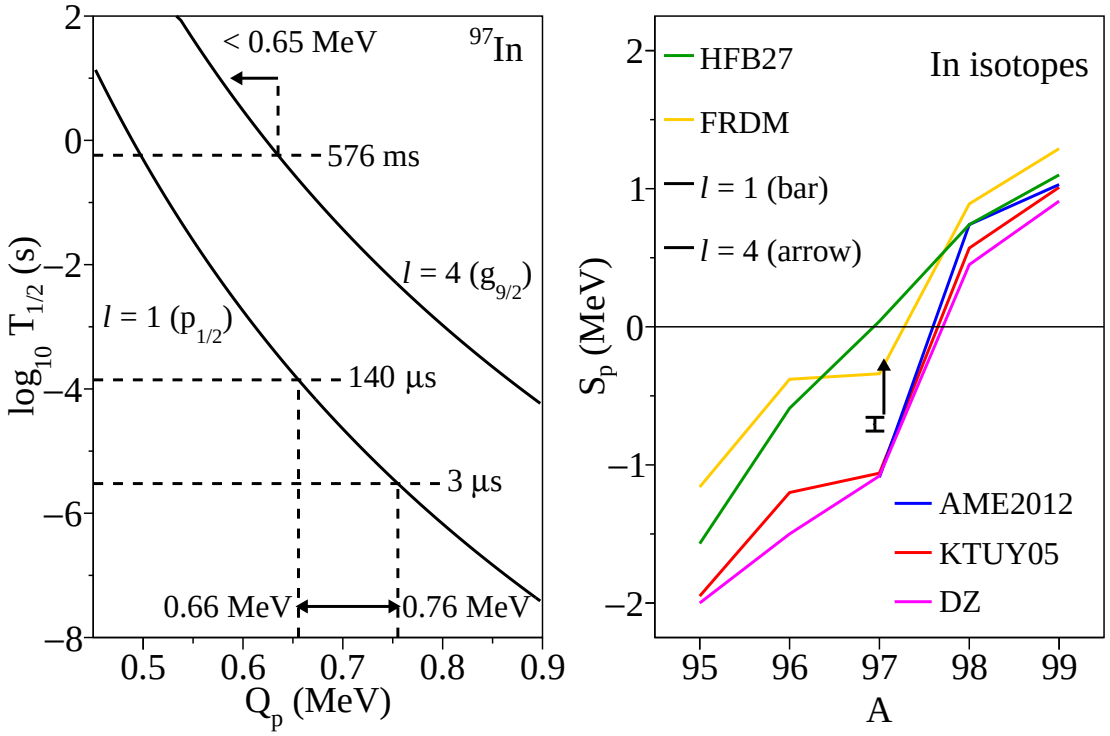

Figure 4.15: Left: Q_p values of ^{97}In based on the half-life limits for $l = 1$ and $l = 4$, corresponding to proton emissions from either the $\pi p_{1/2}$ or the $\pi g_{9/2}$ orbital. A theoretical description of the $T_{1/2}$-Q_p relationship is given in Ref. [9] and derived in Appendix C. Right: S_p values as a function of mass number for In isotopes. The predictions diverge for ^{97}In, and the Q_p values deduced on the left plot occur as intermediate values.

(for low-statistics data) or the integral of the parent fit function, corrected by a run-dependent WAS3ABi deadtime loss. For isotopes without isomeric states, the βp branching ratio $b_{\beta p}$ was simply calculated as $N_{\beta p}/N_{ion}$; if one or more isomeric states were present, $b^i_{\beta p} = N^i_{\beta p}/N^i$ where i is the index for each state. The results and comparisons to literature values are tabulated in Table 4.5, where the half-lives between βp- and β-decay data agree with one another. For several states and isotopes with insufficient statistics, individual $T_{1/2}$ measurements using βp data were not performed due to contributions from isomeric states and daughter nuclei - complicating the $b_{\beta p}$ analysis. The $b_{\beta p}$ values for these cases were obtained by adopting the β-decay half-lives in the βp decay time analysis.

For $N = Z$ nuclei, βp emission from both the ground and isomeric states were analyzed in the same way as the β-decay half-life analysis. The population of the (21^+) isomer in ^{94}Ag was too low to merit an independent measurement of its half-life and $b_{\beta p}$. So the literature values were used in the half-life analysis to obtain $T_{1/2}$ and $b_{\beta p}$ for the (0^+) ground state and the (7^+) isomer. The statistics were low for $N = Z - 1$ nuclei, and βp events from these isotopes were counted in a 200-ms correlation time window. The number of background βp events was determined with a backward-time correlation and subtracted from the $t > 0$ βp events to obtain $b_{\beta p}$.

For ^{96}Ag, the half-lives of the two states were too similar within the finite correlation time range of 20 s to perform independent $T_{1/2}$ measurements using βp data. Instead, the half-lives from β-decay data were adopted to determine the contributions to the βp time spectrum and subsequently the $b_{\beta p}$ values. The $b_{\beta p}$ analysis for ^{96}Cd was complicated by the fact that its β decay from the ground state and the isomeric state populates both the (8^+) and the (2^+) states in ^{96}Ag, each of which has a non-negligible $b_{\beta p}$. Rather than fitting the βp time spectrum, an alternative approach was taken. The βp γ-ray half-life analysis concluded that all of the βp activity originates from the (16^+) isomer. Then the intensity of the 691-keV γ ray to the isomeric $(21/2^+)$ state in ^{95}Pd was used to determine the $b_{\beta p}$ value of ^{96m}Cd.

4.3.5 Direct proton emission search in ^{94}Ag

There have been reports of direct $1p$ and $2p$ emission from ^{94}Ag's (21^+) isomeric state [10, 11]. Based on its low isomeric ratio, attempts to confirm proton emission from this state were challenging. Nevertheless, proton spectroscopy with WAS3ABi is immune from losses in statistics due to the β-particle correlation efficiency, EC, and the EURICA efficiency. The result of the direct proton emission search from ^{94}Ag is shown in Fig. 4.17.

No evidence was found at the reported $1p$ proton energies. 5 counts were observed at 1900 keV, consistent with the total energy of $2p$ emission. The half-life obtained from the 5 events was $0.56^{+0.45}_{-0.17}$ s, which is consistent with either isomeric state's half-life. Note that this energy region overlaps with βp decays, which may generate single-pixel EC-induced proton events. Another point of contention is the branching ratio; for $1p$ decays, the branching ratios for 790(30) keV and 1010(30) keV were 1.9(5)% and 2.2(4)% - about 4 times greater than 0.5(3)% for the $2p$ decay. If the counts at 1900 keV are genuinely $2p$ events, approximately 20 counts should have been observed

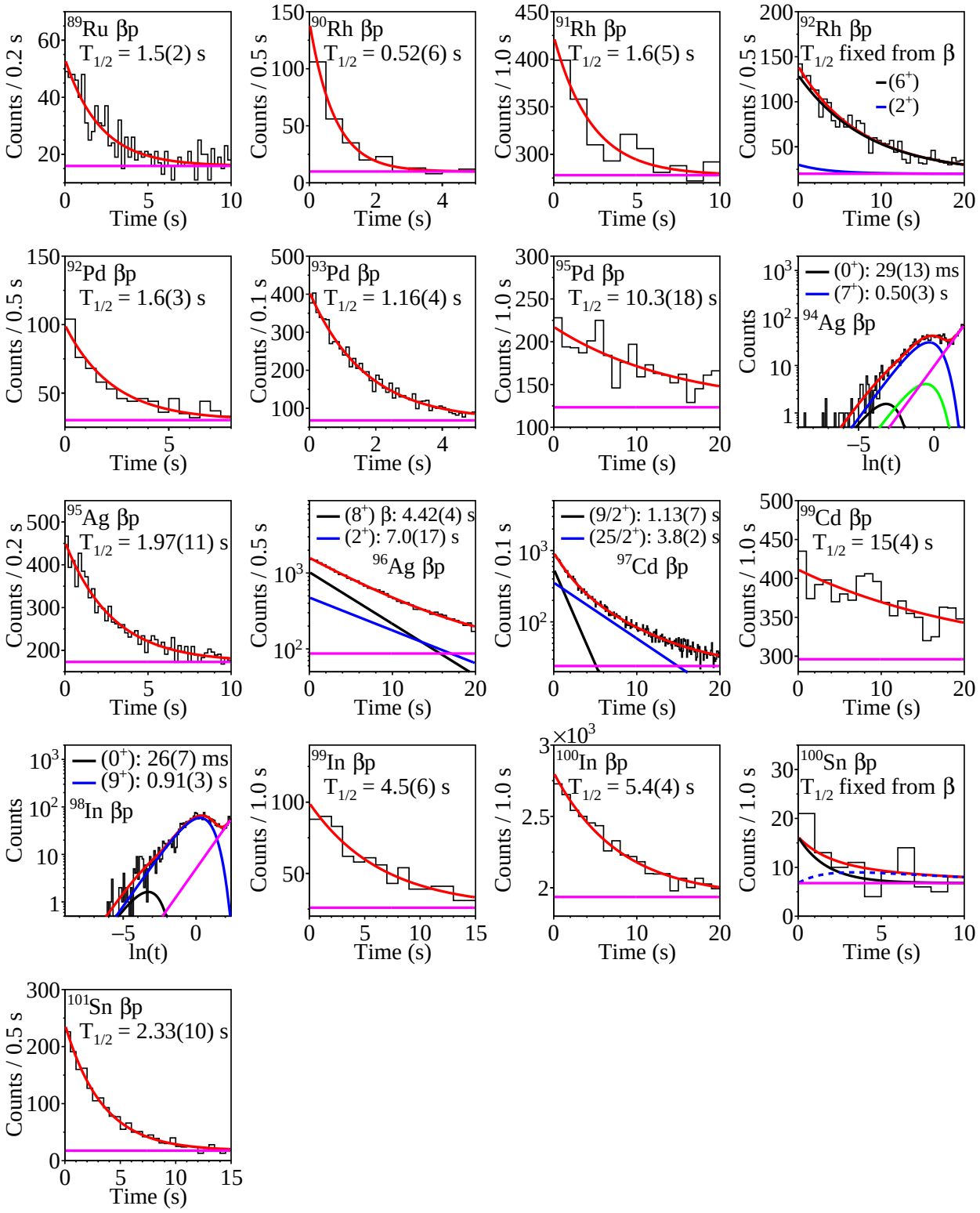

Figure 4.16: Time distribution of βp decays of isotopes and isomeric states. For ^{94}Ag and ^{98}In, the time distributions were plotted and fitted in the same way as shown in Fig. 4.10. The amplitudes of the parent decay components were used to calculate $b_{\beta p}$. For several states/isotopes, the $T_{1/2}$ values from β decays were adopted to determine $b_{\beta p}$.

Table 4.5: Half-lives and βp branching ratios of isotopes with non-negligible $b_{\beta p}$. Unless adopted from β-decay measurements, the half-lives determined from βp events were compared to the β-decay half-lives for consistency checks. The $b_{\beta p}$ values are compared to those from literature [2].

Nucleus	J^π	$T_{1/2}$ (s)		$b_{\beta p}$ (%)	
		β	βp	This work	Literature
^{89}Ru	$(9/2^+)$	1.32(6)	1.5(2)	2.4(3)	3.1(18)
^{90m}Rh	(7^+)	0.52(2)	0.52(6)	5.2(4)	
^{91}Rh	$(9/2^+)$	1.59(10)	1.6(5)	0.65(13)	1.3(5)
^{92}Rh	(6^+)	5.81(12)		1.3(3)	1.9(1)
^{92m}Rh	(2^+)	2.54(44)		12(11)	
^{91}Pd	$(7/2^+)$	0.037(4)	$0.031(^{+0.019}_{-0.009})$	$1.7(^{+0.9}_{-0.7})$	
^{92}Pd	0^+	1.17(4)	1.6(3)	1.7(3)	
^{93}Pd	$(9/2^+)$	1.14(3)	1.16(4)	5.3(1)	7.5(5)
^{95m}Pd	$(21/2^+)$	12.9(4)	10.3(18)	0.60(16)	0.93(15)
^{94}Ag	(0^+)	0.0277(15)	0.029(13)	1.3(6)	
^{94m}Ag	(7^+)	0.51(3)	0.50(3)	6.8(4)	20
^{95}Ag	$(9/2^+)$	1.81(7)	1.97(11)	2.6(1)	2.5(3)
^{96}Ag	(8^+)	4.42(4)		1.9(14)	6.9(7)
^{96m}Ag	(2^+)	5.6(6)	7.0(17)	12.3(50)	15.1(26)
^{95}Cd	$(9/2^+)$	0.031(3)	$0.051(^{+0.022}_{-0.012})$	$2.2(^{+0.9}_{-0.7})$	
^{96m}Cd	(16^+)	0.65(6)	$0.59(^{+0.12}_{-0.07})$	9.0(23)	5.5(40)
^{97}Cd	$(9/2^+)$	1.20(7)	1.13(7)	6.2(8)	11.8(20)
^{97m}Cd	$(25/2^+)$	3.7(1)	3.8(2)	21.6(24)	25(4)
^{99}Cd	$(5/2^+)$	18.7(11)	15(4)	0.16(3)	0.21(8)
^{97}In	$(9/2^+)$	0.026(4)	$0.004(^{+0.010}_{-0.002})$	$0.6(^{+0.8}_{-0.5})$	
^{98}In	(0^+)	0.0290(12)	0.026(7)	0.9(5)	5.6(3)
^{98m}In	(9^+)	1.11(9)	0.91(3)	24.2(11)	19(2)
^{99}In	$(9/2^+)$	3.35(11)	4.5(6)	0.6(2)	0.9(4)
^{100}In	(6^+)	5.56(5)	5.4(4)	1.59(7)	1.64(24)
^{99}Sn	$(9/2^+)$	0.027(5)	$0.011(^{+0.011}_{-0.004})$	$5.2(^{+3.9}_{-2.6})$	
^{100}Sn	0^+	1.19(10)		0.9(3)	< 17
^{101}Sn	$(7/2^+)$	2.09(18)	2.33(10)	18.4(8)	21.0(7)
					19.6(1) [18]

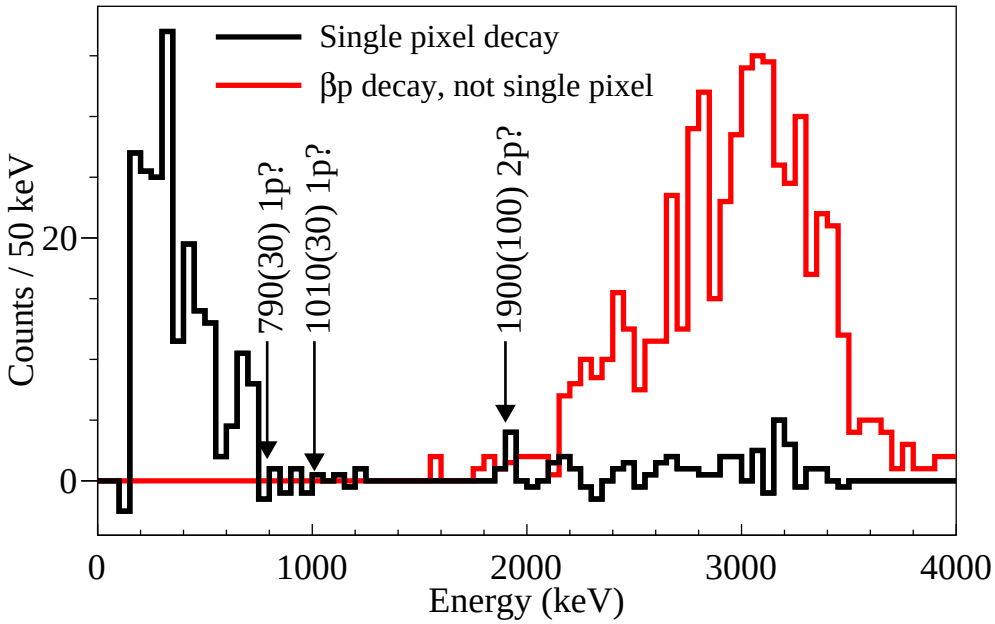

Figure 4.17: WAS3ABi energy spectrum following ^{94}Ag decay with background subtraction. For clarity, a minimum of 1500 keV was required for βp decays. Previously reported Q_p values [10, 11] are marked. The observation of 5 events at 1900 keV is discussed in the text.

at 790 and 1010 keV each. Consequently, it was impossible to confirm direct proton emission in ^{94}Ag from this experiment.

4.4 γ-ray spectroscopy following β and βp decays

γ-ray spectra and related analysis results from several selected nuclei's β and βp decays are presented, including those mentioned in Section 1.2.1 for which no literature exists for β-delayed γ rays. The significance of each finding is discussed mostly in the context of the SM calculations.

4.4.1 Low-spin structure of ^{90}Ru and the spin of ^{90m}Rh

The excited states of ^{90}Ru were populated from the β-decay of the $N = Z = 45$ nucleus ^{90m}Rh. The resulting γ-ray spectrum is shown in Fig. 4.18. Besides the known transitions obtained from a fusion-evaporation experiment [113], two new transitions at 1164 and 1316 keV were discovered. Relative intensities of the 886, 1164, and 1316-keV γ rays (normalized to the 738-keV γ ray) were 42(9)%, 21(6)% and 23(6)%, respectively. Based on the intensity analysis, these new γ-ray transitions feed the yrast (4^+) state and the three proposed (6^+) states are reproduced in the theoretical calculations as shown in Fig. 4.19. In order to determine the feeding of the (8^+) state which decays by a 512-keV γ ray, the intensity of the 511-keV annihilation peak was analyzed. After subtracting the contributions from superallowed Fermi decays, decays to the three (6^+) states and

^{90}Ru β decays, it was found that the feeding of the (8^+) was less than 6% at the 2σ confidence level.

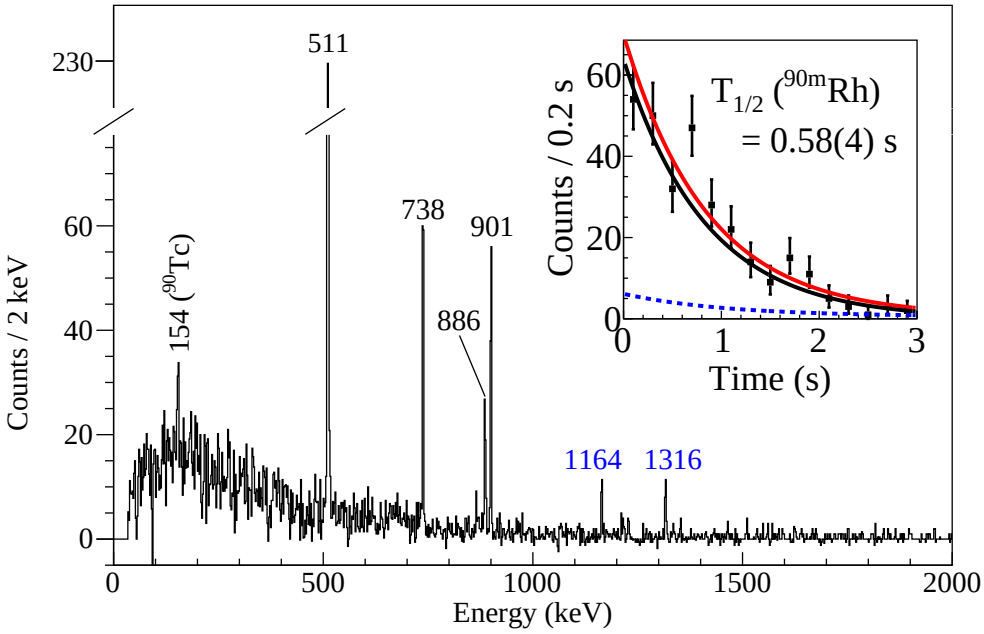

Figure 4.18: γ-ray spectrum of ^{90}Rh decay within the decay correlation time window of 3 seconds. Two new transitions were found at 1164 and 1316 keV. The inset shows the half-life of the isomeric state obtained with the labeled γ-ray gates, which is consistent with 0.52(2) s listed in Table 4.3.

The derived structure of ^{90}Ru and the β-decay feeding supports the assignment of $J^\pi_m = (7^+)$ for ^{90m}Rh, as it is predicted from the SM calculations with an excitation energy of 500 keV. This decay scheme resembles the GT-decay of ^{94}Ag's (7^+) isomer [52], which also feeds three (6^+) states.

4.4.2 Low-spin structure of ^{92}Rh

The low-spin structure of the daughter nucleus ^{92}Rh was investigated with the γ rays following ^{92}Pd's β decay. As seen in Fig. 4.20, only one γ ray at 257 keV belongs to ^{92}Rh, as the 865-keV γ ray is the (2^+) state energy of the granddaughter nucleus ^{92}Ru as previous reported in Ref. [114]. The 257-keV γ ray is understood from the spin selection rules of a GT decay as the transition populating the (2^+) isomer rather than the (6^+) ground state of ^{92}Rh; Fig. 4.21 shows the SM calculations which reveals a low-lying 1^+ state, and the excitation energy is experimentally confirmed as 257 keV above the (2^+) state.

Given the 100% population of ^{92m}Rh from the decay chain of ^{92}Pd, the β-decay time profile with the 865-keV γ-ray gate was used to determine the half-life of ^{92m}Rh. The input value of $T_{1/2}(^{92}\text{Pd}) = 1.17(4)$ s was varied at 2σ, and the resulting systematic uncertainties were included in the overall uncertainty. The $T_{1/2}$ obtained with this method ($T_{1/2} = 2.54(44)$ s) is vastly different from $T_{1/2} = 0.53(37)$ s deduced from the overall ^{92}Rh β-decay half-life analysis in Ref. [114].

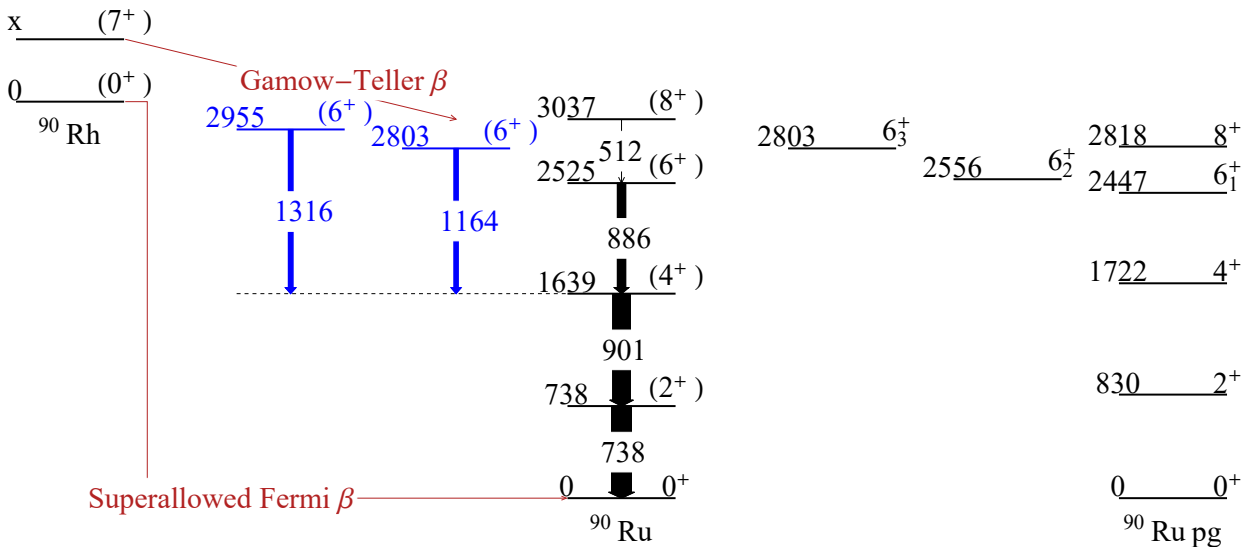

Figure 4.19: Level scheme of ^{90}Ru obtained from the β-decay of ^{90m}Rh. The widths of the arrows indicate relative γ-ray intensities. The two new proposed (6^+) states built by the 1164- and 1316-keV transitions are in agreement with the calculated 6^+ states shown in "^{90}Ru pg".

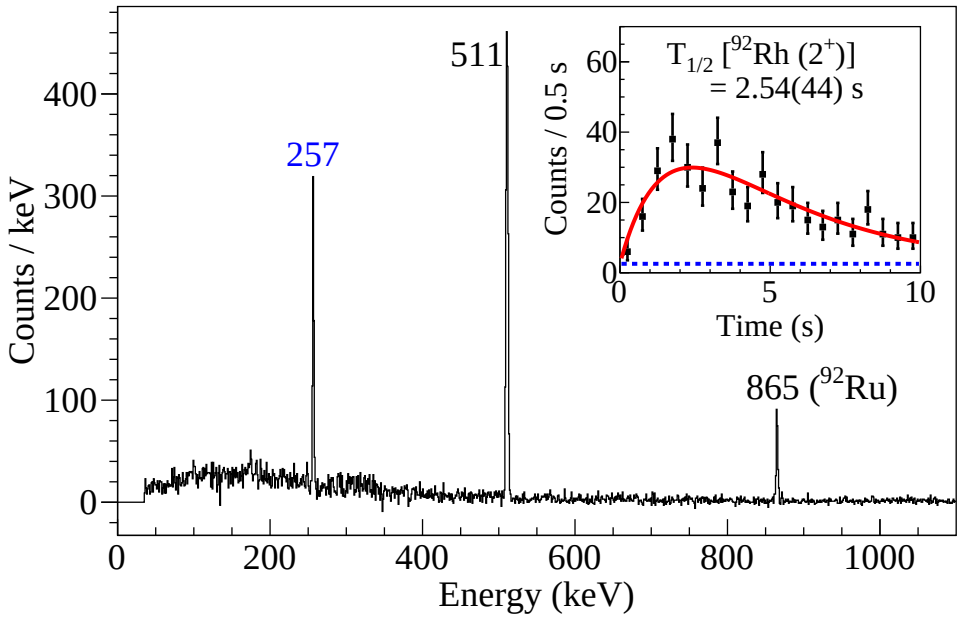

Figure 4.20: γ-ray spectrum following ^{92}Pd decay within 5 s of ion-β correlation. Only the 257-keV transition is attributed to the ^{92}Rh daughter nucleus, and it populates the (2^+) isomeric state. The inset shows the half-life determination of ^{92m}Rh using the time profile of the 865-keV γ ray in the granddaughter nucleus ^{92}Ru.

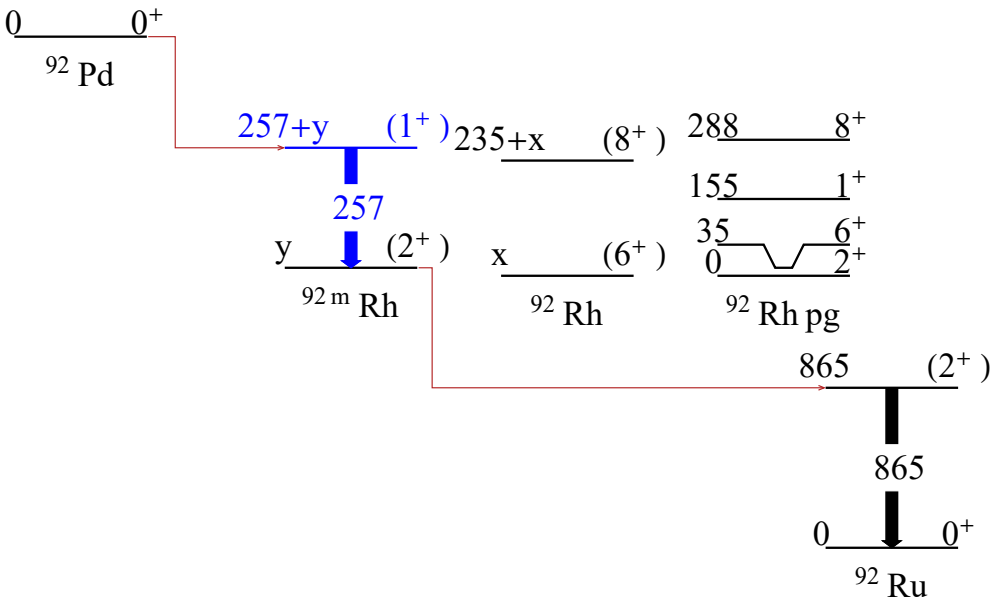

Figure 4.21: Schematic diagram of the ^{92}Pd-^{92m}Rh decay chain, with the interpretation of the newly discovered 257-keV γ ray being the $(1^+) \rightarrow (2^+)$ transition. The experimental low-energy states of ^{92}Rh are reproduced in the SM calculations labeled "^{92}Rh pg".

Another intriguing result is the comparison of the γ-ray intensities. In comparison to the 511-keV annihilation γ ray, relative intensities of 59(4)% and 40(3)% were obtained for the 257-keV and 865-keV γ rays in a correlation time window of 5 s. The ratios of the intensities were consistent with the cumulative distribution calculation using the two half-lives and the finite time range. The sum of relative intensities being consistent with 100% suggests very pure GT decays of both ^{92}Pd and ^{92m}Rh (apart from βp emission) with no direct population of the ground states - in conflict with the literature value of 77(23)% β-decay branch to the ground state of ^{92}Ru from ^{92m}Rh [114]. The current experimental results are better supported by the β-decay selection rules.

4.4.3 β, βp-delayed γ rays of ^{96}Cd

The abundance of ^{96}Cd isotopes produced in this experiment has enabled a more careful examination of the structure of the daughter nuclei. Of the β-delayed γ rays shown in Fig. 4.22, six transitions were discovered at 489, 843, 1146, 1569, 3177, and 3691 keV. The relative intensities of these γ rays compared to the 421-keV γ ray ranged from 5 to 11%. From the βp-delayed γ rays shown in Fig. 4.23, transitions from high-spin states of ^{95}Pd determined from a fusion-evaporation experiment [12] are clearly visible. Thus there is now experimental evidence for βp decays from the (16^+) isomer of ^{96}Cd. The 681-keV transition, which depopulates the $33/2^+$ state in ^{95}Pd, is most likely a 680-keV γ ray from ^{95}Rh which was populated by the βp decay of ^{96}Ag (see a different time profile of this γ ray in Fig. 4.23).

The known γ-ray transitions from both β and βp decays serve as further experimental evidence

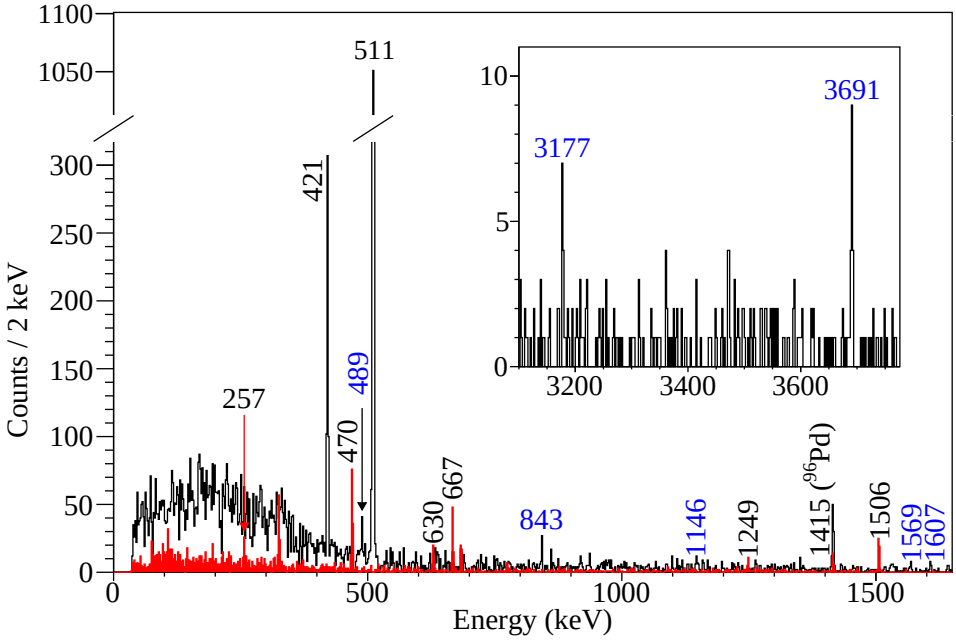

Figure 4.22: γ rays following β decay of ^{96}Cd. The black histogram corresponds to promptly emitted γ rays assigned to the ground-state decay of ^{96}Cd, and the red histogram shows delayed γ rays emitted from the (15^+) isomer of ^{96}Ag populated by the β-decay of ^{96}Cd's (16^+) isomer.

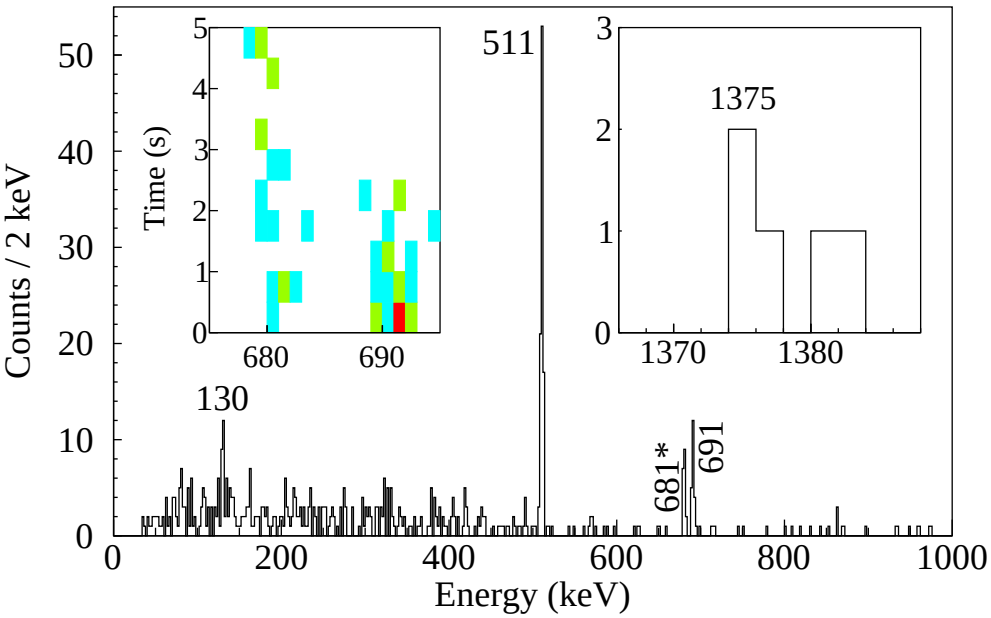

Figure 4.23: γ rays following βp decay of ^{96}Cd, where the labeled transitions are known from the high-spin structure of ^{95}Pd [12]. The left inset shows the time profile of the 681-keV transition, which shows a contamination of the 680-keV γ ray emitted after ^{96}Ag's βp decay into ^{95}Rh.

of the (16^+) spin-gap isomer of ^{96}Cd, the excitation energy of which could be determined with γ-gated Q_β analysis. On the other hand, the new transitions are assumed to originate from the decays of 1^+ states populated by the ground-state decay of ^{96}Cd; the half-life analysis result on these γ rays was more consistent with $T_{1/2}$(g.s.) = 1.08(9) s than the isomer half-life of 0.65(6) s. The calculated level scheme shown in Fig. 4.24 reveals excited 1^+ states up to 3.7 MeV in the *pg* model space (no core excitations), which could accommodate γ-ray energies up to 3691 keV.

The apparent fragmentation of the ground-state β-decay branch injects a systematic uncertainty on the Q_β of ^{96}Cd, as one or more of these transitions could be in coincidence with the 421-keV γ ray used as the selection cut for the Q_β analysis. The sum of the intensities of the six new γ rays is about half of the intensity of the 421-keV γ ray. More statistics would allow a $\gamma\gamma$ coincidence analysis of these transitions to address this issue and develop the low-spin structure of ^{96}Ag to be compared with calculations.

4.4.4 Identification of negative-parity states in ^{97}Cd and ^{97}Ag

While β-delayed γ-ray spectroscopy has been performed for ^{97}Cd revealing the $(25/2^+)$ isomer and is decay scheme [53], there have been predictions of a $(1/2^-)$ isomeric state for this nucleus [13, 63] which could be investigated with γ-ray transitions. In this work, three new transitions at 1245, 1418 and 1673 keV were found as shown in Fig. 4.25. The half-life associated with these γ rays, was 0.78(7) s, which differs from the ground-state half-life of 1.20(7) s by at least 5σ; therefore these transitions were attributed to the decay of the predicted $(1/2^-)$ isomer in ^{97}Cd into three $(3/2^-)$ states in ^{97}Ag.

Schmidt et al. [13] note that ^{97}Cd lies outside of the region of nuclei used in the fitting procedure to obtain empirical single-particle energies and two-body matrix elements by Refs. [27, 115, 116], which leads to large variances in the calculated properties of negative-parity states and their decays. One set of calculations appears to agree well with experimental results, which is elaborated here. Calculations by Ogawa [63] using the interaction derived by Gross and Frenkel [116] suggest the $1/2^-$ isomer to be approximately 800 keV above the ground state with a dominant GT-decay branch over the $M4$ transition. The predicted half-life of this isomer was 0.65 s, which is quite consistent with the experimental value. The scenario of at least one γ ray emitted after the GT decay is possible if J_f^π of the β decay is $3/2^-$. SM calculations were done to include the $f_{5/2}$ and $p_{3/2}$ orbitals in addition to the *pg* model space, since the latter could generate only one $3/2^-$ state in ^{97}Ag. The calculation outputs are displayed in Fig. 4.26 for comparison with experimental data. Calculations show three $3/2^-$ states with energy spacings consistent within 250 keV compared to experimental γ-ray energies, with a small branching ratio to the intermediate $5/2^-$ state. Better statistics would lead to a more definitive structure of low-spin, negative-parity states in both ^{97}Cd and ^{97}Ag, and even obtain decay information about the $(1/2^-)$ state in ^{97}Ag.

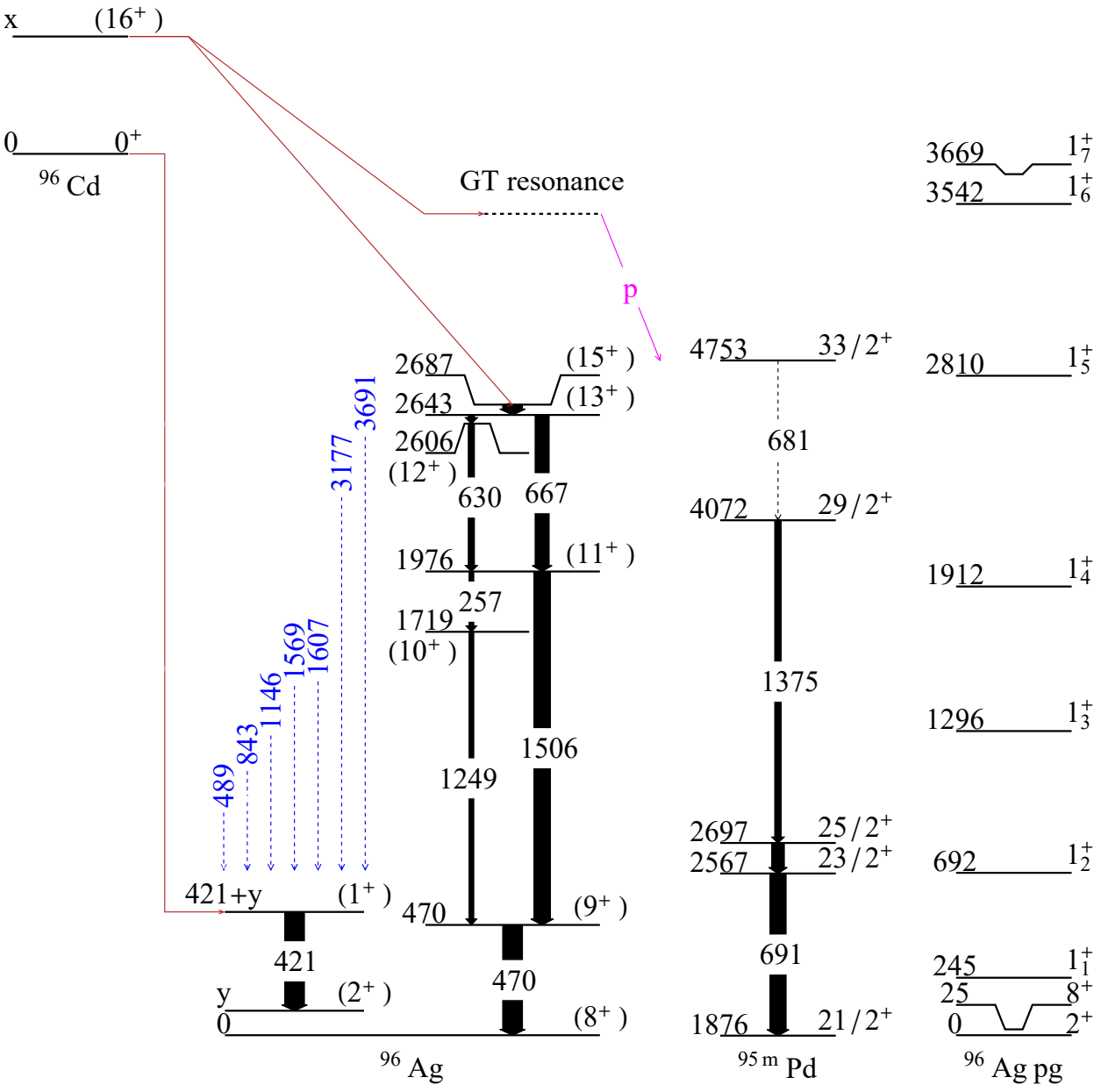

Figure 4.24: Level schemes of ^{96}Ag and ^{95}Pd reproduced from the $\beta/\beta p$ decay of ^{96}Cd. It is unclear whether the βp decay populates the $33/2^+$ state in ^{95}Pd. SM calculations of 1^+ states in ^{96}Ag are shown on the right, in relation to the discovered but unassigned γ rays (dashed blue arrows, compressed energy scale).

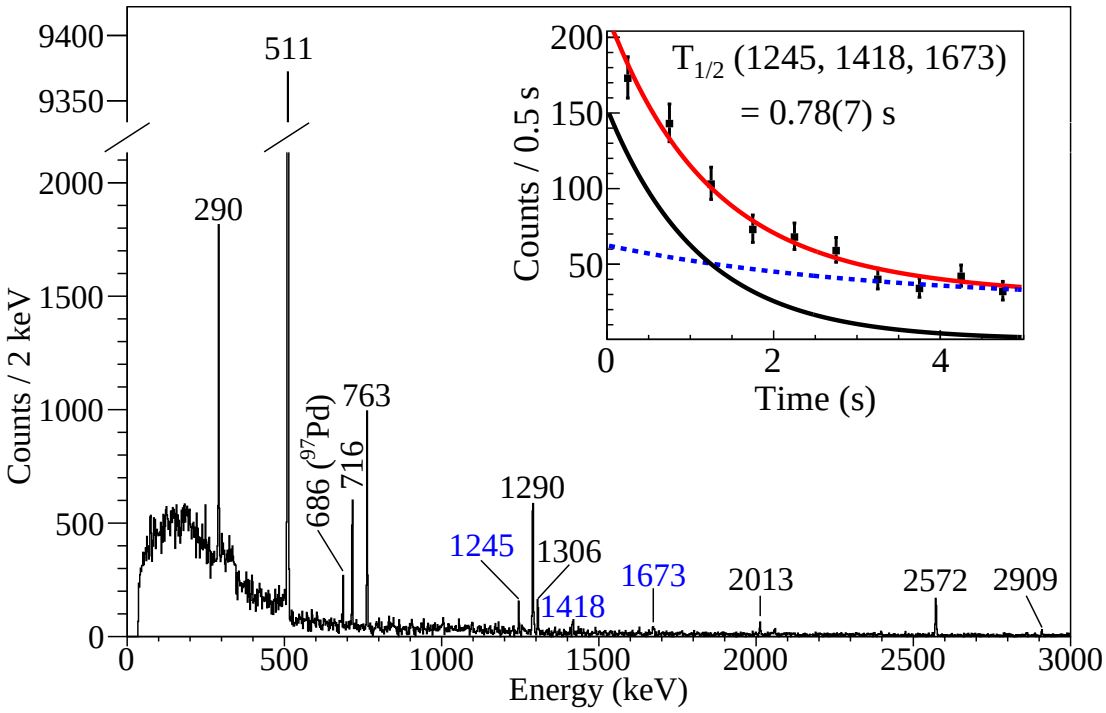

Figure 4.25: γ-ray spectrum following ^{97}Cd decay. Three new transitions at 1245, 1418 and 1673 keV are reported, and the β-decay time profile of these γ rays exhibits a half-life of 0.78(7) s. This half-life is incompatible with both the ground state and the isomeric state half-lives, but agrees well with the predicted $T_{1/2} = 0.65$ s for the $(1/2^-)$ isomer [13].

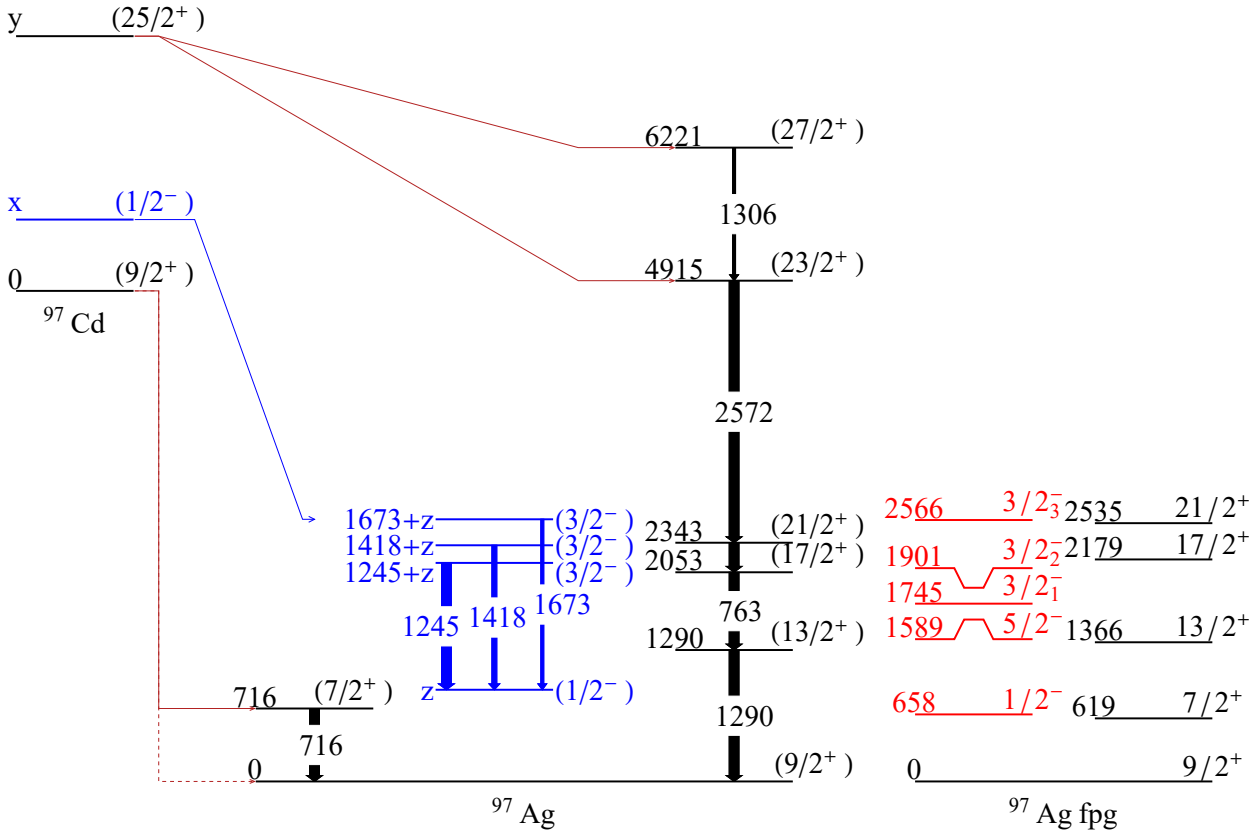

Figure 4.26: Level scheme of ^{97}Ag obtained from the β-decay of ^{97}Cd. The 1245-, 1418- and 1673-keV γ rays are considered to depopulate three $(3/2^-)$ states in ^{97}Ag after the β decay of ^{97}Cd's $(1/2^-)$ isomer, in view of the SM calculations of low-energy states performed in the *fpg* model space shown on the right.

4.4.5 β, βp-delayed γ rays of ^{98m}In

β-delayed γ rays of the (9^+) isomer of ^{98}In into the excited states of ^{98}Cd were analyzed. If the spin of the isomer is correct, then allowed GT β decays would populate states with spins between 8^+ and 10^+. Indeed, the known γ-ray cascade from the (8^+) seniority isomer in ^{98}Cd was observed with equal intensities. Furthermore, three counts were observed in an energy window of 4153-4160 keV, which corresponds to the 4157-keV γ-ray energy from the core-excited (10^+) state to the (8^+) isomer [64]. The β-decay half-life extracted from these events was $0.7^{+0.9}_{-0.2}$ s, consistent with $T_{1/2} = 1.11(9)$ s as exhibited in Fig. 4.10. From $\gamma\gamma$ coincidence analysis, one coincidence event was observed at 147 and 198 keV each. From the intensity analysis, β feeding to the (10^+) was calculated to be $4.9^{+4.5}_{-2.9}$%.

In addition, the γ rays were from βp decays were analyzed. As shown in Fig. 4.27, the dominant transitions at 290, 763, and 1290 keV were previously reported as part of the main seniority scheme of ^{97}Ag in Ref. [117]. In addition, new transitions were found at the following energies: 281, 602, 729, and 1417 keV. A βp decay from the (9^+) state with $l = 0$ leads to final states with spins between $15/2^+$ and $21/2^+$, and the new γ rays could be arranged in the way exhibited in Fig. 4.27 to form a separate γ-ray cascade from the $15/2^+$ state in ^{97}Ag. The energies of the two proposed states are in great agreement with the SM calculations of $11/2^+$ and $15/2^+$ states and their branching ratios. The 281-keV γ ray emitted with the βp decay may be depopulating a first-excited $9/2^+$ state (shown in Fig. 4.28) into either the $(11/2^+)$ or the $(13/2^+)$ state, but the calculations suggest a dominant, high-energy decay branch to the ground state of ^{97}Ag; therefore it was left unassigned. A second-excited $9/2^+$ state is predicted to lie between the $(17/2^+)$ and the $(21/2^+)$ states, but βp feeding to this state is expected to be much suppressed due to the centrifugal barrier. $\gamma\gamma$ coincidence results with higher statistics will allow a firm placement of this γ ray.

4.4.6 Low-spin structure of ^{99}Cd

The β-delayed γ rays from ^{99}In decays provide experimental information on the low-spin states of $N = 51$ nucleus ^{99}Cd. As seen in Fig. 4.29, nine new γ rays are assigned to the ^{99}Cd with a combined decay time profile that is fully consistent with the ground state half-life of ^{99}In. $\gamma\gamma$ coincidence relations and relative intensities of the labeled γ rays is found in Table 4.6. Assignment of the new transitions to the current level scheme on ^{99}Cd built on fusion-evaporation data [118] is presented in Fig. 4.30, using the *gds* model space to predict the single-particle states above the $N = 50$ shell.

The construction of the level scheme of ^{99}Cd was complicated by limited $\gamma\gamma$ coincidence information and the abundance of low-spin states generated by a neutron above the $N = 50$ shell. Theoretical calculations report 48 distinct states with J^π from $5/2^+$ to $13/2^+$ with $E_x < 4.6$ MeV. Thus the theoretical level scheme on the right of Fig. 4.30 was built by identifying the states with dominant decay branches to single final states, assuming that the GT decay from ^{99}In's $(9/2^+)$ ground state populates the ^{99}Cd daughter states with spins between $7/2^+$ and $11/2^+$. The agreement with the experimental γ-ray energies is mixed; while the transitions satisfying the experimental

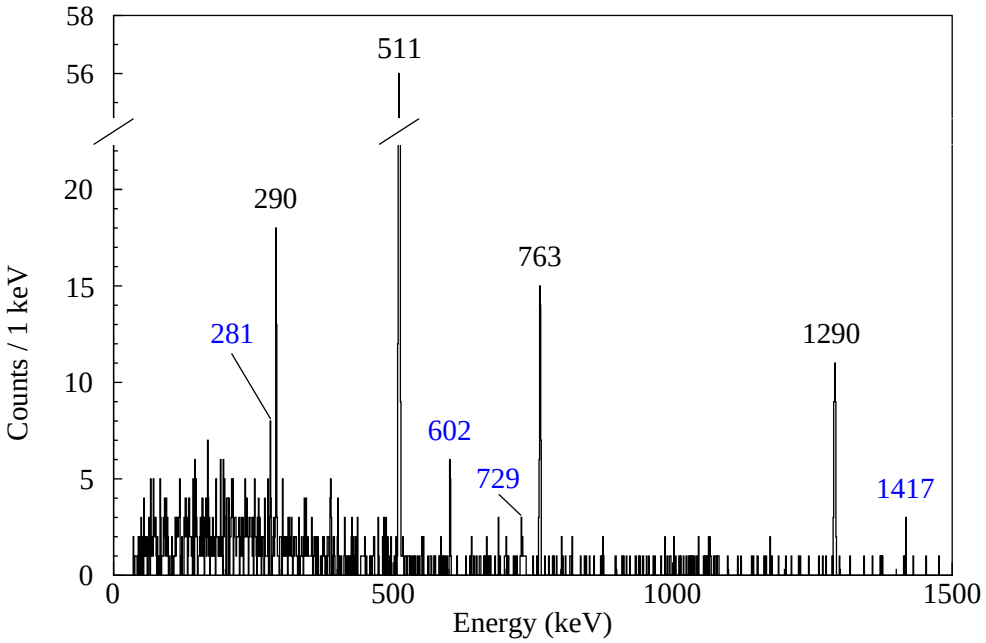

Figure 4.27: γ-ray spectrum following ^{98}In's βp decay. Three intense transitions at 290, 763 and 1290 keV are known to belong to the γ-ray cascade in ^{97}Ag, with the highest spin being $(21/2^+)$. The assignment of the new γ rays in ^{97}Ag is discussed in the text.

Table 4.6: γ-ray energies, coincidences and relative intensities following ^{99}In β decay, where the relative intensities were normalized to the sum of the two yrast transitions 441 keV and 1224 keV. Newly observed γ-ray energies are given in parentheses.

E_γ (keV)	Coincidences	I_{rel} (%)
(371)	607, 1224, (1473)	6.5(26)
441	1234, (1340), (1534), (1786), (1986)	59(3)
607	1224, (1473)	23(2)
783		5.4(20)
(1078)		6.5(26)
1224	607, (1473), (1596)	41(3)
1234	441	18(3)
(1340)	441	5.7(23)
(1473)	(371), 607, 1224, 1234	8.3(17)
(1534)	441	8.1(18)
(1596)	1224	3.8(17)
(1607)		4.4(13)
(1786)	441, (1986)	2.8(13)
(1986)	441, (1786)	8.0(14)

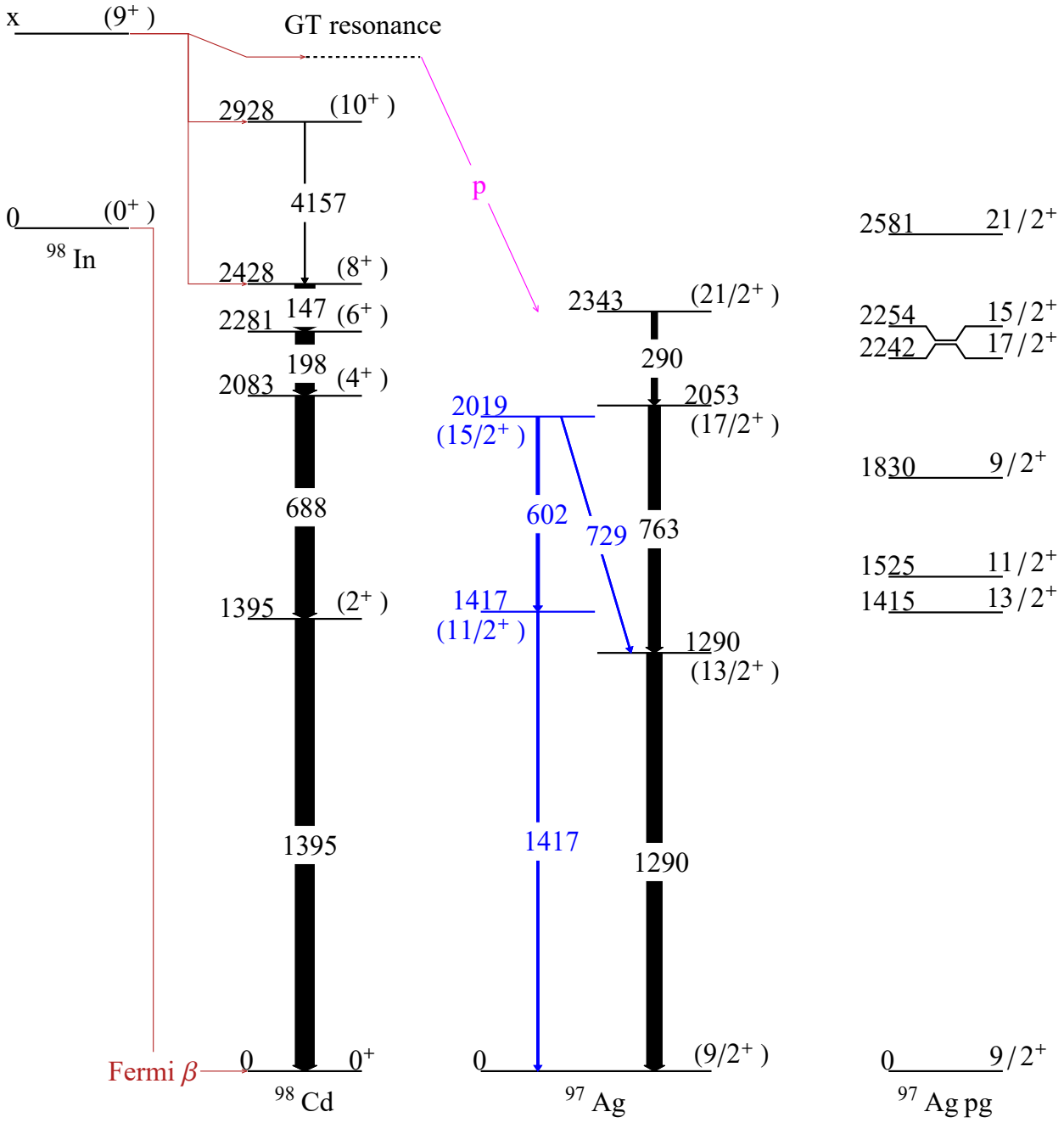

Figure 4.28: Level schemes of ^{98}Cd and ^{97}Ag reproduced from the $\beta/\beta p$ decay of ^{98m}In. The three new γ rays correspond to the transitions from the proposed $(15/2^+)$ and $(11/2^+)$ states in ^{97}Ag, which are reproduced in the calculations.

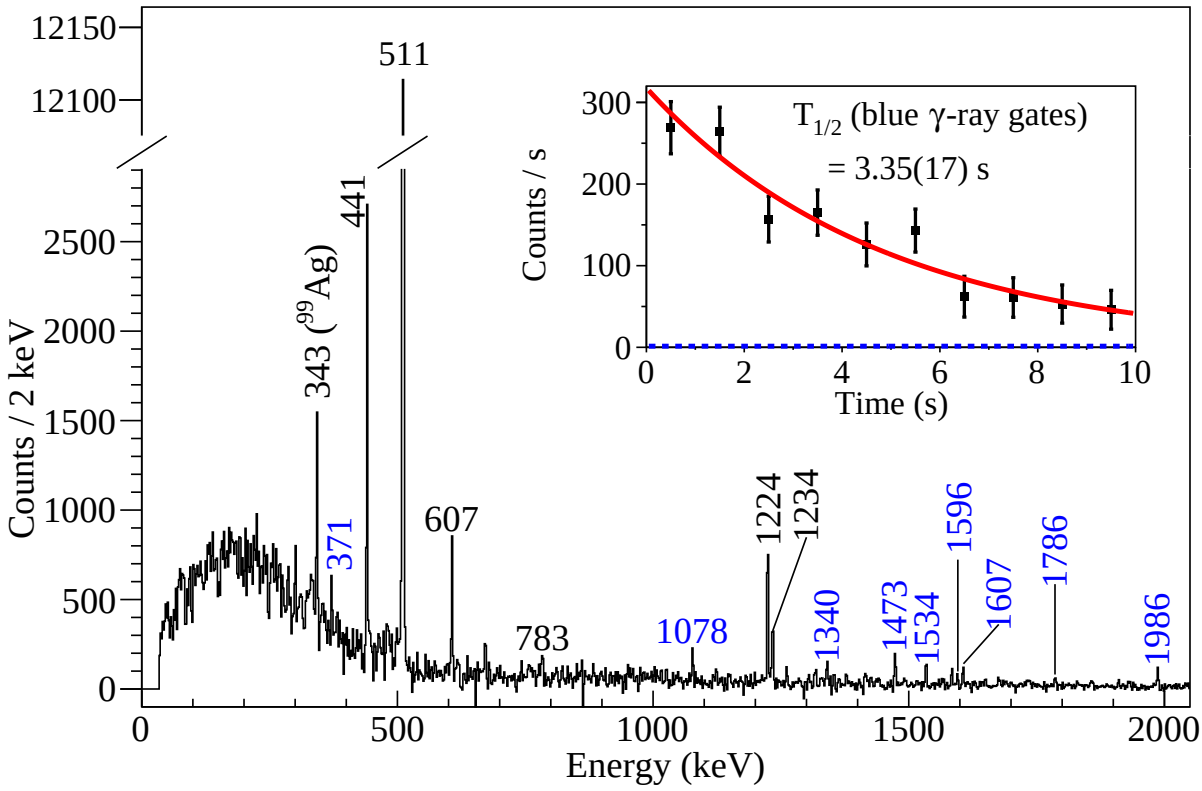

Figure 4.29: γ-ray spectrum following ^{99}In decay. Besides the known transitions in ^{99}Cd (black labels), many new but weak transitions are present (blue labels). The half-life determined from the blue γ-ray gates are fully consistent with $T_{1/2} = 3.35(11)$ s determined from the overall β-decay fit.

$\gamma\gamma$ coincidence relationships could be found, the deviation increased as a function of the excitation energy. In addition, the 1473-371 keV cascade could not account for the whole relative intensity of the 607-keV γ ray from the $13/2^+$ state, which would not be directly populated by β decay; additional feeding to this state is required. A more robust dataset would identify the level scheme of ^{99}Cd, which can solidify the understanding of the SPEs and the TBMEs in the $g_{7/2}, d_{5/2}, d_{3/2}$, and $s_{1/2}$ orbitals across the shell closure.

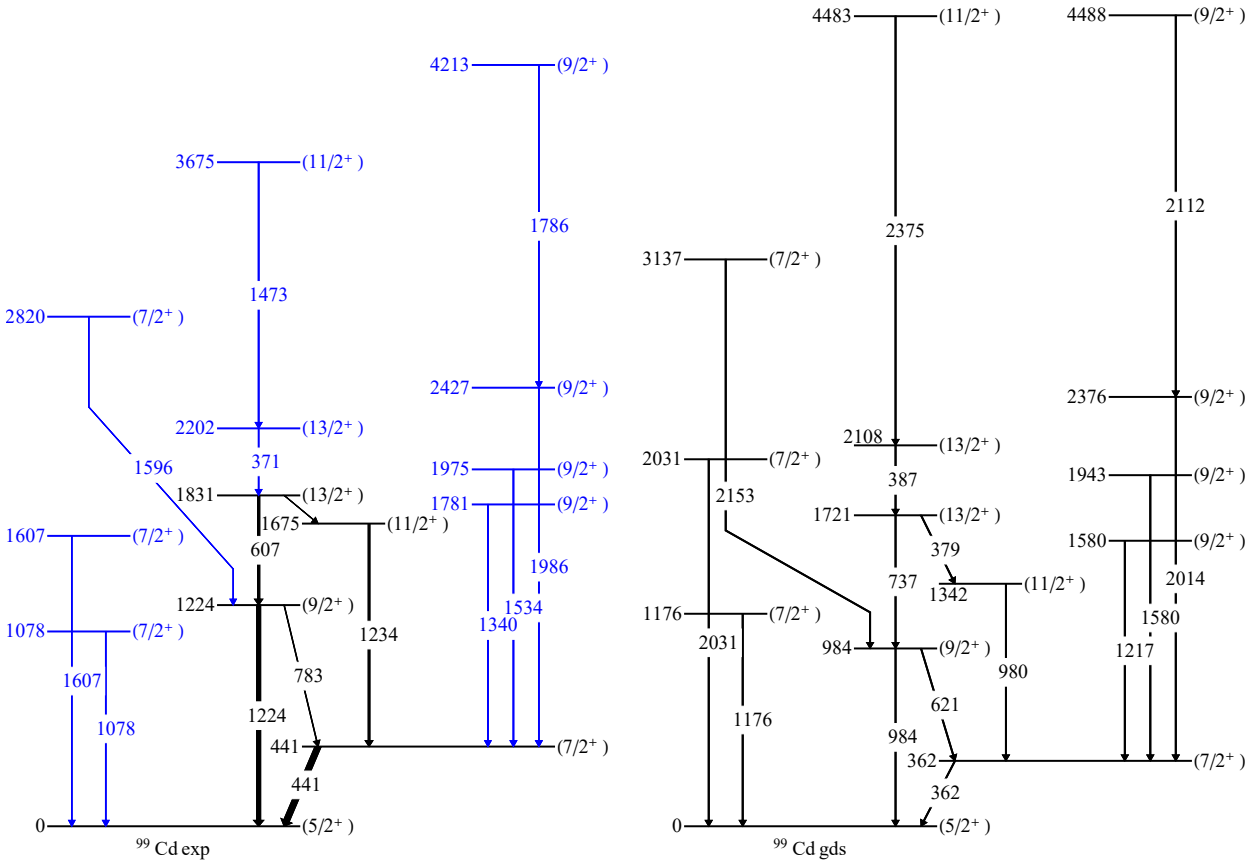

Figure 4.30: Proposed level scheme of ^{99}Cd with $J^+ \leq 13/2$ from the β-delayed γ rays of ^{99}In. A calculated level scheme resembling the experimental results is drawn on the right for comparison.

4.4.7 Structure of ^{100}In, and ^{100}Sn's log(ft) and B_{GT} values

One of the key objectives of the experiment was to construct an unambiguous level scheme of ^{100}In, in order to determine the properties of the superallowed GT decay of ^{100}Sn accurately. A detailed investigation of the GT decay of ^{100}Sn from same dataset presented in this thesis was the central aspect of an independent parallel analysis by D. Lubos [69]; therefore a comprehensive discussion of the results was not carried out here. The β-delayed γ ray spectrum following ^{100}Sn is displayed in Fig. 4.31, with the absolute intensities of the known transitions.

The half-life of ^{100}Sn was determined with the MLH method from ^{100}In's γ-ray gates, yielding

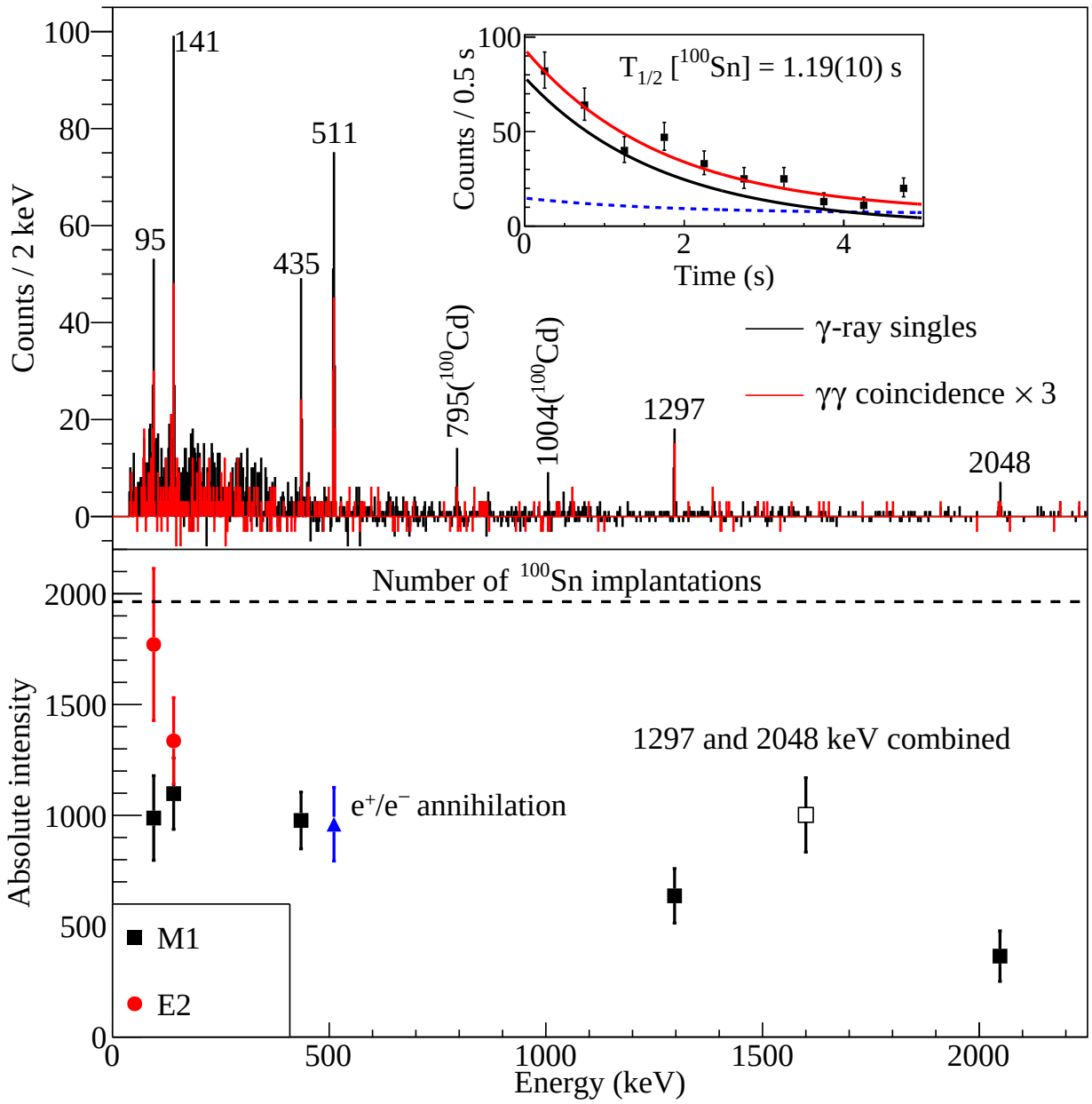

Figure 4.31: Top: single and coincidence γ-ray spectra following ^{100}Sn β decay within 5 s after implantation. No new γ ray has been found in comparison to Ref. [14], but the inset shows a more precise half-life determined from ^{100}In's γ-ray gates. Bottom: absolute intensities of the γ rays belonging to ^{100}In and the annihilation events. In comparison to other γ-ray intensities, both 95- and 141-keV γ rays are likely $M1$ transitions.

a value of 1.19(10) s. This result is consistent with $T_{1/2} = 1.16(20)$ s reported by Hinke et al. [14], and is more precise. $\gamma\gamma$ coincidence relations were established among the 95/141/435/1297-keV γ rays, and one coincidence event of a 96-2048 $\gamma\gamma$ pair was found. Unfortunately, the total coincidence projections built by gating on all of the γ rays in ^{100}In (red bins of Fig. 4.31) did not reveal a new transition. However, the intensity analysis has addressed certain questions. First, both the 95- and 141-keV transitions are likely $M1$ transitions; this was expected and assumed in the literature. Second, the intensities of the 1297 and 2048 keV suggest a parallel branch which feeds a common excited state that hosts a cascade of the low-energy transitions. Two level schemes of ^{100}In proposed in the frameworks of Coraggio [15], and Stone and Walters [16] are drawn with experimental γ-ray energies in Fig. 4.32. Each level scheme is discussed below, in view of the experimental information.

The "Coraggio" [15] level scheme on the left of Fig. 4.32 proposes an isomeric 2^+ state just above the 6^+ ground state, and places the 2048-keV as a side branch. Since the sum of the 95-141-435-1297 keV γ-ray energies is 1968 keV, the missing γ-ray energy must be at least 80 keV to ensure that the ground state of ^{100}In is 6^+ as suggested by experimental data. There are three main objections: first, the energy of the 2^+ isomer is too low compared to 482 keV predicted by the SM calculation in the *gds* model space. Second, the isolation of the 2048-keV transition forces an agreement in intensity between the 1297 keV and the three low-energy γ rays in Fig. 4.31; the 1297-keV γ ray is weaker in intensity by approximately 2σ. Third, the minimum energy requirement of the missing transition raises the expected detection counts significantly, but the data shows no new γ ray.

The "Stone and Walters" [16] level scheme, drawn in the middle of Fig. 4.32 also places the 2048-keV γ ray in parallel with the 1297 keV, but the rest is more sophisticated. The yrast states form a decay cascade of 95-141-435 keV with an unknown energy y, and the 2^+ state populated by the 1297-keV γ ray has three unobserved γ-ray branches; their energies are 751, $\sim$1000, and 1186 keV. The validity of this level scheme depends heavily on the detection of the missing γ-ray energies, and the best agreement with the experimental intensities of the known γ rays can be achieved if the 751-keV transition is the only decay branch. However, there were no counts within ± 2 keV of the 751-keV and the 1186-keV peaks in Fig. 4.31. In the search of an intermediate γ-ray energy, the most prominent peak was found at 1040 keV with 6 counts - more than 3σ lower in intensity than the 1297-keV γ ray with 26(5) counts.

The third alternative is to suggest a second β-decay branch to another 1^+ state. Most of the γ-ray information provided in Fig. 4.31 is satisfied by the level scheme on the right of Fig. 4.32, with emphasis on resolving the relative intensities of the detected γ rays. The non-detection of a low-energy $5^+ \rightarrow 6^+$ γ ray is still assumed. The main contention for this level scheme is the population of two different 1^+ states. This would be reflected by distinct Q_β values, and the centroid of the Q_β distribution gated on the 2048-keV γ ray is lower than those produced from other γ-ray gates (see Fig. 4.33). However, due to large uncertainties it is not a strong evidence for two 1^+ states. Theoretically, the possibility of an energy difference of $2048 - 1297 = 751$ keV between the two 1^+

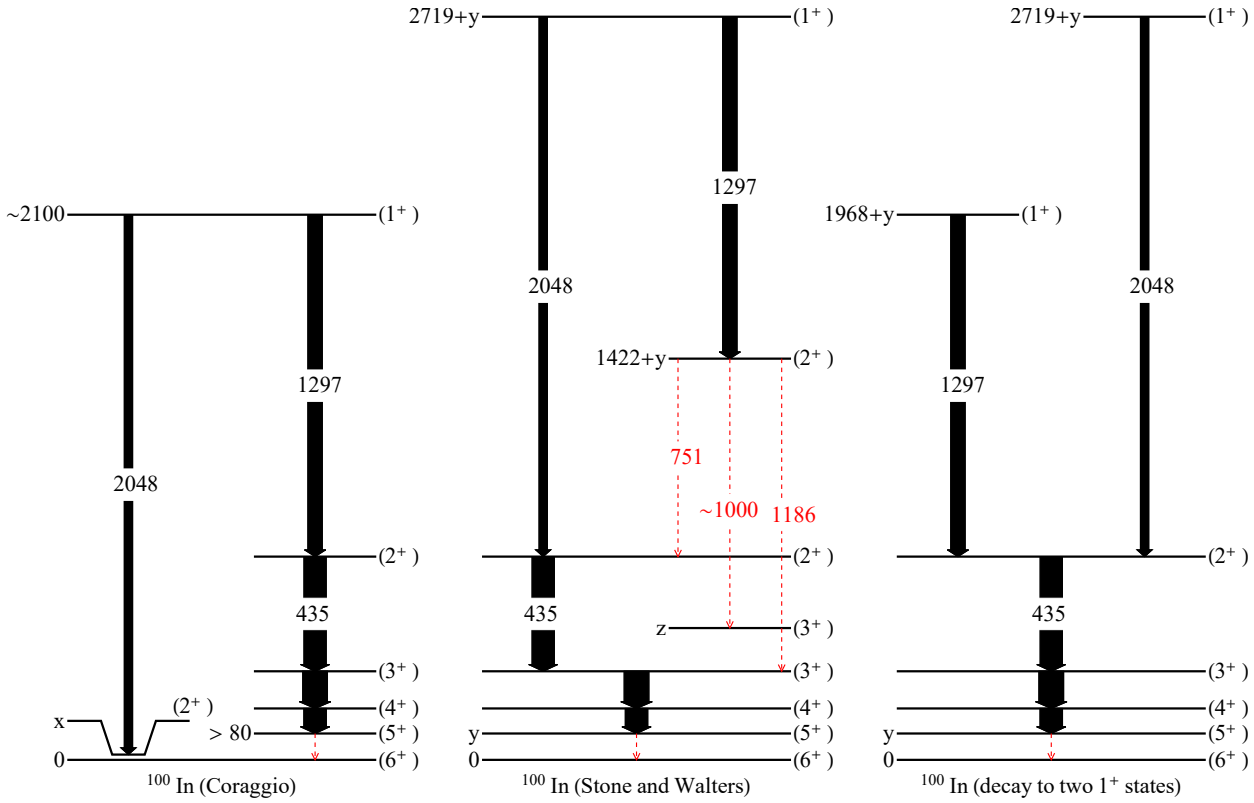

Figure 4.32: Level schemes of ^{100}In constructed from experimental results in the theoretical frameworks of two works: by Coraggio [15] and by Stone and Walters [16]. The dashed arrows and energy labels in red indicate predicted but experimentally unobserved γ rays. The level scheme on the right assumes a fragmentation of the β-decay branch into two final (1^+) states, which satisfies the experimental results but requires a very unlikely breakdown of the $Z = 50$ shells.

states is very low. During the β decay, a proton from the $g_{9/2}$ orbital below the $Z = 50$ shell gap is converted into a neutron in the $g_{7/2}$ orbital above the $N = 50$ shell gap; a hypothetical, second proton hole-neutron particle combination resulting in $J^{\pi} = 1^{+}$ is only possible for a $\pi g_{7/2}$ or a $\pi d_{5/2}$ proton above the magic number 50 coupled to the $\nu g_{7/2}$ neutron. In the current SM, promoting a $g_{9/2}$ proton across the $Z = 50$ shell requires at least 4 MeV in excitation energy. Thus, bringing down the second 1^{+} state to within 1 MeV of the yrast 1^{+} state in ^{100}In requires a severe quenching of the $Z = 50$ shell gap. This is contradicted by the agreement between the experimental B_{GT} value and the theoretical calculations of the large scale shell model (LSSM) that assumes a robust ^{100}Sn core. The LSSM calculations are described in the Supplementary Information of Ref. [14].

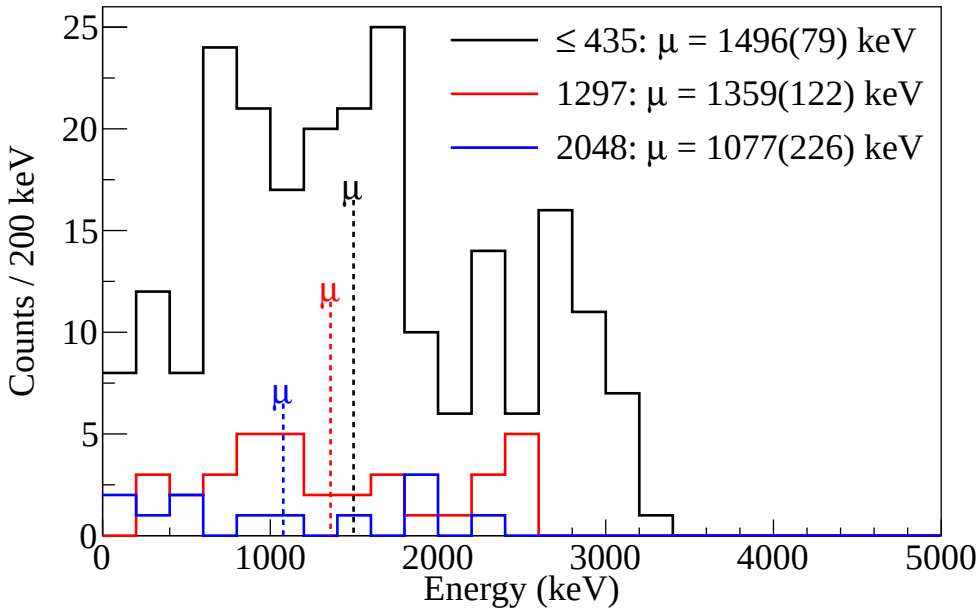

Figure 4.33: Positron energy spectra of ^{100}Sn β decays for different γ-ray gates, and their centroid energies. A lower but not inconsistent centroid value is observed for the Q_{β} spectrum obtained by gating on the 2048-keV γ ray.

Of the first two proposed level schemes of ^{100}In, neither one satisfies the experimental results completely. Considering the mass predictions for ^{100}Sn, subtracting the Q_{β} and the 1.022-MeV annihilation energy from Q_{EC} results in E_x ranging from 2158 keV from AME2012 [112] to 2968 keV from HFB27 [111]. Both level schemes' (1^{+}) energies fall close to these values. If the Q_{EC} value and the excitation energy were scaled by identical energies, the $\log(ft)$ and the B_{GT} values remain identical. Thus a single $\log(ft)$ and B_{GT} value was evaluated, including the assumption of the lowest excited state energy being at most 100 keV. A systematic uncertainty of this value was added to the calculations, yielding $\log(ft) = 3.01(12)$ and $B_{GT} = 3.7(10)$. The $\log(ft)$ value has increased from the value of $2.62^{+0.13}_{-0.11}$ [14] but remains as the smallest in all of the known β decays. The B_{GT} value has decreased significantly from $9.1^{+2.6}_{-3.0}$, owing to the greater Q_{β} evaluated in Fig. 4.13. The $\log(ft)$ and B_{GT} values agree with the empirically extrapolated values of $\log(ft)$

= 2.87(5) and B_{GT} = 5.21(60) [119] within 2σ. The experimental B_{GT} value also agrees with $B_{GT} = 5.68$ received by the yrast 1^+ state in ^{100}In from LSSM calculations.

For the level scheme on the right with two β-decay branches, the branching ratios/log(ft) values of the two 1^+ states based on relative γ-ray intensities are 63(11)%/3.21(14) and 37(11)%/3.06(19) for the 1297- and 2048-keV transitions, respectively. The partial B_{GT} values and their sum are 2.4(4) + 3.3(10) = 5.7(11). Herein lies another problem for this level scheme: the B_{GT} value is higher for the non-yrast 1^+ state, which is strongly contradicted by the LSSM calculation that predicts 69% of the total B_{GT} carried by the yrast 1^+ state.

4.4.8 Low-spin structure of ^{101}In and the ground-state spin of ^{101}Sn

The ground state spin of the $Z = 50, N = 51$ nucleus ^{101}Sn and the structure of the β-decay daughter nucleus ^{101}In was investigated with β-delayed γ rays. As mentioned in Section 1.3.4, the ground state spin of ^{101}Sn has been a controversial topic. The $\nu g_{7/2}$ orbital above the $N = 50$ shell gap is expected to lie close in energy with the $\nu d_{5/2}$ orbital, but multiple works [66, 67, 120] have differed on the order of the two orbitals.

One of the ways to determine the ground state spin of ^{101}Sn was an analysis of the βp data. However, the results obtained in this experiment was similar in statistics and quality compared to the results discussed in the thesis work by K. Straub [18], which did not yield a definitive statement on the spin of ^{101}Sn. An alternative approach via the β-delayed γ-ray data analysis is thus presented here. As shown in Fig. 4.34, five γ rays have been found. This work finds no evidence of 352-keV and 1065-keV transitions reported in Ref. [17]. γ rays at 1347, 1500, and 1508 keV were first observed and noted in Ref. [18], where the 352/1065-keV γ rays were also absent. However, no significant γ-ray intensities at 252, 1281, or 1332 keV were observed, as reported in Straub's work.

The decay branching ratios and log(ft) values calculated using the literature Q_{EC} value of 8.30(42) MeV are listed in Fig. 4.35, which also shows a comparison between the proposed level scheme and the SM results. The SPEs and TBMEs used for this SM calculation result in a $7/2^+$ ground state for ^{101}Sn with a 52-keV energy difference to the yrast $5/2^+$ state. When taking into account some energy scaling, the first three lowest-energy transitions are in agreement with the levels with spins $5/2^+$, $7/2^+$, and $9/2^+$ from the SM calculations. Decay branches from these states to the yrast $11/2^+$ state are expected to be small; the transition energies to the ground state are much larger than to the $11/2^+$, and the multipolarities of the transitions do not hinder their decays to the ground state of ^{101}In. Based on the level spacing, the 1347-keV γ ray was assigned to depopulate the first $(7/2^+)$ state. Being nearly degenerate, the assignment of the state spins for the 1500- and 1508-keV γ rays was left ambiguous between either a $(5/2^+)$ or a $(9/2^+)$ state. In this energy range, the number of available states for β-decay feeding matches the number of γ rays if the ground-state spin of ^{101}Sn is $7/2^+$.

For the two higher-energy γ rays discovered in this work, the SM predicts three near-degenerate states with spins between $5/2^+$ and $9/2^+$. Here, it is more feasible to suggest $5/2^+$ as the ground-state spin of ^{101}Sn as the β-decay branch to the third $9/2^+$ will be heavily suppressed. The number

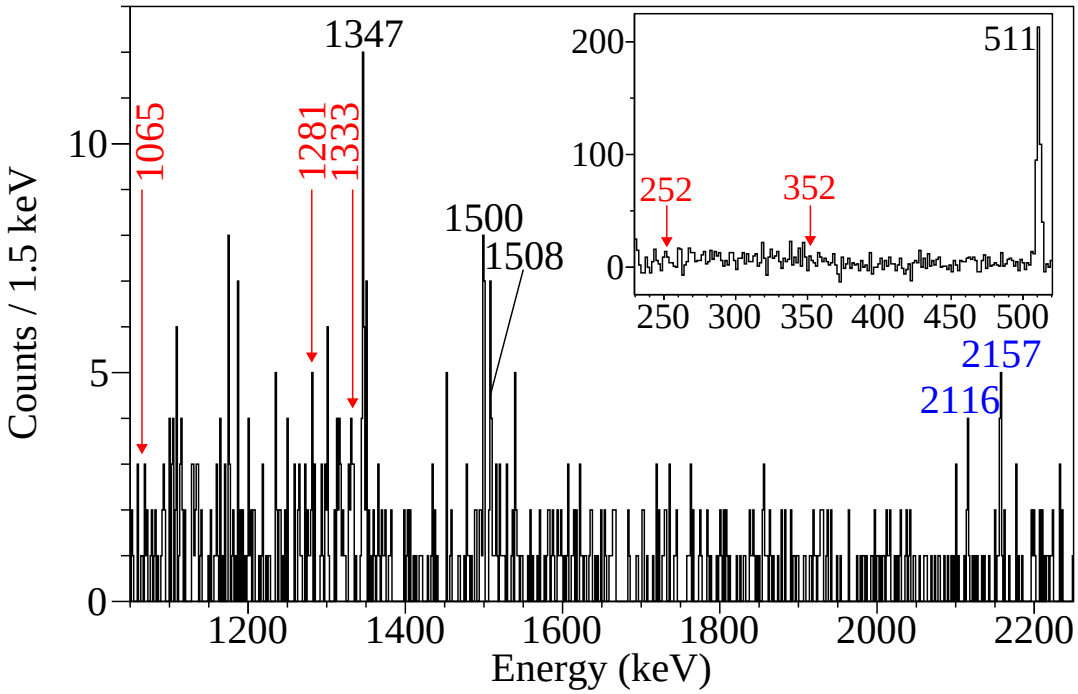

Figure 4.34: γ-ray spectrum following ^{101}Sn β decay. The inset shows the amplitude of the 511-keV γ-ray peak, which is a relevant information in determining the ground-state spin of ^{101}Sn. Red energy labels indicate unobserved γ-ray transitions that have been previously reported in Refs. [17, 18].

of γ rays then matches the number of states fed by β decays. However, the probability that at least one transition was unobserved is rather high due to the lack of statistics caused by a small β-decay branch and a lower EURICA efficiency.

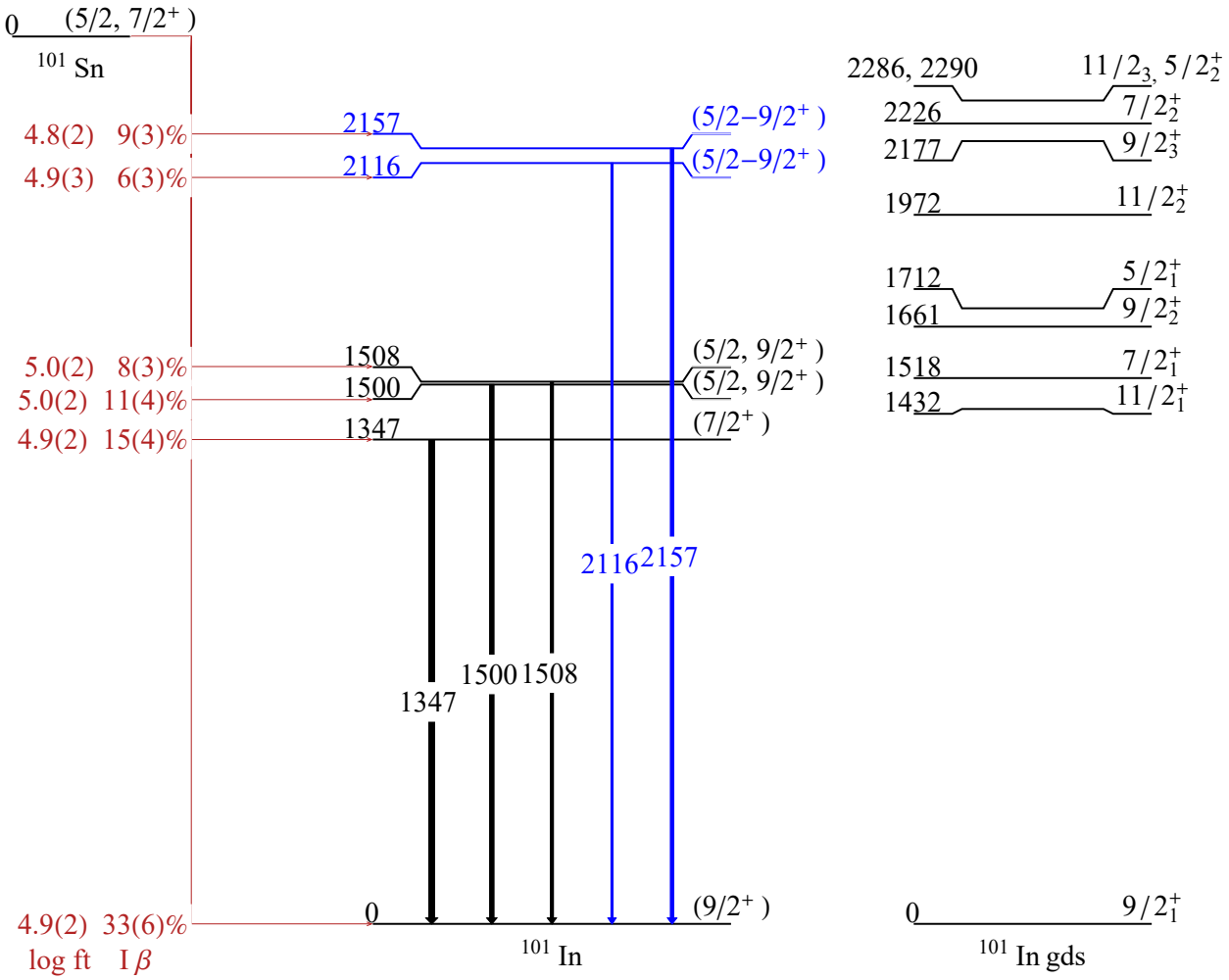

Figure 4.35: Level scheme of ^{101}In deduced from the observed β-delayed γ rays in Fig. 4.34 and the predicted states from the SM calculations in the *gds* model space. Beside each experimentally deduced excited states, β-decay branching ratios and corresponding log(ft) values are listed - all of which suggest allowed GT decays ($\Delta J \leq 1$).

One item of note is the significant β-decay branch to the ground state of ^{101}In determined from the analysis of the 511-keV γ-ray intensity. From the spin selection rules of the GT decay, β decays from a $5/2^+$ state to a $9/2^+$ state are forbidden. However, the log(ft) value of the ground-state to ground-state decay is typical of a $\Delta J = 1$ and parity-conserving transition, which is the decisive evidence for the ground-state spin of ^{101}Sn being $7/2^+$. If this supposition is true, then ^{101}Sn's ground state becomes rather unique; even-Z, $N = 51$ isotones from Mo to Cd isotopes have $J^\pi = 5/2^+$ as the ground state, which is also true for odd-A Sn isotopes from $A = 103$ to 109. The inversion of the order of the two states occurs in ^{111}Sn [121]. The order of the near-degenerate $g_{7/2}$

and $d_{5/2}$ orbitals for ^{101}Sn is a sensitive probe of the strength of the two-body tensor force [68] which supports the $(7/2^+)$ ground-state assignment. From the tensor force effects, the repulsion between the negative-parity $h_{11/2}$ orbital and the positive-parity $g_{7/2}$ orbital causes the lowering of the $g_{7/2}$ orbital below the $d_{5/2}$ orbital in ^{101}Sn.

Chapter 5

Summary and outlook

The decay spectroscopy experiment on ^{100}Sn and nuclei in its vicinity has yielded many new and intriguing results. Many of these results are consistent with theoretical predictions, but several of them have raised new questions. International efforts to investigate these isotopes in greater detail in the future are mentioned.

5.1 Highlights of the results and implications

A summary of the results and discussions in Chapter 4 is reiterated here.

5.1.1 Isomer γ-ray spectroscopy and isomeric ratios

Half-lives of many isomers decaying by γ-ray emission were measured with consistent results compared to literature values. In addition, new half-life and energy measurements of several isomers in ^{95,96}Ag and ^{98}Cd led to new transition strengths that were consistent with theoretical calculations. The sharp cutoff model was relatively successful in reproducing the relative isomeric ratios of both the γ-decaying isomers and β-decaying isomers, and its deficiencies were reasonably explained by the structure effects. No isomeric states were found in ^{100}Sn, and the decay properties of its hypothetical (6^+) isomer were estimated: $E_\gamma > 140$ keV, and $T_{1/2} < 300$ ns.

In ^{96}Cd, a cascade of 8 new γ-ray transitions were found to be emitted from a single isomeric state with $T_{1/2} = 199(26)$ ns. The γ-ray energies could be conveniently arranged to be consistent with the energy gaps of the excited states predicted by SM calculations in the *pg* and the *gds* model spaces. Based on the range estimate of the electromagnetic transition strength, the multipolarity of the isomeric transition was postulated to be $E1$. The spin and parity this isomer is likely to be (13^-), but (12^-) is not completely ruled out. ^{96}Cd is now the heaviest even-even $N = Z$ nucleus with experimental information on its excited states, whose SPEs may be relevant for determining the wavefunction of the ground state of ^{100}Sn.

5.1.2 β, βp spectroscopy of $N \sim Z \sim 50$ nuclei

Half-lives and Q_β values of $N \leq Z \leq 50$ nuclei were either measured for the first time, or with greater precision than literature values. The derived Q_{EC} values of these nuclei were generally lower than the predicted mass differences from various models. No model was able to predict all of the measured Q_{EC} values accurately. Furthermore, odd-odd $N = Z$ nuclei are more bound than

the theoretical predictions. In relation to the current estimates, the attractive $T = 1, T_z = 0$ pn interaction contribution to the ground state may be greater in magnitude.

Unlike other odd-Z, $N = Z - 1$ nuclei ^{89}Rh and ^{93}Ag, ^{97}In has been shown to decay primarily by β-decay. Nevertheless, circumstantial evidence for a near-degenerate proton-emitting isomeric state was also found. The spin of this isomer was postulated to be $(1/2^-)$, where overcoming the centrifugal barrier for proton emission is easier from the $p_{1/2}$ orbital ($l = 1$) than from the $g_{9/2}$ orbital ($l = 4$). The derived S_p (proton separation energy) values for the two states lie midway between -1.2 and 0 MeV, the range given by the different mass models.

5.1.3 $\beta/\beta p$-delayed γ-ray spectroscopy

Many new results obtained from γ rays following β and βp decays revealed the low-spin structure of nuclei around ^{100}Sn, complimenting the high-spin structure of such nuclei previously investigated by fusion-evaporation experiments.

The decay properties ^{90m}Rh were analyzed in detail with γ rays known to belong in ^{90}Ru. In addition, two newly observed γ rays are suggested to depopulate the non-yrast (6^+) states, reinforcing the theoretical prediction of the spin of the isomer being (7^+).

From the β decay of ^{92}Pd, the energy of the (1^+) state in ^{92}Rh was experimentally determined to be 257 keV above the (2^+) isomer. This was predicted by the SM with a ~ 100 keV energy difference. In addition, the half-life and the decay of ^{92m}Rh were better measured compared to literature.

The measured γ rays following β and βp decay of ^{96}Cd confirmed the previous level schemes of ^{96}Ag and ^{95}Pd, adding more evidence to the (16^+) isomer formed by the $T = 0$ pn interaction. Unlike ^{92}Pd, the β decay of the ground state of ^{96}Cd appears fragmented into multiple 1^+ states in ^{96}Ag, based on at least 7 new γ rays. More abundant γ ray statistics would be needed to verify the accuracy of the SM predictions of ^{96}Ag's low-spin states up to 4 MeV in excitation energy.

Three new γ rays have been measured from the β decay of ^{97}Cd, and they are attributed to the decay of the newly proposed $(1/2^-)$ isomer. This makes ^{97}Cd a unique nucleus exhibiting both the spin-aligned isoscalar pn isomer and the spin-gap isomer formed by the excitation of a proton in the $p_{1/2}$ orbital. The γ-ray energies are consistent with the excitation energies of predicted $(3/2^-)$ states relative to the $1/2^-$ state in ^{97}Ag, and the half-life of ^{97}Cd's $(1/2^-)$ isomer agreed well with a theoretical prediction. While these results reinforce the robustness of the SM in the ^{100}Sn region, the excitation energy of the isomer and the properties of the $1/2^-$ state in ^{97}Ag need to be known to establish a solid understanding of negative-parity states in the nuclei around ^{100}Sn.

Evidence for the spin of ^{98m}In formed by the pn hole pair being (9^+) was found with a γ-ray cascade of the well-known seniority level scheme in ^{98}Cd. In addition, signatures for this isomer's β decay into ^{98}Cd's core-excited (10^+) state was also found. From new measurements of βp-delayed γ rays of the (9^+) isomer, two states with spins $(15/2^+)$ and $(11/2^+)$ in ^{97}Ag were revealed. The energies and the decay branches of these states are well reproduced in the SM.

Many new γ rays were discovered from the β decay of ^{99}In into the $N = 51$ nucleus ^{99}Cd,

yielding a glimpse of many daughter states with expected spins from $7/2^+$ to $11/2^+$. Limited $\gamma\gamma$ coincidence relations of the weak transitions were used to establish a tentative level scheme up to 5 MeV in excitation energy, but the disagreement with SM calculations of level energies was up to 1 MeV. Sufficient statistics will be necessary to solidify the low-spin states of ^{99}Cd and perform sensitive tests of the single-particle energies of the neutron orbitals across the $N = 50$ shell for proton-rich nuclei.

Despite higher statistics compared to any previous ^{100}Sn experiment, the level scheme of ^{100}In remains undetermined. The intensities of the two highest-energy transitions suggest two parallel γ-ray decay branches, which ultimately feed a common state for the three low-energy γ rays. However, the non-observation of γ rays predicted by the SM and LSSM calculations has made the agreement between the experimental γ-ray spectrum and the proposed level schemes inconclusive. On the other hand, proposing two close-lying 1^+ states to resolve the non-observation of new γ rays is only possible if the $Z = 50$ shell is heavily quenched to allow less than 1 MeV excitations into the $g_{7/2}$ and $d_{5/2}$ orbitals. Based on the properties of nuclei and their decays studied in the SM framework, such an extreme breakdown of the $Z = 50$ shell is quite unreasonable. The experimental B_{GT} value of the superallowed GT decay of ^{100}Sn was determined to be 3.7(10) assuming a 100% β-decay branch to the yrast (1^+) state in ^{100}Sn, consistent with the experimental extrapolation and the LSSM calculations assuming robust $N = Z = 50$ shell closures for ^{100}Sn. The interpretation of the GT decay of ^{100}Sn and the structure of ^{100}In still depend on sensitive measurements of both the γ-ray data and β energies, requiring even higher statistics to address the discrepancy between theoretical and experimental results.

The analysis of the β-delayed γ rays of ^{101}Sn suggest its ground state spin to be ($7/2^+$) rather than ($5/2^+$), which implies the lowering of the neutron $g_{7/2}$ orbital below the $d_{5/2}$ for this nucleus. The primary basis of this argument lies with a 33(6)% direct β-decay branch to the ($9/2^+$) ground state of ^{101}In, deduced from the γ-ray intensity of the 511-keV annihilation peak. The number of other γ rays attributed to ^{101}In is also more compatible with the ($7/2^+$) assignment, where SM calculations offer more available states with spins between ($5/2^+$) and ($9/2^+$). This spin assignment is supported by the prediction of two-body tensor forces [68]. The spin of ^{101}Sn's ground state can be further solidified by determining the exact low-spin structure of ^{101}In with higher γ-ray statistics.

5.2 Prospective experiments in the ^{100}Sn region

EURICA has been operational at RIKEN for 5 years for many decay spectroscopy experiment campaigns, but it has been relocated back to GSI. Hypothetically, a full EURICA array (about twice the γ-ray singles efficiency) combined with the current primary beam intensity of ^{124}Xe being 100 pnA (5 times more than this experiment) raises the amount of γ-ray statistics by an order of magnitude, and approximately 20 times the $\gamma\gamma$ coincidence statistics. Two major potential setbacks would be the diminishing returns from high implantation rates (increased background decay correlations and deadtime losses), and the available beam time for a decay spectroscopy

experiment in the ^{100}Sn region.

A total absorption spectroscopy (TAS) experiment for $N \sim Z \sim 50$ isotopes is being proposed by A. Algora [122] at RIKEN. One advantage of this setup is the ability to capture the full energies of β particles with large Q_β, which proved to be difficult with WAS3ABi. Improved precisions in Q_{EC} measurements of nuclei near the proton dripline are expected. However, the TAS experiment is better complemented with high-statistics γ-ray data with sufficient $\gamma\gamma$ coincidences as a foreknowledge of the daughter nuclei's structure and β-decay intensities.

An intermediate-energy Coulomb excitation of ^{102}Sn is being proposed by M. L. Cortés [123] at RIKEN. The primary objective of the experiment is to probe the evolution of the $B(E2; 0^+ \rightarrow 2^+)$ trend in the Sn isotopes towards ^{100}Sn, which yields a hint on the inertness of the $Z = 50$ core in ^{100}Sn. During the Coulomb excitation, Doppler-shifted γ rays from ^{102}Sn's yrast 2^+ state will be measured with NaI crystals. From simulations of the γ-ray spectrum, the Coulomb excitation cross section will be measured, which then can be translated into the $B(E2)$ value.

In the long term, GSI will be upgraded into FAIR (Facility for Antiproton and Ion Research) [124] with the DESPEC (DEcay SPECtroscopy) project [125, 126] in mind. In addition to meeting other major physics goals, FAIR will be capable of providing an intense beam of ^{100}Sn and nuclei in its vicinity with the identical fragmentation-separation method at RIBF. Similar to the EURICA-WAS3ABi setup but with better overall capabilities, DEGAS (DEspec Germanium Array Spectrometer) [127] and AIDA (Advanced Implantation Detector Array) are being developed. The higher kinetic energy of the radioactive isotopes produced at FAIR will enable a greater coverage of the implantation area for β-decay spectroscopy. On the other hand, FRIB (Facility for Rare Isotope Beams) [128, 129] at Michigan State University is under construction. The proton-rich nuclei produced from FRIB will be complemented with highly-efficient GRETA (Gamma-Ray Energy Tracking Array, which is the full 4π solid angle coverage version of GRETINA [130]) to study the in-flight decays of ^{100}Sn and nuclei near the proton dripline.

Bibliography

[1] T. Faestermann, M. Górska, and H. Grawe. *Prog. Part. Nucl. Phys.*, 69:85, 2013.

[2] G. Audi et al. *Chin. Phys. C*, 36:1157, 2012.

[3] R. Krücken. *Contemp. Phys.*, 52:101, 2011.

[4] H. Okuno, N. Fukunishi, and O. Kamigaito. *Prog. Theor. Exp. Phys.*, page 03C002, 2012.

[5] S. Nishimura. *Prog. Theor. Exp. Phys.*, page 03C006, 2012.

[6] J. Eberth et al. *Nucl. Phys. A*, 520:669c, 1990.

[7] Z. Y. Xu. PhD thesis, University of Tokyo, 2012.

[8] B. S. Nara Singh et al. *Phys. Rev. Lett.*, 107:172502, 2011.

[9] D. S. Delion, R. J. Liotta, and R. Wyss. *Phys. Rep.*, 424:113, 2006.

[10] I. Mukha et al. *Phys. Rev. Lett.*, 95:022501, 2005.

[11] I. Mukha et al. *Nature*, 439:298, 2006.

[12] R. Mărginean et al. *Phys. Rev. C*, 86:034339, 2012.

[13] K. Schmidt et al. *Nucl. Phys. A*, 624:185, 1997.

[14] C. B. Hinke et al. *Nature*, 486:341, 2012.

[15] L. Coraggio et al. *Phys. Rev. C*, 70:034310, 2004.

[16] C. A. Stone and W. B. Walters. *Hyperfine Interactions*, 22:363, 1985.

[17] O. Kavatsyuk et al. *Eur. Phys. J. A*, 31:319, 2007.

[18] K. Straub. PhD thesis, Technische Universität München, 2010.

[19] R. K. Wallace and S. E. Woosley. *Astrophys. J. Suppl.*, 45:389, 1981.

[20] R. B. Wiringa, V. G. J. Stoks, and R. Schiavilla. *Phys. Rev. C*, 51:38, 1995.

[21] S. Veerasamy and W. N. Polyzou. *Phys. Rev. C*, 84:034003, 2011.

[22] R. D. Woods and D. S. Saxon. *Phys. Rev.*, 95:577, 1954.

[23] O. Haxel, J. H. D. Jensen, and H. E. Suess. *Phys. Rev*, 75:1766, 1949.

[24] M. Göppert-Mayer. *Phys. Rev.*, 75:1969, 1949.

[25] M. Bender, P. H. Heenen, and P. G. Reinhard. *Rev. Mod. Phys.*, 75:121, 2003.

[26] D. Vretenar et al. *Phys. Rep.*, 409:101, 2005.

[27] F. J. D. Serduke, R. D. Lawson, and D. H. Gloeckner. *Nucl. Phys. A*, 256:45, 1976.

[28] H. Herndl and B. A. Brown. *Nucl. Phys. A*, 627:35, 1997.

[29] M. Honma et al. *Phys. Rev. C*, 80:064323, 2009.

[30] A. Lisetskiy et al. *Phys. Rev. C*, 70:044314, 2004.

[31] B. A. Brown and K. Rykaczewski. *Phys. Rev. C*, 50:2270(R), 1994.

[32] B. A. Brown et al. *Phys. Rev. C*, 71:044317, 2005.

[33] E. Caurier et al. *Rev. Mod. Phys.*, 75:427, 2005.

[34] E. Caurier and F. Nowacki. *Acta Phys. Polon. B*, 30:705, 1999.

[35] T. Mizusaki. *RIKEN Acc. Prog. Rep.*, 33:14, 2000.

[36] V. I. Isakov. *Phys. At. Nucl.*, 72:33, 2009.

[37] J. C. Hardy and I. S. Towner. *Phys. Rev. C*, 91:025501, 2015.

[38] B. Singh et al. *Nucl. Data Sheets*, 84:487, 1998.

[39] J. C. Hardy and I. S. Towner. *Phys. Rev. C*, 79:055502, 2009.

[40] J. D. Jackson, S. B. Treiman, and H. W. Jr. Wyld. *Phys. Rev.*, 106:517, 1957.

[41] M. Kobayashi and T. Maskawa. *Prog. Theo. Phys.*, 49:652, 1973.

[42] J. C. Hardy et al. *Phys. Lett. B*, 71:307, 1977.

[43] A. de Shalit and I. Talmi. *Nuclear Shell Theory.* Academic Press, New York and London, 1963.

[44] L. Meitner. *Z. Phys.*, 9:131, 1922.

[45] D. Bazin et al. *Phys. Rev. Lett.*, 101:252501, 2008.

[46] K. Sümmerer et al. *Nucl. Phys. A*, 616:341c, 1997.

[47] H. Grawe. Private communication, 2009.

[48] C. B. Hinke. PhD thesis, Technische Universität München, 2010.

[49] F. Nowacki. *Nucl. Phys. A*, 704:958, 2002.

[50] E. Caurier and F. Nowacki. Private communication, 2005.

[51] V. I. Isakov and K. I. Erokhina. *Phys. At. Nucl.*, 65:1431, 2002.

[52] C. Plettner et al. *Nucl. Phys. A*, 733:20, 2004.

[53] G. Lorusso et al. *Phys. Lett. B*, 699:141, 2011.

[54] B. Cederwall et al. *Nature*, 469:68, 2011.

[55] Evaluated nuclear structure data file (ensdf).

[56] G. Lorusso et al. *Phys. Rev. C*, 86:014313, 2012.

[57] D. G. Jenkins. *Phys. Rev. C*, 80:054303, 2009.

[58] O. L. Pechenaya et al. *Phys. Rev. C*, 76:011304(R), 2007.

[59] J. Cerny et al. *Phys. Rev. Lett.*, 103:152502, 2009.

[60] K. Rykaczewski et al. *Phys. Rev. C*, 52:2310(R), 1995.

[61] P. Kienle et al. *Prog. Part. Nucl. Phys.*, 46:73, 2001.

[62] K. Straub et al. *GSI Scientific Report 2010*, page 151, 2011.

[63] K. Ogawa. *Phys. Rev. C*, 28:223, 1983.

[64] A. Blazhev et al. *J. Phys, Conf. Series*, 205:012035, 2010.

[65] P. Boutachkov et al. *Phys. Rev. C*, 84:044311, 2011.

[66] I. G. Darby et al. *Phys. Rev. Lett.*, 105:16252, 2010.

[67] D. Seweryniak et al. *Phys. Rev. Lett.*, 99:022504, 2007.

[68] T. Otsuka et al. *Phys. Rev. Lett.*, page 012501, 2010.

[69] D. Lubos. PhD thesis, Technische Universität München, 2016.

[70] Y. Yano. *Nucl. Instr. Meth. B*, 261:1009, 2007.

[71] H. Suzuki et al. *Nucl. Instr. Meth. B*, 317:756, 2013.

[72] A. S. Barabash et al. *Sov. J. Nucl. Phys.*, 51:1, 1990.

[73] T. Nakagawa et al. *J. Phys. Soc. Jpn.*, 78:064201, 2009.

[74] O. B. Tarasov and D. Bazin. *Nucl. Instr. Meth. B*, 266:4657, 2008.

[75] I. Čeliković. PhD thesis, Université de Caen, 2013.

[76] N. Fukuda et al. *Nucl. Instr. Meth. B*, 317:323, 2013.

[77] T. Kubo et al. *Prog. Theor. Exp. Phys.*, page 03C003, 2012.

[78] T. Kubo. *Nucl. Instr. Meth. B*, 204:97, 2003.

[79] H. Geissel et al. *Nucl. Instr. Meth. B*, 204:71, 2003.

[80] H. Kumagai et al. *Nucl. Instr. Meth. A*, 470:562, 2001.

[81] H. Blok et al. *Nucl. Instr. Meth. A*, 262:261, 1987.

[82] M. Berz et al. *Phys. Rev. C*, 47:537, 1993.

[83] D. Bazin et al. *Nucl. Instr. Meth. B*, 204:629, 2003.

[84] K. Kimura et al. *Nucl. Instr. Meth. A*, 538:608, 2005.

[85] H. Bethe. *Z. Phys.*, 76:293, 1932.

[86] S. Nishimura et al. *RIKEN Accel. Prog. Rep.*, 46:182, 2013.

[87] F. A. Beck. *Prog. Part. Nucl. Phys.*, 28:443, 1992.

[88] P. H. Regan et al. *AIP Conf. Proc.*, 899:19, 2007.

[89] H. Baba et al. *J. Phys. G*, 37:105103, 2010.

[90] A. Blazhev et al. *Phys. Rev. C*, 69:064304, 2004.

[91] H. Bateman. *Proc. Cambrige Phil. Soc.*, 15:423, 1910.

[92] V. N. Ivanchenko et al. *Nucl. Instr. Meth. A*, 502:666, 2003.

[93] N. Warr, A. Blazhev, and K. Moschner. *EPJ Web of Conf.*, 93:07008, 2015.

[94] N. Mărginean et al. *Eur. Phys. J. A*, 46:329, 2010.

[95] M. Pfützner et al. *Phys. Rev. C*, 65:064604, 2002.

[96] I. Čeliković et al. *Phys. Rev. Lett.*, 116:162501, 2016.

[97] T. Kibédi et al. *Nucl. Instr. Meth. A*, 589:202, 2008.

[98] J. Döring et al. *Phys. Rev. C*, 68:034306, 2003.

[99] K. Moschner. Private communication, 2016.

[100] J. M. Daugas et al. *Phys. Rev. C*, 63:064609, 2001.

[101] K. A. Gladnishki et al. *Phys. Rev. C*, 69:024617, 2004.

[102] J.-J. Gaimard and K.-H. Schmidt. *Nucl. Phys. A*, 531:709, 1991.

[103] M. de Jong, A. V. Ignatuyk, and K-H. Schmidt. *Nucl. Phys. A*, 613:435, 1997.

[104] R. Grzywacz et al. *Phys. Lett. B*, 355:439, 1995.

[105] R. Wadsworth and P. J. Davies. Private communication, 2016.

[106] K.-H. Schmidt et al. *Z. Phys. A*, 319:19, 1984.

[107] M. La Commara et al. *Nucl. Phys. A*, 708:167, 2002.

[108] P. Moller, J. R. Nix, and W. J. Swiatecki. *At. Data Nucl. Data Tables*, 59:185, 1995.

[109] H. Koura et al. *Prog. Theor. Phys.*, 113:305, 2005.

[110] J. Duflo and A. P. Zuker. *Phys. Rev. C*, 52:R23, 1995.

[111] S. Goriely, N. Chamel, and J. M. Pearson. *Phys. Rev. C*, 88:061302(R), 2013.

[112] M. Wang et al. *Chin. Phys. C*, 36:1603, 2012.

[113] D. Bucurescu et al. *Phys. Rev. C*, 69:064319, 2004.

[114] S. Dean et al. *Eur. Phys. J. A*, 21:243, 2004.

[115] D. H. Gloeckner and F. J. D. Serduke. *Nucl. Phys. A*, 220:477, 1974.

[116] R. Gross and A. Frenkel. *Nucl. Phys. A*, 267:85, 1976.

[117] M. Lipoglavšek et al. *Phys. Rev. C*, 72:061304(R), 2005.

[118] M. Lipoglavšek et al. *Phys. Rev. C*, 66:011302(R), 2002.

[119] L. Batist et al. *Eur. Phys. J. A*, 46:45, 2010.

[120] S. N. Liddick et al. *Phys. Rev. Lett*, 97:082501, 2006.

[121] W. Hogervorst et al. *Phys. Scr.*, 9:317, 1974.

[122] A. Algora. Private communication, 2016.

[123] M. L. Cortés. Private communication, 2016.

[124] R. Krücken. *J. Phys. G: Nucl. Part. Phys.*, 31:S1807, 2005.

[125] B. Rubio. *Int. J. Mod. Phys. E*, 15:1979, 2006.

[126] Z. Podolyák. *Nucl. Instr. Meth. B*, 266:4589, 2008.

[127] M. Doncel et al. *J. Instrum.*, 10:P06010, 2015.

[128] C. Wrede. *EPJ Web of Conf.*, 93:07001, 2015.

[129] A. Gade and B. M. Sherrill. *Phys. Scr.*, 91:053003, 2016.

[130] P. Fallon, A. Gade, and I-Y. Lee. *Ann. Rev. Nucl. Part. Sci.*, 66:321, 2016.

Appendix A

γ-ray gates for isomer $T_{1/2}$ determination

Half-lives of γ-decaying isomers shown in Fig. 4.2 were obtained by applying γ-ray gates on the following energies and fitting their time profiles:

Table A.1: γ-ray gates used to obtain half-lives of isomeric states presented in Fig. 4.2.

Nucleus	J^π	γ ray gate energies (keV)
^{88}Zr	8^+	272, 399, 671, 1057, 1083
^{90}Nb	(11^-)	813, 996, 1067
^{90}Mo	8^+	810, 948, 1054
^{92}Mo	8^+	148, 330, 773, 1510
^{92}Tc	(4^+)	214
^{92}Ru	(8^+)	818, 866, 991
^{93}Ru	$(\frac{21}{2}^+)$	544, 1392
^{94}Pd	(19^-)	1545, 1651
	14^+	94, 324, 347, 660, 745, 814, 905, 994, 1092
^{96}Pd	(8^+)	106, 325, 384, 1415
^{96}Ag	(19^+)	4167, 4265
	(15^+)	630, 667
^{98}Ag	(3^+)	107
^{98}Cd	(12^+)	4207, 3696, 3185 (511-keV escape peaks)
	(8^+)	4207(start), 147 (stop)
	(6^+)	147 (start)/688, 1395 (stop)

Appendix B

Electromagnetic transition strengths

The total electromagnetic transition rate λ_{tot} of an excited state, when converted from classical electromagnetic theory to quantum mechanics, is

$$\lambda_{tot} = \left(\frac{E_\gamma}{\hbar c}\right)^{2\ell+1} \frac{8\pi(\ell+1)}{\ell[(2\ell+1)!!]^2\hbar} B(\sigma\ell). \tag{B.1}$$

The total angular momentum difference (in $\hbar$) is ℓ. $B(\sigma\ell)$ is the reduced transition strength:

$$B(\sigma\ell) = \frac{1}{2J_i+1} \left|\langle J_i|\hat{M}(\sigma\ell)|J_f\rangle\right|^2, \tag{B.2}$$

where $\hat{M}(\sigma\ell)$ is the transition operator. The distinction between electric and magnetic radiation is indicated by σ. By determining the transition rate from the data, the experimental transition strength can be obtained for comparison with theoretical calculations.

The total transition rate λ_{tot} of the excited state must be scaled by the branching ratio b and the total internal conversion coefficient α_γ in the following manner:

$$\lambda_\gamma = \lambda_{tot}\frac{b}{1+\alpha_\gamma} = \frac{\ln 2}{T_{1/2}} \cdot \frac{b}{1+\alpha_\gamma}. \tag{B.3}$$

Independent of the experimental quantities, the multipolarity constant

$$K(\sigma\ell) = \frac{(\hbar c)^{2\ell+1}\ell[(2\ell+1)!!]^2\hbar}{8\pi(\ell+1)} \tag{B.4}$$

can be tabulated for each type of electric and magnetic radiation. The simplified formula for $B(\sigma\ell)$ in terms of $K(\sigma\ell)$ and the experimental observables is:

$$B(\sigma\ell) = K(\sigma\ell)E_\gamma^{-(2\ell+1)} \left(\frac{\ln 2}{T_{1/2}}\right)\left(\frac{b}{1+\alpha_\gamma}\right). \tag{B.5}$$

Numerical values for $K(\sigma\ell)$, $B^W(E\ell)$ and $B^W(M\ell)$ up to $\ell = 6$ are provided below:

Table B.1: Numerical values of electromagnetic transition parameters.

$E\ell$	$K(E\ell)$ [in $e^2\mathrm{fm}^{2\ell}\mathrm{MeV}^{2\ell+1}\mathrm{s}$]	$B^W(E\ell)$ [in $e^2\mathrm{fm}^{2\ell}$]
$E1$	1.590×10^{15}	$6.446 \times 10^{-2} A^{2/3}$
$E2$	1.225×10^{9}	$5.940 \times 10^{-2} A^{4/3}$
$E3$	5.708×10^{2}	$5.940 \times 10^{-2} A^{2}$
$E4$	1.697×10^{-4}	$6.285 \times 10^{-2} A^{8/3}$
$E5$	3.457×10^{-11}	$6.929 \times 10^{-2} A^{10/3}$
$E6$	5.108×10^{-18}	$7.884 \times 10^{-2} A^{4}$
$M\ell$	$K(M\ell)$ [in $\mu_N^2\mathrm{fm}^{2\ell-2}\mathrm{MeV}^{2\ell+1}\mathrm{s}$]	$B^W(M\ell)$ [in $\mu_N^2\mathrm{fm}^{2\ell-2}$]
$M1$	1.758×10^{13}	1.790
$M2$	1.355×10^{7}	$1.650 A^{2/3}$
$M3$	6.312	$1.650 A^{4/3}$
$M4$	1.876×10^{-6}	$1.746 A^{2}$
$M5$	3.823×10^{-13}	$1.925 A^{8/3}$
$M6$	5.648×10^{-20}	$2.190 A^{10/3}$

Appendix C

Proton emission $T_{1/2}$ as a function of ℓ and Q_p

The equations and several constants are taken directly from Ref. [9]. Starting with the reduced half-life for proton emission T_{red}

$$T_{red} = \frac{T_{1/2}}{C_l^2}, \tag{C.1}$$

where C_l is the centrifugal barrier function

$$C_l(\chi, \rho) = \exp\left[\frac{l(l+1)}{\chi}\tan\alpha\right], \cos^2\alpha = \frac{Q_p}{V_C^0(R)}. \tag{C.2}$$

The Coulomb potential $V_C^0(R)$ has the common form

$$V_C^0(R) = \frac{Z_D e^2}{R}, \tag{C.3}$$

where Z_D is the atomic number of the daughter nucleus after single proton emission and $R = 1.2(A_D^{1/3} + A_p^{1/3})$ fm is the matching radius. In Ref. [9], experimental data was used to obtain an empirical formula for T_{red}:

$$\log_{10} T_{red} = a(\chi - 20) + b, \tag{C.4}$$

where $a = 1.31$ and $b = -2.44$ for $Z < 68$ nuclei, the atomic number where a sudden change in deformation occurs. For $Z > 68$, $a = 1.25$ and $b = -4.71$. The dimensionless Coulomb parameter χ is

$$\chi = \frac{2Z_D e^2}{\hbar v} \tag{C.5}$$

where $v = \hbar k/\mu = \sqrt{2Q_p/\mu}$ is the velocity of the outgoing proton and $\mu = m_D m_p/(m_D + m_p)$ is the reduced mass of the proton-daughter system.

Putting the equations together, the $T_{1/2}$ of proton emission as a function of Q_p is

$$\log_{10} T_{1/2} = \frac{1}{\ln 10}\left[\frac{\hbar}{Z_D e^2}\sqrt{\frac{2Q_p}{\mu}}l(l+1)\tan\left(\cos^{-1}\sqrt{\frac{Q_p R}{Z_D e^2}}\right)\right] + a\left(\frac{2Z_D e^2}{\hbar}\sqrt{\frac{\mu}{2Q_p}} - 20\right) + b. \tag{C.6}$$

The values of the constants are:

$$\hbar = 197.32697 \text{ MeV} \cdot \text{fm (in units of } \hbar c); \tag{C.7}$$

$$e^2 = 1.4399764 \text{ MeV} \cdot \text{fm}. \tag{C.8}$$